AWARD NUMBER: W81XWH-13-1-0233

TITLE: Development and Translation of Hybrid Optoacoustic/
Ultrasonic Tomography for Early Breast Cancer Detection

PRINCIPAL INVESTIGATOR: Fatima Anis

CONTRACTING ORGANIZATION: Washington University
St. Louis, MO 63130

REPORT DATE: September 2015

TYPE OF REPORT: Final

PREPARED FOR: U.S. Army Medical Research and Materiel Command
Fort Detrick, Maryland 21702-5012

		Form Approved OMB No. 0704-0188
REPORT DOCUMENTATION PAGE		

Public reporting burden for this collection of information is estimated to average 1 hour per response, including the time for reviewing instructions, searching existing data sources, gathering and maintaining the data needed, and completing and reviewing this collection of information. Send comments regarding this burden estimate or any other aspect of this collection of information, including suggestions for reducing this burden to Department of Defense, Washington Headquarters Services, Directorate for Information Operations and Reports (0704-0188), 1215 Jefferson Davis Highway, Suite 1204, Arlington, VA 22202-4302. Respondents should be aware that notwithstanding any other provision of law, no person shall be subject to any penalty for failing to comply with a collection of information if it does not display a currently valid OMB control number. **PLEASE DO NOT RETURN YOUR FORM TO THE ABOVE ADDRESS.**

1. REPORT DATE September 2015	2. REPORT TYPE Final	3. DATES COVERED 1Sep2013 - 31Aug2015
4. TITLE AND SUBTITLE Development and Translation of Hybrid Optoacoustic/Ultrasonic Tomography for Early Breast Cancer Detection		5a. CONTRACT NUMBER
		5b. GRANT NUMBER W81XWH-13-1-0233
		5c. PROGRAM ELEMENT NUMBER
6. AUTHOR(S) Fatima Anis E-Mail: fatimaanis@seas.wustl.edu		5d. PROJECT NUMBER
		5e. TASK NUMBER
		5f. WORK UNIT NUMBER
7. PERFORMING ORGANIZATION NAME(S) AND ADDRESS(ES) Washington University, Sponsored Research Services, Vice Chancellor for Research, Campus Box 1054, One Brookings Drive, St. Louis MO, 63130-4862		8. PERFORMING ORGANIZATION REPORT NUMBER
9. SPONSORING / MONITORING AGENCY NAME(S) AND ADDRESS(ES) U.S. Army Medical Research and Materiel Command Fort Detrick, Maryland 21702-5012		10. SPONSOR/MONITOR'S ACRONYM(S)
		11. SPONSOR/MONITOR'S REPORT NUMBER(S)

12. DISTRIBUTION / AVAILABILITY STATEMENT

Approved for Public Release; Distribution Unlimited

13. SUPPLEMENTARY NOTES

14. ABSTRACT
Optoacoustic tomography (OAT), also known as photoacoustic tomography, is a rapidly emerging hybrid imaging modality that combines high ultrasonic resolution with strong optical or microwave contrast, and represents a highly promising biomedical imaging modality [1,2,3] with a great potential for early breast cancer detection and subsequent management. On the other hand, ultrasound computed tomography (UST) can provide high-resolution anatomical images of breast lesions based on three complementary acoustic properties (speed-of-sound (SOS), attenuation, reflectivity). The broad objective of the proposed research is to develop an optimized system design and associated image reconstruction algorithms for a hybrid three-dimensional (3D) breast imaging system that combines OAT and UST. This system will provide co-registered functional and anatomical information without the need for breast compression, ionizing radiation, or contrast agents, which will result in a highly effective and affordable 3D imaging method.

15. SUBJECT TERMS
Ultrasound Computed tomography, Optoacoutics Tomography, Breast Imaging, Iterative Image reconstruction algorithms, Bent-Ray USCT, GPU-accelerated algorithms

16. SECURITY CLASSIFICATION OF:			17. LIMITATION OF ABSTRACT	18. NUMBER OF PAGES	19a. NAME OF RESPONSIBLE PERSON USAMRMC
a. REPORT Unclassified	b. ABSTRACT Unclassified	c. THIS PAGE Unclassified	Unclassified	66	19b. TELEPHONE NUMBER (include area code)

Standard Form 298 (Rev. 8-98)
Prescribed by ANSI Std. Z39.18

Table of Contents

1. Introduction:

Optoacoustic tomography (OAT), also known as photoacoustic tomography, is a rapidly emerging hybrid imaging modality that combines high ultrasonic resolution with strong optical or microwave contrast, and represents a highly promising biomedical imaging modality with a great potential for early breast cancer detection and subsequent management. On the other hand, ultrasound computed tomography (UST) can provide high-resolution anatomical images of breast lesions based on three complementary acoustic properties (speed-of-sound (SOS), attenuation, reflectivity). The broad objective of the proposed research is to develop an optimized system design and associated image reconstruction algorithms for a hybrid three-dimensional (3D) breast imaging system that combines OAT and UST. This system will provide co-registered functional and anatomical information without the need for breast compression, ionizing radiation, or contrast agents, which will result in a highly effective and affordable 3D imaging method.

2. Keywords:

Ultrasound Computed tomography, Optoacoutics Tomography, Breast Imaging, Iterative Image reconstruction algorithms, Bent-Ray USCT, GPU-accelerated algorithms

3. Overall Project Summary

Task 1: Construct a computational model of the OAT/UST imager and identify optimal system geometries:

1a. Computational modeling of the proposed imager: We have conducted a computational study of imager designs for 3D laser ultrasound (LU) UST. The imager consists of a circular transducer arc attached opposite to a half cylinder. There were 128 transducers attached to the circular arc; which has 140 mm diameter and 118 mm aperture size and is symmetric around the central plane.

1b. Optimization studies (Months 8-36): The goal of the optimization studies was to identify optimal imaging system configurations for OAT and UST that satisfy the design goals. The number and location of the ultrasound emitters, which are constrained to reside on this cylindrical surface, were optimized. In addition to the system parameters, an iterative image reconstruction was optimized. We demonstrated that high quality 3D SOS maps can be reconstructed when only 32 emitters and 128 receiving transducers are employed to record time-of-flight data at 360 tomographic view angles.

1c. Approaches to evaluation of image quality for system optimization: Standard quantitative measures of image quality were employed. These included bias-variance curves, contrast-to-noise ratios.

It is advocated in the modern imaging science literature to utilize objective, or task-based, measures of system performance to guide the optimization of hardware design and image reconstruction algorithms. We investigated this approach to assess the performance of OAT

breast imaging systems. In particular, we applied principles from signal detection theory to compute the detectability of a simulated tumor at different depths within a breast, for two different system designs. The signal-to-noise ratio of the test statistic computed by a numerical observer was employed as the task-specific summary measure of system performance. A numerical breast model was employed that contains both slowly varying background and vessel structures as the background model, and superimpose a deterministic signal to emulate a tumor. This study quantified how signal detection performance of a numerical observer will vary as a function of signal depth and imaging system characteristics. The described methodology is being employed to systematically optimize our OAT imaging system design for tumor detection tasks.

Task 2: Development of reconstruction methods for sparse-array 3D UST

Reconstruction of SOS distribution:

Iterative image reconstruction algorithms have been developed to reconstruct the SOS distribution. These algorithms have also been validated for experimental phantom studies. To perform USCT, measured time-of-flight (TOF) was extracted from the measured signals of the transducer elements.

(i) Time-of-flight (TOF) extraction of the transmission ultrasound signals: I utilized geometrical acoustic-based ray theory to establish a non-linear model that relates the measured TOF values to speed of sound (SOS) distribution. To solve this nonlinear optimization problem, we needed to extract time-of-flight (TOF) from the measured signal. This is a very important pre-processing step for good image quality. In search of the best TOF extraction technique, six TOF extraction algorithms have been implemented and compared: (i) envelope-detection method, (ii) picking the max value of filtered signal, (iii) AIC-method, (iv) weighted-AIC picker, (v) cross-correlation method, and (vi) thresholding method from windowed and filtered signal [1]. These methods were investigated for both the computer simulation by adding different levels of noise and the experimental data (provided by Tomowave Laboratories Inc., Houston TX).

(ii) Bent-Ray method: Algorithms are developed for reconstructing the SOS distribution of breast from knowledge of time-of-flight (TOF) measurements of the transmission ultrasound signals. Utilizing the geometrical acoustic-based ray theory, a non-linear model has been established that relates the measured TOF values to the SOS distribution.

For a given SOS distribution, numerically solution of the Eikonal equation yielded the ray paths. An iterative reconstruction method was developed for inverting the resulting system of equations that alternatively updates the estimates of the SOS and ray paths, minimizes a regularized cost function to obtain the final estimate of the SOS [2].

(iii) Adjoint-State Method: I also investigated a partial differential equation-based Eulerian approach to travel-time tomography as an alternative approach [3]. The work on comparison of the Adjoint-State Method are Ray-tracing algorithm was presented in SPIE Photonics West, 2014 and SPIE Medical Imaging 2014. For detail implementation of this algorithm please see attached proceedings paper. The waveform inversion method for SOS reconstruction has also been explored in the group. In this regard, adjoint-state method provides a suitable initial SOS distribution to aid waveform inversion method.

I performed several numerical studies to compare bent-ray and adjoint-state method. The method was also validated for the experimental phantom studies. In this study, the pressure

signals were recorded using a transducer array consisting of 64 elements and a single Laser Induced Source placed opposite to the middle transducer. The data was recoded for 150 views. The experimental phantom consisted of three tubes at varying salt concentration to exhibit different acoustic and optical properties.

2b. Reconstruction of attenuation distribution

Not accomplished

2c. Reconstruction of reflectivity: An algorithm has been developed to produce reflectivity maps. These algorithms are based on the Synthetic Transmit Aperture (STA) approach [4]. This method utilizes multiple elements or a single source to produce the spherical waves and the whole image is being reconstructed for each emitted signal. The final reflectivity map is obtained by accumulating these individual images. It has been shown that the STA method improves SNR. This method is especially useful in our current study because we are using laser induced ultrasound emitter (LUS), which produce spherical waves. The reflectivity map for breast tomographic was not accomplished.

Task 3: Ultrasound-assisted OAT image reconstruction:

3a. (i) Development of imaging models and reconstruction algorithms: An interpolation-based discrete-discrete imaging model has been implemented to perform 3D OAT for breast imaging [5]. In the new implementation, an unmatched back projection (or pixel-driven) scheme has been used and validated in computer simulations studies. This algorithm is **five times** more efficient than the ray-driven back-projection and allows to perform iterative image reconstruction for large fields-of-views, making it very suitable for breast imaging. To efficiently mitigate data incompleteness, noise, and model error, I investigated the least-squares objective regularized by a TV-norm penalty. I implemented the fast iterative shrinkage/thresholding algorithm (FISTA) to minimize cost function with TV regularization [6].

(ii) In-vivo OAT-Imaging to validate unmatched imaging model: Numerical phantom study
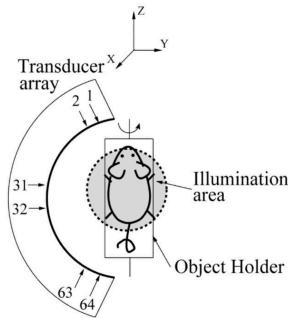

Figure 1: Schematic of full body mouse imaging module. TomoWave Inc. performed experiment.
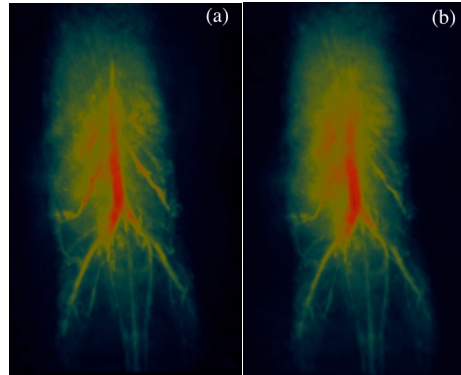

Figure 2: Maximum intensity projection renderings of 3D images of a mouse body using (a) the original interpolation-based algorithm, and (b) the accelerated interpolation-based algorithm.

of the comparison between matched and unmatched imaging model was reported previously. It is

important to validate the model for noisy and experimental data. In order to achieve this validation, image reconstruction was performed for the full-body in-vivo mouse OAT imaging in addition of the numerical phantom study. The results were reported in an oral presentation for SPIE 2015. The schematic of the imaging module is shown in fig. 2. The comparison of mouse images using unmatched imaging model to the matched imaging model is shown in fig. 2. It can be seen clearly that using the unmatched backprojection imaging model has not compromised the resolution of the reconstructed images. This validation is pivotal in achieving the goal of iterative image reconstruction of breast imaging. For more detail please refer to Appendix IV.

3b. (i) GPU implementation of image reconstruction algorithms: Improved GPU-based implementations of a numerical imaging model and its adjoint have been developed for use with general gradient-based iterative image reconstruction algorithms. Particularly, two types of computation-reduced discretization methods have been employed; a parallel fast GPU-based Fourier transform (FFT) algorithm was employed to accelerate the calculation of the temporal convolution with ultrasonic transducer responses; and a volume-reduction method is proposed to reduce the computation for applications with irregular field-of-view (breast imaging). The results suggest that the proposed implementation is more than **five times** faster than previous implementations for a single GPU. In addition, the algorithm has also been developed to use multiple GPUs further reducing the computational time. The work was presented in SPIE Photonics West, 2015.

(ii) Development of Innovative Forward Projection numerical scheme to accomplish Breast Imaging: The unmatched back-projection imaging model, and GPU implementation are two major accomplishments during the first year of developing imaging model and optimization algorithm. The next task is to be able to perform image reconstruction for the breast. The iterative image reconstruction involved as much as up to 35000 integration step over a volume of up to 70 mm x 70 mm x 90 mm, with the discretization requirement much less than 1 mm. The iterative reconstruction tomography required more innovation. To achieve even faster images, I exploited the symmetry of the problem. The schematic of the object volume is shown in Fig. In previous implementation the object volume was fully contained inside a sphere. The integration was performed over the surface of intersection between the two spheres (one of the

Figure 3: Schematic of the integration volume for the forward projection of imaging model.

object and second defined by the transducers' location to receive pressure wave at a given time) to calculate the forward projection (blue and grey shaded regions). However, this was infeasible for breast imaging application. In this case, I devised the hemispherical object volume (red shaded region) and, the chest wall was modeled by a plane. I derived analytically the intersection between the plane and the integration surface to eliminate undesirable integration steps. This
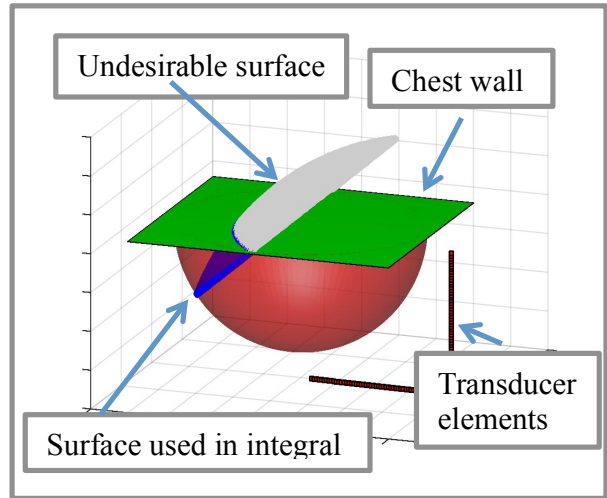
allowed us to conduct studies for numerical breast phantoms of realistic sizes and clinical studies.

Task 4: Validate prototype imager and image reconstruction algorithms

4a. Experimental phantom studies:

We conducted experimental phantom studies using the first-generation prototype OAT breast imaging system built by our collaborators at TomoWave Inc. The first experiment uses a gelatin phantom mimicking breast tissue. A gelatin phantom was created to mimic normal breast tissue, with an embedded gelatin sphere to represent tumor and two crossing tubes filled with an optical-absorbing fluid to represent blood vessel. The phantom was imaged. The pressure data was collected for 1536 time samples with a sampling frequency of 12.5 MHz at 1800 tomographic views. The reconstructed OAT images are displayed in Fig. 4. These images accurately revealed the phantom structures.
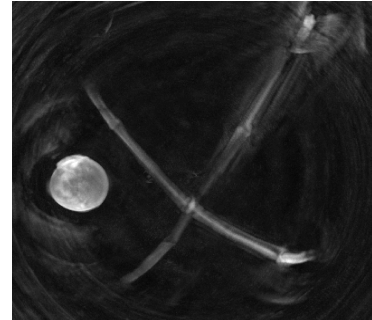

Figure 4: Maximum intensity projection image of an experimental phantom contains tubes and a sphere.

4b. Use of clinical image data:

We also conducted preliminary that employed clinical data. Figure 5 shows an OAT image. Pressure data is collected at only 300 tomographic views. It is very encouraging to observe that some major vascular structures can be clearly reconstructed along with some peripheral small capillary vessels. The study helped immensely for phase-II design of imaging module and imaging reconstruction methods.

Figure 5: Maximum intensity projection image of a female breast (clinical study).

4. KEY RESEARCH ACCOMPLISHMENTS

- A novel OAT imaging system for breast imaging was designed and implemented.
- Image reconstruction methods were developed, implemented, and tested.
- The developed system and algorithms were employed in a pilot clinical study in which 3D OAT images, in vivo, were acquired. The images revealed the presence of vessels and other blood filled structures.

5. Conclusion

This project involved the development and clinical validation of an innovative 3D breast imaging system that provides co-registered functional and anatomical information without the use of ionizing radiation. The system is first of its kind to produce comprehensive clinical information based on co-registered volumetric images of two types of OAT images depicting the absorbed optical energy (blood distribution and its oxygenation) and three types of UST images (speed-of-sound, ultrasonic reflectance, and ultrasonic attenuation distributions) of the breast tissue. This will provide an extremely rich set of complementary anatomical and functional 3D information to the radiologist, enabling early detection of small tumors (such as *in situ* lesions), accurate

staging of more advanced tumors, and diagnostic characterization of the tumor potential for aggressive growth and metastatic activity. Early tumors (< 6 mm) are undetectable with the existing screening mammography, especially in a dense breast of younger women. Unlike X-ray based or nuclear imaging methods, the proposed imaging method is radiation-safe, pain-free (no compression required), toxicity-free, and much less expensive. The new ultrasound plus optoacoustic tomography platform is expected to transform breast cancer care by providing a better screening method and serve as a highly valuable tool for monitoring and identifying effective cancer therapies.

6. Publications, Abstracts, and Presentations

1a. **Title:** Waveform Inversion with Source Encoding for Breast Speed-of-Sound Reconstruction in Ultrasound Computed Tomography (submitted)
Authors: Kun Wang, Thomas Mathew, **Fatima Anis**, Cuiping Li, Neb Duric, and Mark Anastasio
Journal: IEEE Transaction on Ultrasonics, Ferroelectrics, and frequency control, 2015; **62**(3): 475-492.

2a. **Title:** Three-Dimensional Optoacoustic and Laser-Induced Ultrasound Tomography System for Preclinical Research in Mice Design and Phantom Validation.
Authors: Ermilov SA, Su R, Conjusteau A, **Fatima Anis**, Nadvoretskiy V, Anastasio MA, Oraevsky AA.
Journal: Ultrasonic imaging. 2016;38(1):77-95.

1b*. **Title:** Investigation of the adjoint-state method for ultrasound computed tomography: a numerical and experimental study
Authors: Fatima Anis, Yang Lou, Andre Conjusteau, Sergey Ermilov, Alexander Oraevsky and Mark A. Anastasio
Conference: SPIE Photonics West- 2014;8943, San Francisco CA

2b- **Title:** Investigation of a method for laser-induced ultrasound tomography that eliminates the need for ray tracing
Authors: Fatima Anis, Yang Lou, Andre Conjusteau, Sergey Ermilov, Alexander Oraevsky and Mark A. Anastasio
Conference: SPIE Medical Imaging 2015: Ultrasonic Imaging and Tomography

3b- **Title:** Accelerated iterative image reconstruction in three-dimensional optoacoustic tomography
Authors: Fatima Anis, Yang Lou, Kun Wang, Richard Su, Tanmayi Oruganti, Andre Conjusteau, Sergey Ermilov, Alexander A. Oraevsky and Mark A. Anastasio
Conference: SPIE Photonics West, 2015

4b- **Title:** Waveform Inversion with Source Encoding for Breast Speed-of-Sound Reconstruction in Ultrasound Computed Tomography
Authors: Kun Wang, Thomas Mathew, **Fatima Anis**, Cuiping Li, Neb Duric, and Mark A. Anastasio
Conference: SPIE Medical Imaging 2015: Ultrasonic Imaging and Tomography

5b- **Title:** Three-dimensional laser optoacoustic and laser ultrasound imaging system for biomedical research
Authors: Sergey A. Ermilov, Rishard Su, Andre Conjusteau, Kun Wag, Fatima Anis, Mark A. Anastasio, Alexander A. Oreavsky
Conference: SPIE: Photon Plus Ultrasound: Imaging and Sensing 2015; 9323

7. Training

The year has been very fruitful as I continue to benefit from many scholarly activities and kept adding to my skills as imaging scientist.

1- **Attending course (E62 BME 500 67):** In Fall 2014, I participated in BME course on the imaging science. The class held weekly for two hours. Some of the study topics included continuous and discrete object representations, imaging operators, image statistics, imaging quality assessment, ideal observer, Hotelling observers and imaging errors. The course provided me with a formal training as biomedical image scientist.

2- **Conferences:**
i- SPIE Photonics West, 2014 San Francisco CA: The conference is the major international meeting held annually for the optoacoustic/photoacpustic imaging. I attended this meeting and was greatly benefited from the presentation and poster sessions as well as constructive meetings with the Prof. Oraevsky and his team about the hybrid OAT/ USCT breast imager.

ii- SPIE Medical Imaging, 2014, San Diago CA: This conference is another major international conference, which holds annually and covers broad range of topics concerning medical imaging and diagnostics. I was specially benefited from many talks and poster presentations about the image quality assessment. Moreover, the dedicated Ultrasonic Imaging and Tomography sessions on ultrasound imaging provided me with a great opportunity to learn about ultrasound tomography in medical imaging.

iii- SPIE Photonics West, 2015 San Francisco CA

3- **Visiting TomoWave Inc, Houston TX:**
I visited TomoWave Inc. in December 2013. During the visit, I benefited from lab tours and learned about practical aspects of OAT/USCT imaging.

4- **Algorithm development and GPU computing:** I continued to establish more skills towards algorithm development. One of the major achievements towards this end was to learn CUDA programming from other group members. This training will continue to benefit me through the remainder of the project.

5- **Image rendering software:** I learned image rendering softwares for 3D visualization of the imaging. This is important and allows one to draw inference form the reconstructed images.

8. Reportable Outcomes
Nothing to report

9. Other Achievements
Nothing to report

10. References

[1] C. Li, L. Huang, N. Duric, H. Zhang, and C. Rowe, "An improved automatic time-of-flight picker for medical ultrasound tomography," Ultrasonics, vol. 49, no. 1, pp. 61–72, 2009.
[2] A. Hormati, I. Jovanovi, O. Roy, and M. Vetterli, "Robust ultrasound travel-time tomography using the bent ray model," Proc. SPIE, vol. 7629, 2010, pp. 76 290I–76 290I–12.
[3] S. Leung and J. Qian, "An adjoint-state method for three-dimensional transmission traveltime tomography using rst arrivals," Comm. in Math and Sci. 4(1), p. 2006, 249-266.
[4] J.A. Jensen, S.I. Nikolov, K.L. Gammelmark, M.H. Pedersen, Synthetic aperture ultrasound imaging, Ultrasonics 44 (2006) e5–e15.
[5] K. Wang, C. Huang, Y.J. Kao, C.Y. Chou, A.A. Oraevsky, M.A. Anastasio, "Accelerating image reconstruction in three-dimensional optoacoustic tomography on graphics processing units",Medical Physics, 40 (2) (2013), p. 023301.
[6] Amir Beck and Marc Teboulle, "A fast iterative shrinkage-thresholding algorithm for linear inverse problems," SIAM J. Img. Sci., 2(1):183–202, March 2009.

11. Appendices
1- Waveform Inversion with Source Encoding for Breast Speed-of-Sound Reconstruction in Ultrasound Computed Tomography"
2- Conference Proceedings, SPIE Photonics West, 2014
3- Abstract submitted for the poster presentation in SPIE Medical Imaging, 2014
4- Co-author in the abstract submitted for the oral presentation in upcoming SPIE Medical Imaging, 2015
5- Three-Dimensional Optoacoustic and Laser-Induced Ultrasound Tomography System for Preclinical Research in Mice Design and Phantom Validation.
6- Accelerated iterative image reconstruction in three-dimensional optoacoustic tomography

Waveform Inversion With Source Encoding for Breast Sound Speed Reconstruction in Ultrasound Computed Tomography

Kun Wang, *Member, IEEE*, Thomas Matthews, *Student Member, IEEE*, Fatima Anis, Cuiping Li, Neb Duric, and Mark A. Anastasio, *Senior Member, IEEE*

Abstract—Ultrasound computed tomography (USCT) holds great promise for improving the detection and management of breast cancer. Because they are based on the acoustic wave equation, waveform inversion-based reconstruction methods can produce images that possess improved spatial resolution properties over those produced by ray-based methods. However, waveform inversion methods are computationally demanding and have not been applied widely in USCT breast imaging. In this work, source encoding concepts are employed to develop an accelerated USCT reconstruction method that circumvents the large computational burden of conventional waveform inversion methods. This method, referred to as the waveform inversion with source encoding (WISE) method, encodes the measurement data using a random encoding vector and determines an estimate of the sound speed distribution by solving a stochastic optimization problem by use of a stochastic gradient descent algorithm. Both computer simulation and experimental phantom studies are conducted to demonstrate the use of the WISE method. The results suggest that the WISE method maintains the high spatial resolution of waveform inversion methods while significantly reducing the computational burden.

I. Introduction

AFTER decades of research [1]–[4], advancements in hardware and computing technologies are now facilitating the clinical translation of ultrasound computed tomography (USCT) for breast imaging applications [2], [5]–[8]. USCT holds great potential for improving the detection and management of breast cancer because it provides novel acoustic tissue contrasts, is radiation- and breast-compression-free, and is relatively inexpensive [9], [10]. Several studies have reported the feasibility of USCT for characterizing breast tissues [2], [4]–[6], [10], [11]. Although some USCT systems are capable of generating three images that depict the breast's acoustic reflectivity, acoustic attenuation, and sound speed distributions, this study will focus on the reconstruction of the sound speed distribution.

A variety of USCT imaging systems have been developed for breast sound speed imaging [5], [7], [10], [12]–[15]. In a typical USCT experiment, acoustic pulses that are generated by different transducers are employed, in turn, to insonify the breast. The resulting wavefield data are measured by an array of ultrasonic transducers that are located outside of the breast. Here and throughout the manuscript, a transducer that produces an acoustic pulse will be referred to as an emitter; the transducers that receive the resulting wavefield data will be referred to as receivers. From the collection of recorded wavefield data, an image reconstruction method is utilized to estimate the sound speed distribution within the breast [5], [7], [10].

The majority of USCT image reconstruction methods for breast imaging investigated to date have been based on approximations to the acoustic wave equation [12], [16]–[24]. A relatively popular class of methods is based on geometrical acoustics. Such methods are commonly referred to as ray-based methods. These methods involve two steps. First, time-of-flight (TOF) data corresponding to each emitter-receiver pair are estimated [25]. Under a geometrical acoustics approximation, the TOF data are related to the sound speed distribution via an integral geometry, or ray-based, imaging model [16], [26]. Second, by use of the measured TOF data and the ray-based imaging model, a reconstruction algorithm is employed to estimate the sound speed distribution. Although ray-based methods can be computationally efficient, the spatial resolution of the images they produce is limited due to the fact that diffraction effects are not modeled [23], [27]. This is undesirable for breast imaging applications, in which the ability to resolve fine features (e.g., tumor spiculations) is important for distinguishing healthy from diseased tissues.

USCT reconstruction methods based on the acoustic wave equation, also known as full-wave inverse scattering or waveform inversion methods, have also been explored for a variety of applications including medical imaging [12], [22], [23], [28] and geophysics [29]–[31]. Because they account for higher-order diffraction effects, waveform inversion methods can produce images that possess higher spatial resolution than those produced by ray-based methods [23], [28]. However, conventional waveform inversion methods are iterative in nature and require the wave

equation to be solved numerically a large number of times at each iteration. Consequently, such methods can be extremely computationally burdensome. For special geometries [12], [32], efficient numerical wave equation solvers have been reported. However, apart from special cases, the large computational burden of waveform inversion methods has hindered their widespread application.

A natural way to reduce the computational complexity of the reconstruction problem is to reformulate it in a way that permits a reduction in the number of times the wave equation needs to be solved. In the geophysics literature, source encoding methods have been proposed to achieve this [29]–[31]. When source encoding is employed, at each iteration of a prescribed reconstruction algorithm, all of the acoustic pulses produced by the emitters are combined (or encoded) by use of a random encoding vector. The measured wavefield data are combined in the same way. As a result, the wave equation may need to be solved as few as twice at each algorithm iteration. In conventional waveform inversion methods, this number would be equal to twice the number of emitters employed. Although conventional waveform inversion methods may require fewer algorithm iterations to obtain a specified image accuracy compared with source encoded methods, as demonstrated later, the latter can greatly reduce the overall number of times the wave equation needs to be solved.

In this study, a waveform inversion with source encoding (WISE) method for USCT sound speed reconstruction is developed and investigated for breast imaging with a circular transducer array. The WISE method determines an estimate of the sound speed distribution by solving a stochastic optimization problem by use of a stochastic gradient descent algorithm [30], [33]. Unlike previously studied waveform inversion methods that were based on the Helmholtz equation [22], [23], the WISE method is formulated by use of the time-domain acoustic wave equation [34]–[36] and uses broad-band measurements. The wave equation is solved by use of a computationally efficient k-space method that is accelerated by use of graphics processing units (GPUs). To mitigate the interference of the emitter on its neighboring receivers, a heuristic data replacement strategy is proposed. The method is validated in computer simulation studies that include modeling errors and other physical factors. The practical applicability of the method is further demonstrated in studies involving experimental breast phantom data.

The remainder of the paper is organized as follows. In Section II, USCT imaging models in their continuous and discrete forms are reviewed. A conventional waveform inversion method and the WISE method for sound speed reconstruction are formulated in Section III. The computer simulation studies and corresponding numerical results are presented in Sections IV and V, respectively. In Section VI, the WISE method is further validated in experimental breast phantom studies. Finally, the paper concludes with a discussion in Section VII.

II. Background: USCT Imaging Models

In this section, imaging models that provide the basis for image reconstruction in waveform inversion-based USCT are reviewed.

A. USCT Imaging Model in Its Continuous Form

Although a digital imaging system is properly described as a continuous-to-discrete (C-D) mapping (chapter 7 in [37]), for simplicity, a USCT imaging system is initially described in its continuous form below.

In USCT breast imaging, a sequence of acoustic pulses is transmitted through the breast. We denote each acoustic pulse by $s_m(\mathbf{r},t) \in \mathbb{L}^2(\mathbb{R}^3 \times [0,\infty))$, where each pulse is indexed by an integer m for $m = 0, 1, ..., M-1$ with M denoting the total number of acoustic pulses. Although it is spatially localized at the emitter location, each acoustic pulse can be expressed as a function of space and time. When the mth pulse propagates through the breast, it generates a pressure wavefield distribution denoted by $p_m(\mathbf{r},t) \in \mathbb{L}^2(\mathbb{R}^3 \times [0,\infty))$. If acoustic absorption and mass density variations are negligible, $p_m(\mathbf{r},t)$ in an unbounded medium satisfies the acoustic wave equation [38]:

$$\nabla^2 p_m(\mathbf{r},t) - \frac{1}{c^2(\mathbf{r})} \frac{\partial^2}{\partial t^2} p_m(\mathbf{r},t) = -4\pi s_m(\mathbf{r},t), \quad (1)$$

where $c(\mathbf{r})$ is the sought-after sound speed distribution. Eq. (1) can be expressed in operator form as

$$p_m(\mathbf{r},t) = \mathcal{H}^c s_m(\mathbf{r},t), \quad (2)$$

where the linear operator $\mathcal{H}^c : \mathbb{L}^2(\mathbb{R}^3 \times [0,\infty)) \mapsto \mathbb{L}^2(\mathbb{R}^3 \times [0,\infty))$ denotes the action of the wave equation and is independent of the index of m. The superscript c indicates the dependence of $\mathcal{H}^c$ on $c(\mathbf{r})$.

Consider that $p_m(\mathbf{r},t)$ is recorded outside of the object for $\mathbf{r} \in \Omega_m$ and $t \in [0,T]$, where $\Omega_m \subset \mathbb{R}^3$ denotes a continuous measurement aperture. In this case, when discrete sampling effects are neglected, the imaging model can be described as a continuous-to-continuous mapping as

$$g_m(\mathbf{r},t) = \mathcal{M}_m \mathcal{H}^c s_m(\mathbf{r},t), \quad \text{for} \quad m = 0,1,\cdots,M-1, \quad (3)$$

where $g_m(\mathbf{r},t) \in \mathbb{L}^2(\Omega_m \times [0,T])$ denotes the measured data function and the operator $\mathcal{M}_m$ is the restriction of $\mathcal{H}^c$ to $\Omega_m \times [0,T]$. The m-dependent operator $\mathcal{M}_m$ allows (3) to describe USCT imaging systems in which the measurement aperture varies with emitter location. Here and throughout the manuscript, we will refer to the process of firing one acoustic pulse and acquiring the corresponding wavefield data as one data acquisition indexed by m. The USCT reconstruction problem in its continuous form is to estimate the sound speed distribution $c(\mathbf{r})$ by use of (3) and the data functions $\{g_m(\mathbf{r},t)\}_{m=0}^{M-1}$.

B. USCT Imaging Model in Its Discrete Forms

A digital imaging system is accurately described by a continuous-to-discrete (C-D) imaging model, which is typically approximated in practice by a discrete-to-discrete (D-D) imaging model to facilitate the application of iterative image reconstruction algorithms. A C-D description of the USCT imaging system is provided in Appendix A. Below, a D-D imaging model for waveform-based USCT is presented. This imaging model will be employed subsequently in the development of the WISE method in Section III.

Construction of a D-D imaging model requires the introduction of finite-dimensional approximate representations of the functions $c(\mathbf{r})$ and $s_m(\mathbf{r},t)$, which will be denoted by the vectors $\mathbf{c} \in \mathbb{R}^N$ and $\mathbf{s}_m \in \mathbb{R}^{NL}$. Here, N and L denote the number of spatial and temporal samples, respectively, employed by the numerical wave equation solver. In waveform-based USCT, the way in which $c(\mathbf{r})$ and $s_m(\mathbf{r},t)$ are discretized to form $\mathbf{c}$ and $\mathbf{s}_m$ is dictated by the numerical method employed to solve the acoustic wave equation. In this study, we employ a pseudospectral k-space method [34]–[36]. Accordingly, $c(\mathbf{r})$ and $s_m(\mathbf{r},t)$ are sampled on Cartesian grid points as

$$[\mathbf{c}]_n = c(\mathbf{r}_n), \quad \text{and} \quad [\mathbf{s}_m]_{nL+l} = s_m(\mathbf{r}_n, l\Delta^t),$$
$$\text{for} \quad \begin{matrix} n = 0,1,\cdots,N-1 \\ l = 0,1,\cdots,L-1 \end{matrix}, \tag{4}$$

where Δ^t denotes the temporal sampling interval and $\mathbf{r}_n$ denotes the location of the nth point.

For a given $\mathbf{c}$ and $\mathbf{s}_m$, the pseudospectral k-space method can be described in operator form as

$$\mathbf{p}_m^{\mathrm{a}} = \mathbf{H}^{\mathrm{c}}\mathbf{s}_m, \tag{5}$$

where the matrix $\mathbf{H}^{\mathrm{c}}$ is of dimension $NL \times NL$ and represents a discrete approximation of the wave operator $\mathcal{H}^{\mathrm{c}}$ defined in (2), and the vector $\mathbf{p}_m^{\mathrm{a}}$ represents the estimated pressure data at the grid point locations and has the same dimension as $\mathbf{s}_m$. The superscript a indicates that these values are approximate, i.e., $[\mathbf{p}_m^{\mathrm{a}}]_{nL+l} \approx p_m(\mathbf{r}_n, l\Delta^t)$. We refer the readers to [34]–[36] for additional details regarding the pseudospectral k-space method.

Because the pseudospectral k-space method yields sampled values of the pressure data on a Cartesian grid, a sampling matrix $\mathbf{M}_m$ is introduced to model the USCT data acquisition process as

$$\mathbf{g}_m^{\mathrm{a}} = \mathbf{M}_m\mathbf{p}_m^{\mathrm{a}} \equiv \mathbf{M}_m\mathbf{H}^{\mathrm{c}}\mathbf{s}_m. \tag{6}$$

Here, the $N^{\mathrm{rec}}L \times NL$ sampling matrix $\mathbf{M}_m$ extracts the pressure data corresponding to the receiver locations on the measurement aperture Ω_m, with N^{rec} denoting the number of receivers. The vector $\mathbf{g}_m^{\mathrm{a}}$ denotes the predicted data that approximates the true measurements. In principle, $\mathbf{M}_m$ can be constructed to incorporate transducer characteristics, such as finite aperture size and temporal delays. For simplicity, we assume that the transducers are point-like in this study. When the receiver and grid point locations do not coincide, an interpolation method is required. As an example, when a nearest-neighbor interpolation method is employed, the elements of $\mathbf{M}_m$ are defined as

$$[\mathbf{M}_m]_{n^{\mathrm{rec}}L+l,nL+l} = \begin{cases} 1, & \text{for} \quad n = \mathcal{I}_m(n^{\mathrm{rec}}), \\ 0, & \text{otherwise,} \end{cases} \tag{7}$$

where $[\mathbf{M}_m]_{n^{\mathrm{rec}}L+l,nL+l}$ denotes the element of $\mathbf{M}_m$ at the $(n^{\mathrm{rec}}L + l)$th row and the $(nL + l)$th column, and $\mathcal{I}_m(n^{\mathrm{rec}})$ denotes the index of the grid point that is closest to $\mathbf{r}(m,n^{\mathrm{rec}})$. Here, $\mathbf{r}(m,n^{\mathrm{rec}})$ denotes the location of the n^{rec}th receiver in the mth data acquisition. Eq. (6) represents the D-D imaging model that will be employed in the remainder of this study.

III. WAVEFORM INVERSION WITH SOURCE ENCODING FOR USCT

A. Sequential Waveform Inversion in Its Discrete Form

A conventional waveform inversion method that does not utilize source encoding will be employed as a reference for the developed WISE method and is briefly described below. Like other conventional approaches, this method sequentially processes the data acquisitions $\{\mathbf{g}_m\}$ (in an arbitrary order) for $m = 0, 1, ..., M - 1$ at each iteration of the associated algorithm. As such, we will refer to the conventional method as a sequential waveform inversion method.

A sequential waveform inversion method can be formulated as a nonlinear numerical optimization problem:

$$\hat{\mathbf{c}} = \arg \min_{\mathbf{c}}\{\mathcal{F}(\mathbf{c}) + \beta\mathcal{R}(\mathbf{c})\}, \tag{8}$$

where $\mathcal{F}(\mathbf{c})$, $\mathcal{R}(\mathbf{c})$, and β denote the data fidelity term, the penalty term, and the regularization parameter, respectively. The data fidelity term $\mathcal{F}(\mathbf{c})$ is defined as a sum of squared ℓ^2 norms of the data residuals corresponding to all data acquisitions as

$$\mathcal{F}(\mathbf{c}) = \frac{1}{2}\sum_{m=0}^{M-1} \parallel \underline{\mathbf{g}}_m - \mathbf{M}_m\mathbf{H}^{\mathrm{c}}\mathbf{s}_m \parallel^2, \tag{9}$$

where $\underline{\mathbf{g}}_m \in \mathbb{R}^{N^{\mathrm{rec}}L}$ denotes the measured data vector at the mth data acquisition. The choice of the penalty term will be addressed in Section IV.

The gradient of $\mathcal{F}(\mathbf{c})$ with respect to $\mathbf{c}$, denoted by $\mathbf{J}$, will be computed by discretizing an expression for the Fréchet derivative that is derived assuming a continuous form of (9). The Fréchet derivative is described in Appendix B. Namely, the gradient is approximated as

$$[\mathbf{J}]_n \equiv \sum_{m=0}^{M-1}[\mathbf{J}_m]_n$$

$$\approx \frac{1}{[\mathbf{c}]_n^3}\sum_{m=0}^{M-1}\sum_{l=1}^{L-2}[\mathbf{q}_m^{\mathrm{a}}]_{nL+(L-l)} \qquad (10)$$

$$\times \frac{[\mathbf{p}_m^{\mathrm{a}}]_{nL+l-1}-2[\mathbf{p}_m^{\mathrm{a}}]_{nL+l}+[\mathbf{p}_m^{\mathrm{a}}]_{nL+l+1}}{\Delta^{\mathrm{t}}},$$

where $\mathbf{J}_m$ denotes the gradient of $\|\underline{\mathbf{g}}_m - \mathbf{M}_m\mathbf{H}^{\mathrm{c}}\mathbf{s}_m\|^2/2$ with respect to $\mathbf{c}$ and the vector $\mathbf{q}_m^{\mathrm{a}}$ contains samples that approximate adjoint wavefield $q_m(\mathbf{r},t)$ that satisfies (34) in Appendix B. By use of the pseudospectral k-space method, $\mathbf{q}_m^{\mathrm{a}}$ can be calculated as

$$\mathbf{q}_m^{\mathrm{a}} = \frac{1}{4\pi}\mathbf{H}^{\mathrm{c}}\boldsymbol{\tau}_m, \qquad (11)$$

where

$$[\boldsymbol{\tau}_m]_{nL+l} = \begin{cases} [\mathbf{g}_m^{\mathrm{a}}-\underline{\mathbf{g}}_m]_{\mathcal{I}_m^{-1}(n)L+(L-l)}, & \text{if } n \in \mathbb{N}_m, \\ 0, & \text{otherwise.} \end{cases} \qquad (12)$$

Here, $\mathbb{N}_m = \{n: \mathcal{I}_m(n^{\mathrm{rec}}), n^{\mathrm{rec}}=0,1,\cdots,N^{\mathrm{rec}}-1\}$, and $\mathcal{I}_m^{-1}$ denotes the inverse mapping of $\mathcal{I}_m$.

Given the explicit form of $\mathbf{J}$ in (10), a variety of optimization algorithms can be employed to solve (8) [39]. Algorithm 1 describes a gradient descent-based sequential waveform inversion method. Note that at every algorithmic iteration, the sequential waveform inversion method updates the sound speed estimate only once using the gradient $\mathbf{J}$ accumulated over all $\mathbf{J}_m$ for $m = 0, 1, ..., M - 1$. This is unlike the Kaczmarz method—also known as the algebraic reconstruction technique [16], [19], [40]—that updates the sound speed estimate multiple times in one algorithmic iteration. In Line 10 of Algorithm 1, $\mathbf{J}^{\mathrm{R}}$ denotes the gradient of $\mathcal{R}(\mathbf{c})$ with respect to $\mathbf{c}$.

Algorithm 1: Gradient descent-based sequential waveform inversion.
Input: $\{\underline{\mathbf{g}}_m\}, \{\mathbf{s}_m\}, \mathbf{c}^{(0)}$
Output: $\hat{\mathbf{c}}$

- 1: $k \leftarrow 0$ {k is the number of algorithm iteration.}
- 2: **while** stopping criterion is not satisfied do
- 3: $k \leftarrow k + 1$
- 4: $\mathbf{J} \leftarrow \mathbf{0}$
- 5:   **for** $m := 0$ **to** $M - 1$ **do**
- 6: $\mathbf{p}_m^{\mathrm{a}} \leftarrow \mathbf{H}^{\mathrm{c}}\mathbf{s}_m$ {m is the index of the emitter.}
- 7: $\mathbf{q}_m^{\mathrm{a}} \leftarrow \mathbf{H}^{\mathrm{c}}\boldsymbol{\tau}_m$ {$\boldsymbol{\tau}_m$ is calculated via (12).}
- 8: $\mathbf{J} \leftarrow \mathbf{J} + \mathbf{J}_m$ {$\mathbf{J}_m$ is calculated via (10).}
- 9:   **end for**
- 10: $\mathbf{J} \leftarrow \mathbf{J} + \beta\mathbf{J}^{\mathrm{R}}$
- 11:   Determine step size λ via a line search
- 12: $\mathbf{c}^{(k)} \leftarrow \mathbf{c}^{(k-1)} - \lambda\mathbf{J}$
- 13: **end while**
- 14: $\hat{\mathbf{c}} = \mathbf{c}^{(k)}$

In Algorithm 1, $\mathbf{H}^{\mathrm{c}}$ is the most computationally burdensome operator, representing one run of the wave equa-

tion solver. Note that it appears in Lines 6, 7, and 11. Because Lines 6 and 7 have to be executed M times to process all of the data acquisitions and the line search method must pass through all M emitters at least once, the wave equation solver has to be executed at least $3M$ times at each algorithm iteration. The line search in Line 11 searches for a step size along the direction of $-\mathbf{J}$ so that the cost function is reduced by use of a classic trial-and-error approach [39]. Note that, in general, the line search will require more than M applications of $\mathbf{H}^{\mathrm{c}}$, so $3M$ represents a lower bound on the total number of wave equation solver runs per iteration.

B. Stochastic Optimization-Based WISE

To alleviate the large computational burden presented by sequential waveform inversion methods (e.g., Algorithm 1), a source encoding method has been proposed [22], [29], [41]. This method has been formulated as a stochastic optimization problem and solved by various stochastic gradient-based algorithms [30], [31]. In this section, we adapt the stochastic optimization-based formulation in [30] to find a solution of (8).

Algorithm 2. WISE Method.
Input: $\{\underline{\mathbf{g}}_m\}, \{\mathbf{s}_m\}, \mathbf{c}^{(0)}$
Output: $\hat{\mathbf{c}}$

- 1: $k \leftarrow 0$ {k is the number of algorithm iteration.}
- 2: **while** stopping criterion is not satisfied do
- 3: $k \leftarrow k + 1$
- 4:   Draw elements of $\mathbf{w}$ from independent and identical Rademacher distribution.
- 5: $\mathbf{p}^{\mathrm{w}} \leftarrow \mathbf{H}^{\mathrm{c}}\mathbf{s}^{\mathrm{w}}$ {$\mathbf{s}^{\mathrm{w}}$ is calculated via (14).}
- 6: $\mathbf{q}^{\mathrm{w}} \leftarrow \mathbf{H}^{\mathrm{c}}\boldsymbol{\tau}^{\mathrm{w}}$ {$\boldsymbol{\tau}^{\mathrm{w}}$ is calculated via (17).}
- 7: $\mathbf{J} \leftarrow \mathbf{J}^{\mathrm{w}} + \beta\mathbf{J}^{\mathrm{R}}$ {$\mathbf{J}^{\mathrm{w}}$ is calculated via (16).}
- 8:   Determine step size λ by use of line search
- 9: $\mathbf{c}^{(k)} \leftarrow \mathbf{c}^{(k-1)} - \lambda\mathbf{J}$
- 10: **end while**
- 11: $\hat{\mathbf{c}} = \mathbf{c}^{(k)}$

The WISE method seeks to minimize the same cost function as the sequential waveform inversion method, namely (8). However, to accomplish this, the data fidelity term in (9) is reformulated as the expectation of a random quantity as [29]–[31], [33], [41], [42]

$$\mathcal{F}_s(\mathbf{c}) = \mathbf{E}_{\mathbf{w}}\left\{\frac{1}{2}\|\underline{\mathbf{g}}^{\mathrm{w}}-\mathbf{M}\mathbf{H}^{\mathrm{c}}\mathbf{s}^{\mathrm{w}}\|^2\right\}, \qquad (13)$$

where $\mathbf{E}_{\mathbf{w}}$ denotes the expectation operator with respect to the random source encoding vector $\mathbf{w} \in \mathbb{R}^M$, $\mathbf{M} \equiv \mathbf{M}_m$ is the sampling matrix that is assumed to be identical for $m = 0, 1, ..., M - 1$, and $\underline{\mathbf{g}}^{\mathrm{w}}$ and $\mathbf{s}^{\mathrm{w}}$ denote the $\mathbf{w}$-encoded data and source vectors, defined as

$$\underline{\mathbf{g}}^{\mathrm{w}} = \sum_{m=0}^{M-1}[\mathbf{w}]_m\underline{\mathbf{g}}_m, \quad \text{and} \quad \mathbf{s}^{\mathrm{w}} = \sum_{m=0}^{M-1}[\mathbf{w}]_m\mathbf{s}_m, \qquad (14)$$
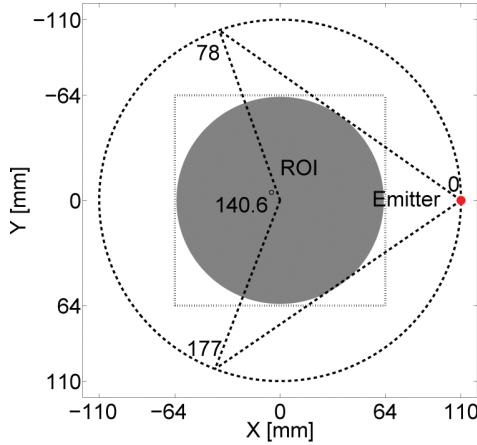
Fig. 1. Schematic of a USCT system with a circular transducer array whose elements are indexed from 0 to 255. It shows the first data acquisition, where element 0 (in red) is emitting an acoustic pulse, whereas all 256 elements are receiving signals. The region of interest (ROI) is shaded in gray, and the dashed square box represents the physical dimensions (128×128 mm^2) of all reconstructed images.

respectively. It has been demonstrated that (9) and (13) are mathematically equivalent when $\mathbf{w}$ possesses a zero mean and an identity covariance matrix [30], [33], [42]. In this case, the optimization problem whose solution specifies the sound speed estimate can be re-expressed in a stochastic framework as

$$\hat{\mathbf{c}} = \arg\min_{\mathbf{c}} \mathbf{E}_{\mathbf{w}} \left\{ \frac{1}{2} \parallel \underline{\mathbf{g}}^{\mathrm{w}} - \mathbf{M}\mathbf{H}^{\mathrm{c}}\mathbf{s}^{\mathrm{w}} \parallel^2 \right\} + \beta\mathcal{R}(\mathbf{c}), \quad (15)$$

which we refer to as the WISE method. An implementation of the WISE method that utilizes the stochastic gradient descent algorithm is summarized in Algorithm 2.

In Algorithm 2, the wave equation solver needs to be run one time in each of Lines 5 and 6. In the line search to determine the step size in Line 8, the wave equation solver needs to be run at least once, but in general will require a small number of additional runs, just as in Algorithm 1. Accordingly, the lower bound on the number of required wave equation solver runs per iteration is 3, as opposed to (3*M*) for the conventional sequential waveform inversion method described by Algorithm 1. As demonstrated in geophysics applications [29], [31], [41] and the breast imaging studies below, the WISE method provides a substantial reduction in reconstruction times over use of the standard sequential waveform inversion method. In Line 7 of Algorithm 2, $\mathbf{J}^{\mathrm{w}}$ can be calculated analogously to (10) as

$$[\mathbf{J}^{\mathrm{w}}]_n \approx \frac{1}{[\mathbf{c}]_n^3} \sum_{l=1}^{L-2} [\mathbf{q}^{\mathrm{w}}]_{nL+(L-l)} \frac{[\mathbf{p}^{\mathrm{w}}]_{nL+l-1} - 2[\mathbf{p}^{\mathrm{w}}]_{nL+l} + [\mathbf{p}^{\mathrm{w}}]_{nL+l+1}}{\Delta^{\mathrm{t}}},$$

$$(16)$$

where $\mathbf{p}^{\mathrm{w}} = \mathbf{H}^{\mathrm{c}}\mathbf{s}^{\mathrm{w}}$ and $\mathbf{q}^{\mathrm{w}} = \mathbf{H}^{\mathrm{c}}\boldsymbol{\tau}^{\mathrm{w}}$ with $\boldsymbol{\tau}^{\mathrm{w}} \in \mathbb{R}^{NL}$ calculated by

$$[\boldsymbol{\tau}^{\mathrm{w}}]_{nL+l} = \begin{cases} [\mathbf{M}\mathbf{p}^{\mathrm{w}} - \underline{\mathbf{g}}^{\mathrm{w}}]_{\mathcal{I}^{-1}(n)L+(L-l)}, & \text{if } n \in \mathbb{N}, \\ 0, & \text{otherwise} \end{cases}. \quad (17)$$

Here, we drop the subscript m of both $\mathcal{I}^{-1}(n)$ and $\mathbb{N}$ because we assume $\mathbf{M}$ to be identical for all data acquisitions. Various probability density functions have been proposed to describe the source encoding vector $\mathbf{w}$ [29], [31], [41]. In this study, we employed a Rademacher distribution as suggested by [29], in which case each element of $\mathbf{w}$ had a 50% chance of being either $+1$ or -1.

IV. DESCRIPTION OF COMPUTER SIMULATION STUDIES

Two-dimensional computer simulation studies were conducted to validate the WISE method for breast sound speed imaging and demonstrate its computational advantage over the standard sequential waveform inversion method.

A. Measurement Geometry

A circular measurement geometry was chosen to emulate a previously reported USCT breast imaging system [10], [23], [43]. As depicted in Fig. 1, 256 ultrasonic transducers were uniformly distributed on a ring of radius 110 mm. The generation of one USCT data set consisted of $M = 256$ sequential data acquisitions. In each data acquisition, one emitter produced an acoustic pulse. The acoustic pulse was numerically propagated through the breast phantom and the resulting wavefield data were recorded by all transducers in the array as described below. Note that the location of the emitter in every data acquisition was different from those in other acquisitions, whereas the locations of receivers were identical for all acquisitions.

B. Numerical Breast Phantom

A numerical breast phantom of diameter 98 mm was employed. The phantom was composed of 8 structures representing adipose tissues, parenchymal breast tissues, cysts, benign tumors, and malignant tumors, as shown in Fig. 2. For simplicity, the acoustic attenuation of all tissues was described by a power law with a fixed exponent $y = 1.5$ [44]. The corresponding sound speed and the attenuation slope values are listed in Table I [44]–[46]. Both the sound speed and the attenuation slope distributions in Fig. 2 were sampled on a uniform Cartesian grid with spacing $\Delta^{\mathrm{s}} = 0.25$ mm. The finest structure [indexed by 7 in Fig. 2(a)] was of diameter 3.75 mm.

C. Simulation of the Measurement Data

1) First-Order Numerical Wave Equation Solver: Acoustic wave propagation in acoustically absorbing media was modeled by three coupled first-order partial differential equations [47]:
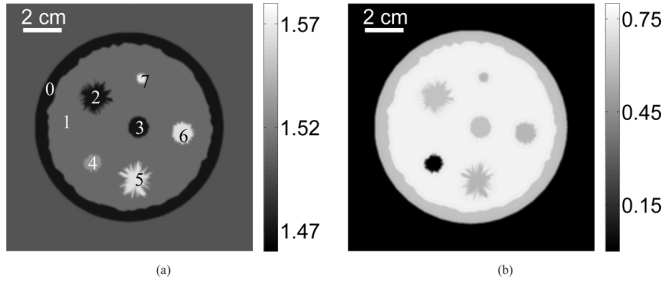
Fig. 2. (a) Sound speed map $(mm \cdot \mu s^{-1})$ and (b) acoustic attenuation slope map $[dB \cdot (MHz)^{-y} \cdot cm^{-1}]$ of the numerical breast phantom.

TABLE I. Parameters of the Numerical Breast Phantom [44]–[46].

Structure index	Tissue type	Sound speed $(mm \cdot \mu s^{-1})$	Slope of attenuation $[dB \cdot (MHz)^{-y} \cdot cm^{-1}]$
0	Adipose	1.47	0.60
1	Parenchyma	1.51	0.75
2	Benign tumor	1.47	0.60
3	Benign tumor	1.47	0.60
4	Cyst	1.53	0.00217
5	Malignant tumor	1.565	0.57
6	Malignant tumor	1.565	0.57
7	Malignant tumor	1.57	0.57

$$\frac{\partial}{\partial t}\mathbf{u}(\mathbf{r},t) = -\nabla p(\mathbf{r},t), \tag{18a}$$

$$\frac{\partial}{\partial t}\rho(\mathbf{r},t) = -\nabla \cdot \mathbf{u}(\mathbf{r},t) + 4\pi \int_0^t dt' s(\mathbf{r},t'), \tag{18b}$$

$$p(\mathbf{r},t) =$$
$$c^2(\mathbf{r})[1 + \tau(\mathbf{r})\frac{\partial}{\partial t}(-\nabla^2)^{y/2-1} + \eta(\mathbf{r})(-\nabla^2)^{(y+1)/2-1}]\rho(\mathbf{r},t), \tag{18c}$$

where $\mathbf{u}(\mathbf{r},t)$, $p(\mathbf{r},t)$, and $\rho(\mathbf{r})$ denote the acoustic particle velocity, the acoustic pressure, and the acoustic density, respectively. The functions $\tau(\mathbf{r})$ and $\eta(\mathbf{r})$ describe acoustic absorption and dispersion during the wave propagation [47]:

$$\tau(\mathbf{r}) = -2\alpha_0(\mathbf{r})c_0(\mathbf{r})^{y-1}, \quad \eta(\mathbf{r}) = 2\alpha_0(\mathbf{r})c_0(\mathbf{r})^y \tan(\pi y/2), \tag{19}$$

where $\alpha_0(\mathbf{r})$ and y are the attenuation slope and the power law exponent, respectively. When the medium is assumed to be lossless [i.e., $\alpha_0(\mathbf{r}) = 0$], it can be shown that (18) is equivalent to (1).

Based on (18), a pseudospectral k-space method was employed to simulate acoustic pressure data [36], [47]. This method was implemented by use of a first-order numerical scheme on GPU hardware. The calculation domain was of size 512×512 mm^2, sampled on a 2048×2048 uniform Cartesian grid of spacing $\Delta^s = 0.25$ mm. A nearest-neighbor interpolation was employed to place all

transducers on the grid points. On a platform consisting of dual quad-core CPUs with a 3.30 GHz clock speed, 64 GB of random-access memory, and a single NVIDIA Tesla K20 GPU, the first-order pseudospectral k-space method required approximately 108 s to complete one forward simulation.

2) Acoustic Excitation Pulse: The excitation pulse employed in this study was assumed to be spatially localized at the emitter location while temporally it was a $f_c = 0.8$ MHz sinusoidal function tapered by a Gaussian kernel with standard deviation $\sigma = 0.5$ µs, i.e.,

$$s_m(\mathbf{r},t) =$$
$$\begin{cases} \exp\left(-\frac{(t-t_c)^2}{2\sigma^2}\right)\sin(2\pi f_c t), & \text{at the } m\text{th emitter location,} \\ 0, & \text{otherwise,} \end{cases} \tag{20}$$

where $t_c = 3.2$ µs. The temporal profile and the amplitude frequency spectrum of the excitation pulse are plotted in Fig. 3(a) and (b), respectively. The excitation pulse contained approximately 3 cycles.

3) Generation of Non-Attenuated and Attenuated Noise-Free Data: For every data acquisition (indexed by m), the first-order pseudospectral k-space method was run for 3600 time steps with a time interval $\Delta^t = 0.05$ µs (corresponding to a 20 MHz sampling rate). Downsampling the recorded data by taking every other time sample resulted in a data vector $\mathbf{g}_m$ that was effectively sampled at 10 MHz and was of dimensions ML with $M = 256$ and $L = 1800$. The data vector at the zeroth data acquisition, $\mathbf{g}_0$, is displayed as a 2-D image in Fig. 4(a). This undersampling procedure was introduced to avoid *inverse crime* [48] so that the data generation and the image reconstruction employed different numerical discretization schemes. Repeating the calculation for $m = 0, 1, ..., 255$, we obtained a collection $\{\mathbf{g}_m\}$ of data vectors that together represented one complete data set. Using the absorption phantom described in Section IV-B, a complete attenuated data set was computed. An idealized, non-attenuated data set was also computed by setting $\alpha_0(\mathbf{r}) = 0$.
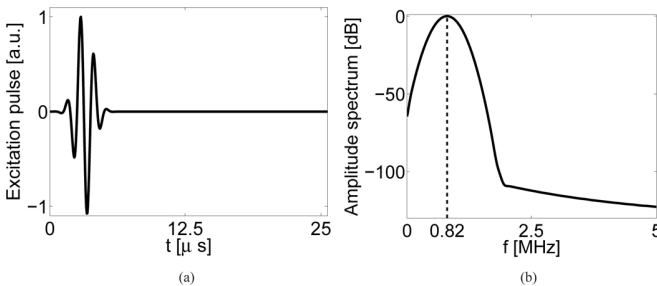

Fig. 3. (a) Normalized temporal profile and (b) amplitude spectrum of the excitation pulse employed in the computer simulation studies. The dashed line in (b) marks the center frequency of excitation pulse at 0.82 MHz.
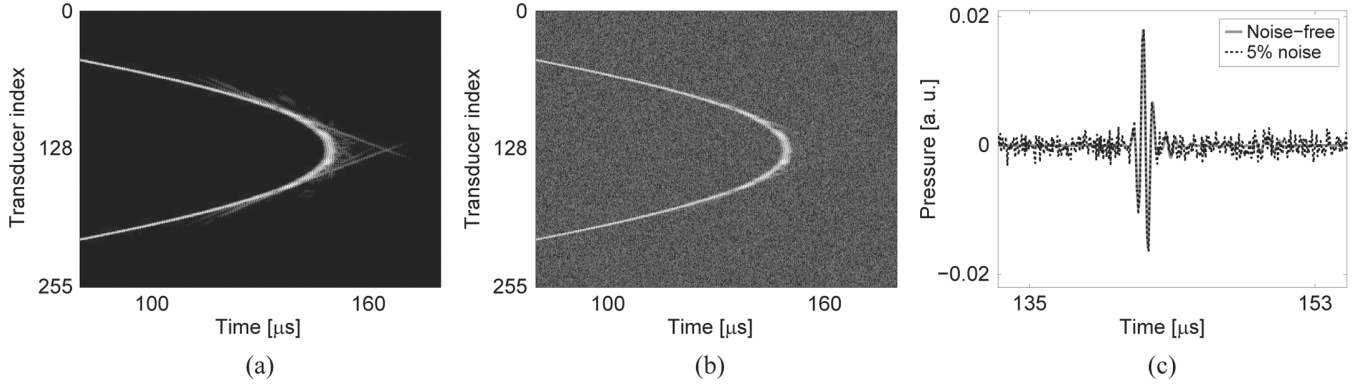
Fig. 4. Computer-simulated (a) noise-free and (b) noisy data vectors at the zeroth data acquisition. (c) Profiles of the pressure received by the 128th transducer. The grayscale window for (a) and (b) is $[-45, 0]$ dB.

4) Generation of Incomplete Data: An incomplete data set in this study corresponds to one in which only N^{rec} receivers located on the opposite side of the emitter record the pressure wavefield, with $N^{\text{rec}} < M$. Taking the zeroth data acquisition as an example (Fig. 1), only $N^{\text{rec}} = 100$ receivers, indexed from 78 to 177, record the wavefield, whereas other receivers record either unreliable or no measurements. Incomplete data sets formed in this way can emulate two practical scenarios: (1) Signals recorded by receivers near the emitter are unreliable and therefore discarded [23], and (2) an arc-shaped transducer array is employed that rotates with the emitter [13], [14], [49].

Specifically, incomplete data sets were generated as

$$[\mathbf{g}_m^{\text{incpl}}]_{n^{\text{rec}}L+l} = [\underline{\mathbf{g}}_m]_{\mathcal{J}_m(n^{\text{rec}})L+l}, \quad \text{for} \quad \begin{matrix} m = 0,1,\cdots,M-1 \\ n^{\text{rec}} = 0,1,\cdots,N^{\text{rec}}-1 \end{matrix}, \tag{21}$$

where $\mathbf{g}_m^{\text{incpl}}$ is the incomplete mth data acquisition, which is of dimensions $N^{\text{rec}}L$, with $N^{\text{rec}} < M$. The index map $\mathcal{J}_m : \{0,1,\cdots,N^{\text{rec}}-1\} \mapsto \mathbb{M}_m^{\text{good}}$ is defined as

$$\mathcal{J}_m(n^{\text{rec}}) = \left(m + n^{\text{rec}} + \frac{M - N^{\text{rec}}}{2}\right) \text{mod}\, M, \tag{22}$$

where $(m' \bmod M)$ calculates the remainder of m' divided by M, and the index set $\mathbb{M}_m^{\text{good}}$ collects indices of transducers that reliably record data at the mth data acquisition and is defined as

$$\mathbb{M}_m^{\text{good}} = \\ \{k \bmod M \mid k \in [m + (M - N^{\text{rec}})/2, m + (M + N^{\text{rec}})/2)\}. \tag{23}$$

Here, for simplicity, we assume that M and N^{rec} are even numbers. In this study, we empirically set $N^{\text{rec}} = 100$ so that the object can be fully covered by the fan region as shown in Fig. 1.

5) Generation of Noisy Data: An additive Gaussian white noise model was employed to simulate electronic measurement noise as

$$\tilde{\underline{\mathbf{g}}}_m = \underline{\mathbf{g}}_m + \tilde{\mathbf{n}}, \tag{24}$$

where $\tilde{\underline{\mathbf{g}}}_m$ and $\tilde{\mathbf{n}}$ are the noisy data vector and the Gaussian white noise vector, respectively. In this study, the maximum value of the pressure received by the 128th transducer at the zeroth data acquisition with a homogeneous medium (water tank) was chosen as a reference signal amplitude. The noise standard deviation was set to be 5% of this value. An example of a simulated noiseless and noisy data acquisition is shown Fig. 4.

D. Image Reconstruction

1) Second-Order Pseudospectral k-Space Method: In the reconstruction methods described below, the action of the operator $\mathbf{H}^c$ (5) was computed by solving (1) by use of a second-order pseudospectral k-space method. This was implemented using GPUs. The calculation domain was of size 512×512 mm^2, sampled on a 1024×1024 uniform Cartesian grid of spacing $\Delta^s = 0.5$ mm for reconstruction. On a platform consisting of dual octa-core CPUs with a 2.00 GHz clock speed, 125 GB RAM, and a single NVIDIA Tesla K20C GPU, the second-order k-space method required approximately 7 s to complete one forward simulation.

2) Sequential Waveform Inversion: To serve as a reference for the WISE method, we implemented the sequential waveform inversion method described in Algorithm 1. A uniform sound speed distribution was employed as the initial guess, which corresponded to the known background value of 1.5 mm/μs. The object was contained in a square region of interest (ROI) of dimension 128×128 mm^2 (Fig. 1), which was covered by 256×256 pixels.

3) WISE Method: We implemented the WISE method by use of Algorithm 2. Two types of penalties were employed in this study: a quadratic penalty expressed as

$$\mathcal{R}^{\text{Q}}(\mathbf{c}) = \sum_j \sum_i \{([\mathbf{c}]_{jN_x+i} - [\mathbf{c}]_{jN_x+i-1})^2 \\ + ([\mathbf{c}]_{jN_x+i} - [\mathbf{c}]_{(j-1)N_x+i})^2\}, \tag{25}$$

$$\mathcal{J}_m^{-1}(m^{\mathrm{rec}}) = \begin{cases} m^{\mathrm{rec}} - m - \dfrac{M - N^{\mathrm{rec}}}{2}, & \text{if } \dfrac{M - N^{\mathrm{rec}}}{2} \le m^{\mathrm{rec}} - m < \dfrac{M + N^{\mathrm{rec}}}{2} \\ m^{\mathrm{rec}} - m + \dfrac{M + N^{\mathrm{rec}}}{2}, & \text{if } \dfrac{-M - N^{\mathrm{rec}}}{2} \le m^{\mathrm{rec}} - m < \dfrac{-M + N^{\mathrm{rec}}}{2}. \end{cases} \tag{28}$$

where N_x and N_y denote the number of grid points along the x and y directions, respectively, and a total variation (TV) penalty, defined as [52], [53]

$$\mathcal{R}^{\mathrm{TV}}(\mathbf{c}) = \sum_j \sum_i \sqrt{\varepsilon + ([\mathbf{c}]_{jN_x+i} - [\mathbf{c}]_{jN_x+i-1})^2 + ([\mathbf{c}]_{jN_x+i} - [\mathbf{c}]_{(j-1)N_x+i})^2}, \tag{26}$$

where ε is a small number introduced to avoid dividing by 0 in the gradient calculation. In this study, we empirically selected $\varepsilon = 10^{-12}$. This value was fixed because we observed that it had a minor impact on the reconstructed images compared with the impact of β. The use of this parameter can be avoided when advanced optimization algorithms are employed [54], [55]. As in the sequential waveform inversion case, it was assumed that the background sound speed was known and the object was contained in a square ROI of dimension 128×128 mm^2 (Fig. 1), which corresponded to 256×256 pixels. The regularization parameters corresponding to the quadratic penalty and the TV penalty will be denoted by β^Q and β^{TV}, respectively. Optimal regularization parameter values should ultimately be identified by use of task-based measures of image quality [37]. In this preliminary study, we investigated the impact of β^Q and β^{TV} on the reconstructed images by sweeping their values over a wide range.

4) Reconstruction From Incomplete Data: Because the WISE method requires $\mathbf{M}_m$ to be identical for all m's, image reconstruction from incomplete data remains challenging [30], [33], [42]. In this study, two data completion strategies were investigated [30], [33], [42] to synthesize a complete data set, to which the WISE method could be effectively applied.

One strategy was to fill the missing data with pressure corresponding to a homogeneous medium as

$$[\underline{\mathbf{g}}_m^{\mathrm{combH}}]_{m^{\mathrm{rec}}L+l} = \begin{cases} [\underline{\mathbf{g}}_m^{\mathrm{incpl}}]_{\mathcal{J}_m^{-1}(m^{\mathrm{rec}})L+l}, & \text{if } m^{\mathrm{rec}} \in \mathbb{M}_m^{\mathrm{good}} \\ [\mathbf{g}_m^{\mathrm{h}}]_{m^{\mathrm{rec}}L+l}, & \text{otherwise,} \end{cases} \tag{27}$$

for $m^{\mathrm{rec}} = 0, 1, ..., M - 1$, where $\mathbf{g}_m^{\mathrm{h}} \in \mathbb{R}^{\mathrm{ML}}, \underline{\mathbf{g}}_m^{\mathrm{incpl}} \in \mathbb{R}^{N^{\mathrm{rec}}L}$, and $\underline{\mathbf{g}}_m^{\mathrm{combH}} \in \mathbb{R}^{\mathrm{ML}}$ denote the computer-simulated (with a homogeneous medium), the measured incomplete, and the combined complete data vectors at the mth data acquisition, respectively. The mapping $\mathcal{J}_m^{-1} : \mathbb{M}_m^{\mathrm{good}} \mapsto \{0, 1, \cdots, N^{\mathrm{rec}} - 1\}$ denotes the inverse operator of $\mathcal{J}_m$ as in (28), see above. This data completion

strategy is based on the assumption that the back-scatter from breast tissue in an appropriately sound speed-matched water bath is weak. This assumption suggests that the missing measurements can be replaced by the corresponding pressure data that would have been produced in the absence of the object.

The second, more crude, data completion strategy was to simply fill the missing data with zeros, i.e.,

$$[\underline{\mathbf{g}}_m^{\mathrm{comb0}}]_{m^{\mathrm{rec}}L+l} = \begin{cases} [\underline{\mathbf{g}}_m^{\mathrm{incpl}}]_{\mathcal{J}_m^{-1}(m^{\mathrm{rec}})L+l}, & \text{if } m^{\mathrm{rec}} \in \mathbb{M}_m^{\mathrm{good}} \\ 0, & \text{otherwise,} \end{cases} \tag{29}$$

where $\underline{\mathbf{g}}_m^{\mathrm{comb0}}$ denotes the data completed with the second strategy.

5) Bent-Ray Image Reconstruction: A bent-ray method was also employed to reconstruct images. Details regarding the TOF estimation and algorithm implementation are provided in Appendix C.

V. Computer Simulation Results

A. Images Reconstructed From Idealized Data

The images reconstructed from the noise-free, non-attenuated data by use of the WISE method with 199 iterations and the sequential waveform inversion method with 43 iterations are shown in Fig. 5(a) and (b). As expected [23], [56], both images are more accurate and possess higher spatial resolution than the one reconstructed by use of the bent-ray reconstruction algorithm displayed in Fig. 5(c). Profiles through the reconstructed images are displayed in Fig. 6. The images shown in Fig. 5(a) and (b) possess similar accuracies as measured by their root-mean-square errors (RMSEs), namely, 1.08×10^{-3} for the former and 1.19×10^{-3} for the latter. The RMSE was computed as the Euclidean distance between the reconstructed image and the sound speed phantom vector $\mathbf{c}$, averaged by the 256×256 pixels of the ROI sketched in Fig. 1. However, the reconstruction of Fig. 5(a) required only about 1.7% of the computational time required to reconstruct Fig. 5(b), namely, 1.4 hours for the former and 81.4 hours for the latter. This is because the WISE method required only 1018 wave equation solver runs, which is significantly less than the 57 088 wave equation solver runs required by the sequential waveform inversion method. With a similar number of wave equation solver runs (e.g., 1024), one can
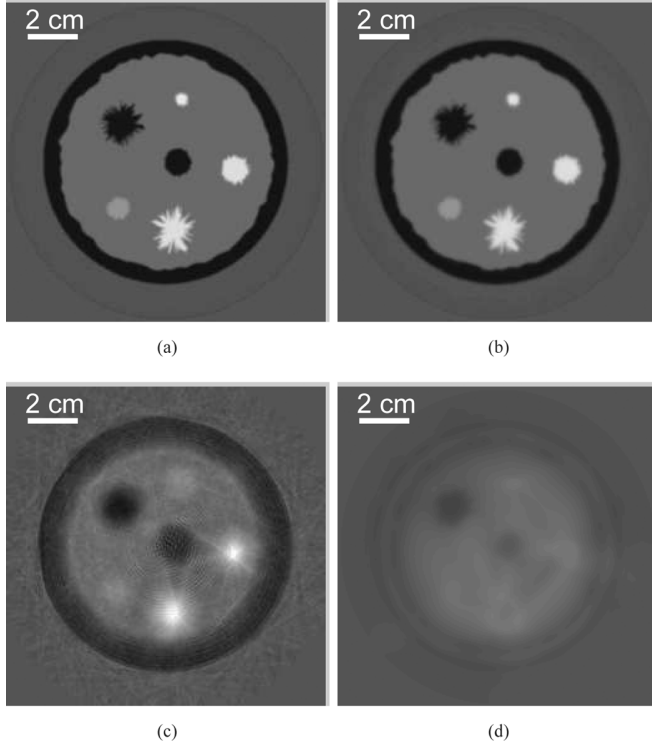
(a)   (b)

(c)   (d)

Fig. 5. Images reconstructed by use of (a) the WISE method after the 199th iteration (1018 runs of the wave equation solver), (b) the sequential waveform inversion algorithm after the 43rd iteration (57 088 runs of the wave equation solver), (c) the bent-ray model-based sound speed reconstruction method, and (d) the sequential waveform inversion algorithm after the first iteration (1024 runs of the wave equation solver) from the noise-free non-attenuated data. The grayscale window is [1.46, 1.58] mm/μs.
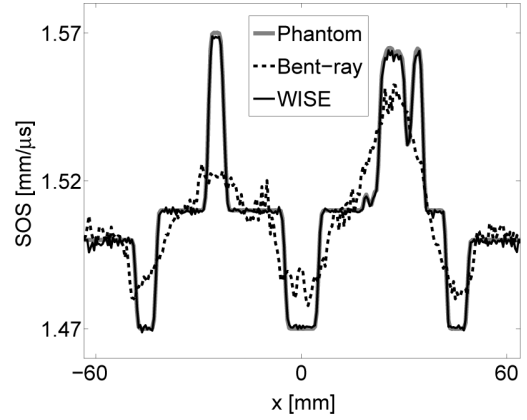

Fig. 6. Profiles at $y = 6.5$ mm of the images reconstructed by use of the bent-ray TOF image reconstruction method and the WISE method from the noise-free non-attenuated data.

complete only a single algorithm iteration by use of the sequential waveform inversion method. The corresponding image, shown in Fig. 5(d), lacks quantitative accuracy as well as qualitative value for identifying features. The results suggest that the WISE method maintains the advantages of the sequential waveform inversion method while significantly reducing the computational time.

B. Convergence of the WISE Method

Images reconstructed from noise-free, non-attenuated, data by use of the WISE method contain radial streak artifacts when the algorithm iteration number is less than 100, as shown in Figs. 7(a) to (c). Profiles through these images are displayed in Fig. 8. The streak artifacts are likely caused by crosstalk introduced during the source encoding procedure [31], [41]. However, these artifacts are effectively mitigated after more iterations as demonstrated by the image reconstructed after the 199th iteration in Fig. 5(a) and its profile in Fig. 6. The quantitative accuracy of the reconstructed images is improved with more iterations as shown in Fig. 8.

Fig. 9(a) reveals that the WISE method requires a larger number of algorithm iterations than does the sequential waveform inversion method to achieve the same RMSE.

The RMSE of the images reconstructed by use of the WISE method appears to oscillate around 1.0×10^{-3} after the first 100 iterations, whereas the sequential waveform inversion method can achieve a lower RMSE. However, as shown previously in Fig. 5(a) and the corresponding profile in Fig. 6, after additional iterations the image reconstructed by use of the WISE method achieves a high accuracy. Moreover, to achieve the same accuracy as the sequential waveform inversion method, the WISE method requires a computation time that is reduced by approximately 2 orders of magnitude, as suggested by Fig. 9(b). We also plotted the cost function value against the number of iterations in Fig. 9(c). Note that for the WISE method, the cost function value was approximated by the current realization of $\left\| \mathbf{\underline{g}}^{\mathrm{w}} - \mathbf{MH}^{\mathrm{c}}\mathbf{s}^{\mathrm{w}} \right\|^2/2$. These plots suggest that, in this particular case, the WISE method appears to approximately converge after 200 iterations. For example, the images reconstructed after 199 [Fig. 5(a)] and 250 [Fig. 7(d)] iterations are nearly identical.

C. Images Reconstructed From Non-Attenuated Data Containing Noise

Images reconstructed by use of the WISE method with a quadratic penalty and the WISE method with a TV penalty from noisy, non-attenuated data are presented in Fig. 10. All images were obtained after 1024 algorithm iterations. The WISE method with a quadratic penalty effectively mitigates image noise as shown in Figs. 10(a) to (c), at the expense of image resolution, as expected. Fig. 10(d) shows an image reconstructed by use of the WISE method with a TV penalty. The image appears to possess a similar resolution but a lower noise level than the image in Fig. 10(b) that was reconstructed by use of the WISE method with a quadratic penalty. We also compared the convergence rates of the WISE method and the sequential waveform inversion methods when both utilize a TV penalty and the same regularization parameter. As shown in Fig. 11, the convergence properties of the penalized meth-

(a)   (b)
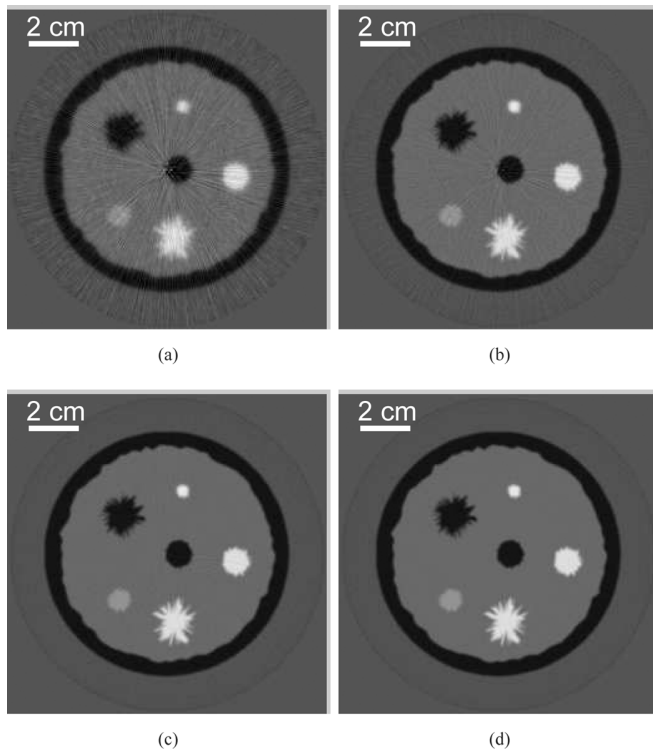
(c)   (d)

Fig. 7. Images reconstructed by use of the WISE method after (a) the 20th, (b) the 50th, (c) the 100th, and (d) the 250th iteration from the noise-free, non-attenuated data set. The grayscale window is [1.46, 1.58] mm/μs.

ods follow similar trends as the un-penalized methods, which were discussed above and shown in Fig. 9. Even though it required a larger number of algorithm iterations, the WISE method reduced the computation time by approximately 2 orders of magnitude as compared with the sequential waveform inversion method.

D. Images Reconstructed From Acoustically Attenuated Data

Our current implementation of the WISE method assumes an absorption-free acoustic medium. This assump-
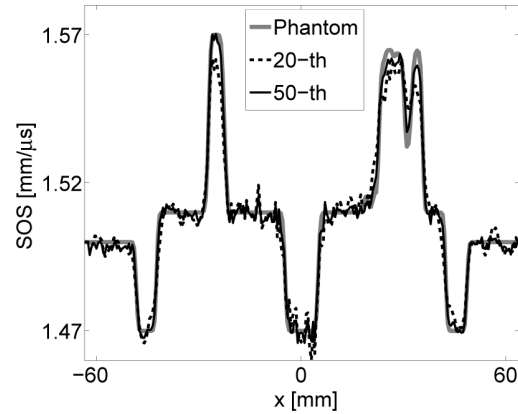
Fig. 8. Profiles of the images reconstructed by use of the WISE method from the noise-free non-attenuated data after different numbers of iterations.

tion can be strongly violated in practice. To investigate the robustness of the WISE method to model errors associated with ignoring medium acoustic absorption, we applied the algorithm to the acoustically attenuated data that were produced as described in Section IV-C. As shown in Fig. 12, when acoustic absorption is considered, the amplitude of the measured pressure is attenuated by approximately a factor of 2. The wavefront [Fig. 12(a)] remains very similar to that when medium absorption is ignored [Fig. 4(a)]. Medium absorption has the largest impact on the pressure data received by transducers located opposite the emitter as shown in Fig. 12(b). The shape of the pulse profile remains very similar as shown in Figs. 12(c) and (d), suggesting that waveform dispersion may be less critical than amplitude attenuation in image reconstruction for this phantom.

Images reconstructed by use of the WISE method with a TV penalty from noise-free and noisy attenuated data are shown in Figs. 13(a) and (b). Image profiles are shown in Fig. 13(c). Although these images contain certain artifacts that were not produced in the idealized data studies, most object structures remain readily identified. These results suggest that the WISE method with a TV penalty can tolerate data inconsistencies associated with neglect-

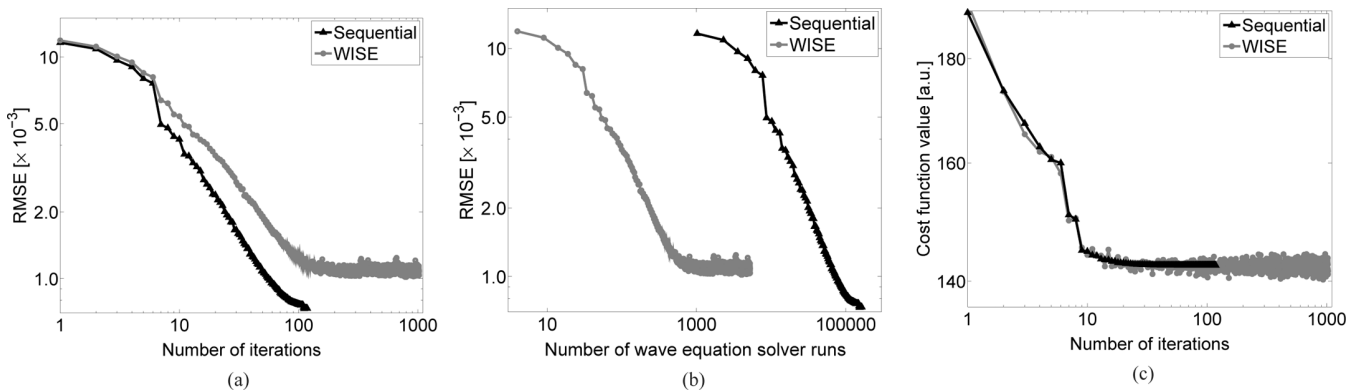(a)   (b)   (c)

Fig. 9. Plots of the root mean square errors (RMSEs) of the images reconstructed from the noise-free data versus (a) the number of iterations and (b) the number of wave equation solver runs. (c) Plots of the cost function value versus the number of iterations.
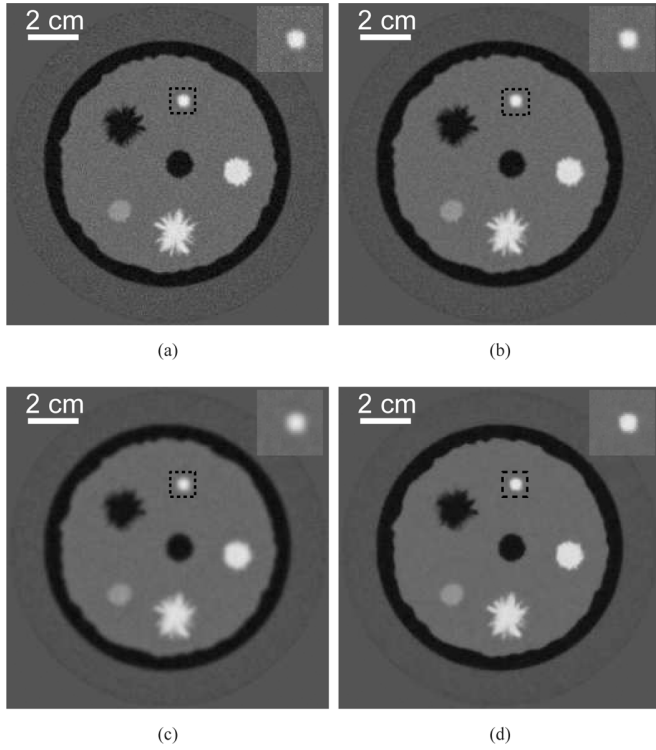
Fig. 10. Images reconstructed from non-attenuated data contaminated with Gaussian random noise. Images (a) to (c) were reconstructed by use of the WISE method with a quadratic penalty with $\beta^Q = 1.0 \times 10^{-3}$, 1.0×10^{-2}, and 1.0×10^{-1}, respectively. Image (d) was reconstructed by use of the WISE method with a TV penalty with $\beta^{TV} = 5.0 \times 10^{-4}$. The insert in the up right corner of each image is the zoomed-in image of the dashed black box, which contains 35×35 pixels (17.5×17.5 mm^2). The grayscale window is [1.46, 1.58] mm/μs.

ing acoustic attenuation in the imaging model, at least to a certain level with regard to feature detection tasks.

E. Images Reconstructed From Idealized Incomplete Data

The wavefront of the noise- and attenuation-free pressure wavefield when the object is absent [Fig. 14(a)] ap-

pears to be very similar to that when the object is present [Fig. 4(a)]. As expected, the largest differences are seen in the signals received by the transducers located opposite of the emitter, as shown in Fig. 14(b). As seen in Fig. 14(c), the time traces received by the 40th transducer are nearly identical when object is present and absent. This is because the back-scattered wavefield is weak for breast imaging applications. These results establish the potential efficacy of the data completion strategy of filling the missing data with the pressure data corresponding to a water bath.

The image reconstructed from the measurements completed with pressure data corresponding to a water bath is shown in Fig. 15(a). As revealed by the profile in Fig. 15(c), this image is highly accurate. Alternatively, the image reconstructed from the data completed with zeros contains strong artifacts as shown in Fig. 15(b). These results suggest that the WISE method can be adapted to reconstruct images from incomplete data, which is particularly useful for emerging laser-induced USCT imaging systems [13]–[15].

VI. Experimental Validation

A. Data Acquisition

Experimental data recorded by use of the SoftVue USCT scanner [57] were utilized to further validate the WISE method. The scanner contained a ring-shaped array of radius 110 mm that was populated with 2048 transducer elements. Each element had a center frequency of 2.75 MHz, a pitch of 0.34 mm, and was elevationally focused to isolate a 3-mm-thick slice of the to-be-imaged object. The transducer array was mounted in a water tank and could be translated with a motorized gantry in the vertical direction. See [57] for additional details regarding the system.

The breast phantom was built by Dr. Ernie Madsen from the University of Wisconsin and provides tissue-
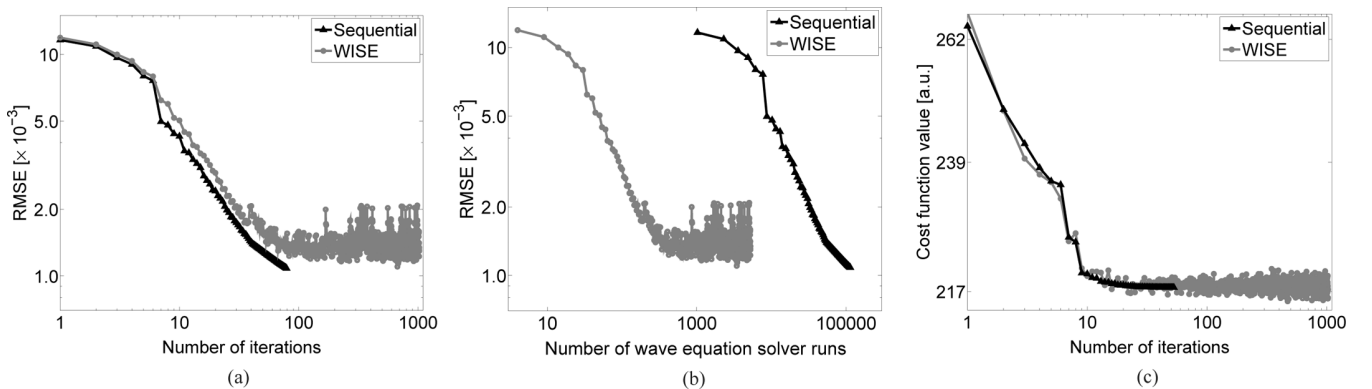

Fig. 11. Plots of the root-mean-square errors (RMSEs) of the images reconstructed from the noisy data versus (a) the number of iterations and (b) the number of wave equation solver runs. (c) Plots of the cost function value versus the number of iterations. Both the WISE and the sequential waveform inversion methods employed a TV penalty with $\beta^{TV} = 5.0 \times 10^{-4}$.
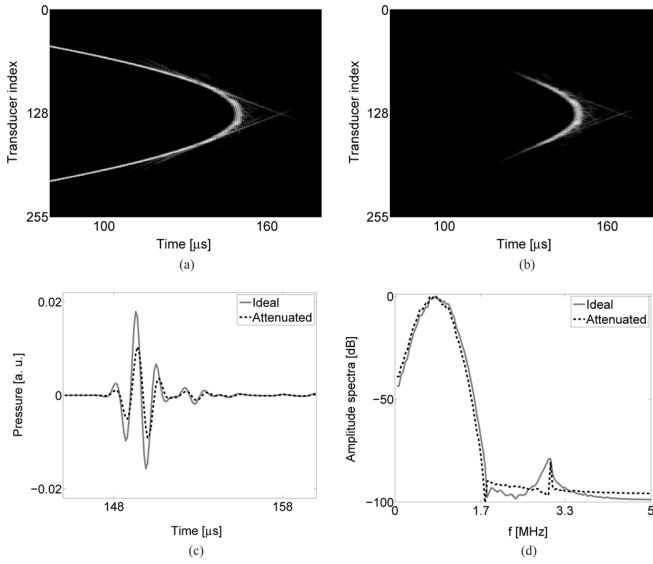
Fig. 12. (a) Computer-simulated noise-free attenuated pressure of the zeroth data acquisition. (b) The difference between the attenuated pressure data and the non-attenuated pressure data. (c) The temporal profiles and (d) the amplitude spectra of the pressure received by the 128th transducer. The grayscale window for (a) and (b) is [−45, 0] dB.

equivalent characteristics of highly scattering, predominantly parenchymal breast tissue. The phantom mimics the presence of benign and cancerous masses embedded in glandular tissue, including a subcutaneous fat layer. Fig. 16 displays a schematic of one slice through the phantom. The diameter of the inclusions is approximately 12 mm. Table II presents the known acoustic properties of the phantom.

During data acquisition, the breast phantom was placed near the center of the ring-shaped transducer array so that the distance between the phantom and each transducer was approximately the same. While scanning each slice, every other transducer element sequentially emits fan beam ultrasound signals toward the opposite side of the ring. The forward-scattered and back-scattered ultrasound signals are subsequently recorded by the same transducer elements. The received waveform was sampled at a rate of 12 MHz. The 1024 data acquisitions required approximately 20 s in total. A calibration data set was also acquired in which the phantom object was absent.
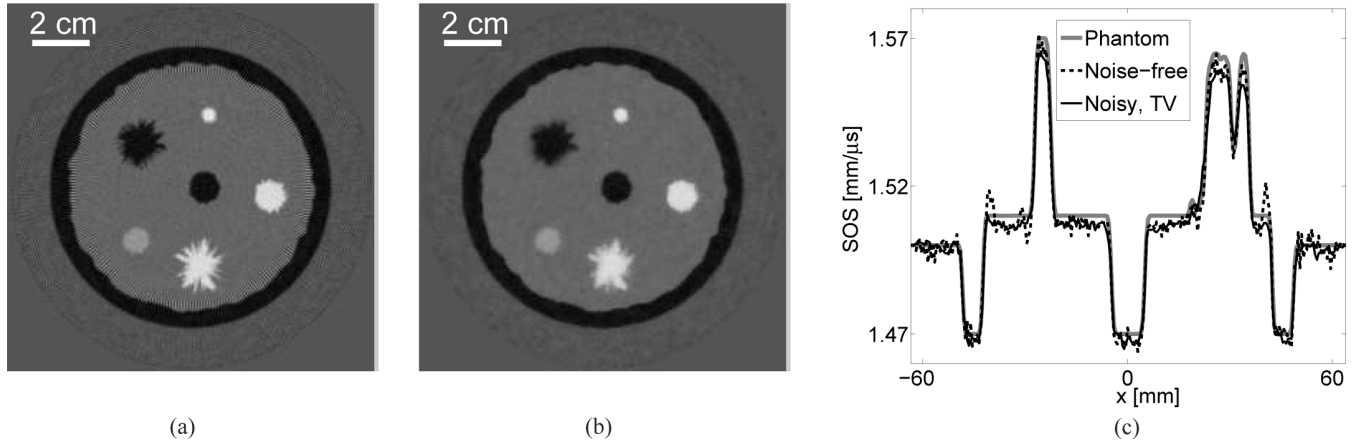

Fig. 13. (a) Image reconstructed by use of the WISE method from the noise-free attenuated data. (b) Image reconstructed by use of the WISE method with a TV penalty with $\beta^{TV} = 5.0 \times 10^{-4}$, from the noisy attenuated data. The grayscale window is [1.46, 1.58] mm/μs. (c) Profiles at $y = 6.5$ mm of the reconstructed images.
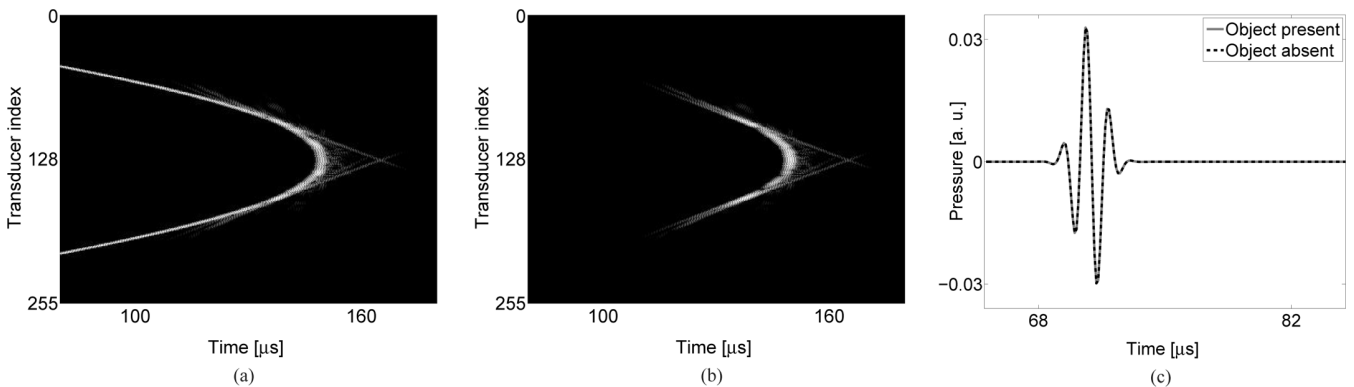

Fig. 14. (a) Computer-simulated noise-free non-attenuated pressure data when the object is absent. (b) The difference between the pressure data when object is present and the pressure data when the object is absent. (c) Profiles of the pressure received by the 40th transducer. The grayscale window for (a) and (b) is [−45, 0] dB.
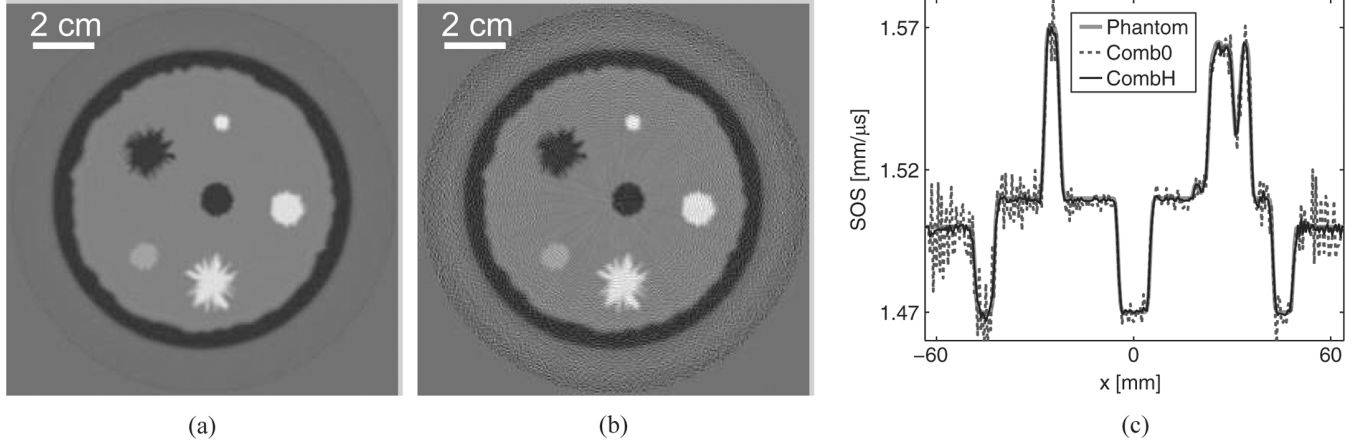
Fig. 15. Images reconstructed by use of the WISE method from noise-free combined data that are completed (a) with computer-simulated pressure corresponding to a homogeneous medium and (b) with zeros. The grayscale window is [1.46, 1.58] mm/μs. (c) Profiles at $y = 6.5$ mm of the images reconstructed by use of the WISE method from the two combined data sets.

B. Data Pre-Processing

Forty-eight bad channels were manually identified by visual inspection. After discarding these, the data set contained $M = 976$ acquisitions. Each acquisition contained $N^{\text{rec}} = 976$ time traces. Each time trace contained $L = 2112$ time samples. The 976 good channels were indexed from 0 to 975. The corresponding data acquisitions were indexed in the same way. A Hann-window low-pass filter with a cutoff frequency of 4 MHz was applied to every time trace in both the calibration and the measurement data. This data filtering was implemented to mitigate numerical errors that could be introduced by our second-order wave equation solver.

C. Estimation of Excitation Pulse

The shape of the excitation pulse was estimated as the time trace of the calibration data (after pre-processing) received by the 488th receiver at the zeroth data acquisition. Note that the 488th receiver was approximately located on the axis of the zeroth emitter, thus the received pulse was minimally affected by the finite aperture size effect of the transducers. Because our calibration data and measurement data were acquired using different electronic amplifier gains, the amplitude of the excitation pulse was estimated from the measurement data. More specifically, we simulated the zeroth data acquisition using the second-order pseudospectral k-space method and compared the simulated time trace received by the 300th receiver with the corresponding measured time trace (after preprocessing). The ratio between the maximum values of these two traces was used to scale the excitation pulse shape. We selected the 300th receiver because it resided out of the fan region indicated in Fig. 1; its received signals were unlikely to be strongly affected by the presence of the object. The estimated excitation pulse and its amplitude spectrum are displayed in Fig. 17. Note that the experimental excitation pulse contained higher frequency components than did the computer-simulated excitation pulse shown in Fig. 3.

D. Synthesis of Combined Data

As discussed in Section IV-C-4, signals received by receivers located near the emitter can be unreliable [23]. Our experimental data, as shown in Fig. 18(a), contained noise-like measurements for the receivers indexed from 0 to 200, and from 955 to 975, in the case where the zeroth transducer functioned as the emitter. Also, our point-like transducer assumption introduces larger model mismatch-
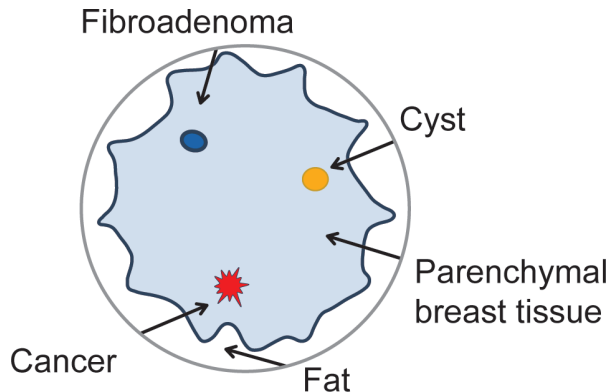

Fig. 16. Schematic of the breast phantom employed in the experimental study.

TABLE II. PARAMETERS OF THE EXPERIMENTAL BREAST PHANTOM.

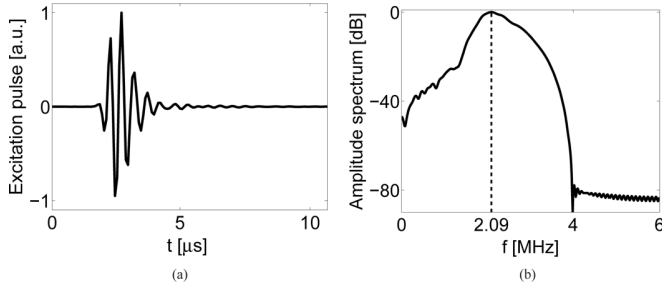| Material	Sound speed (mm·μs^{-1})	Attenuation coefficient at 2.5 MHz (dB/cm)
Fat	1.467	0.48
Parenchymal tissue	1.552	0.89
Cancer	1.563	1.20
Fibroadenoma	1.552	0.52
Gelatin cyst	1.585	0.16

Fig. 17. (a) Normalized temporal profile and (b) amplitude spectrum of the excitation pulse employed in the experimental studies. The dashed line in (b) marks the center frequency of excitation pulse at 2.09 MHz.

es for the receivers located near the emitter. As shown in Figs. 18(c) and (d), even though the simulated time trace received by the 300th receiver matches accurately with the experimentally measured one, the simulated time trace received by the 200th receiver is substantially different compared with the experimentally measured one. To minimize the effects of model mismatch, we replaced these unreliable measurements with computer-simulated water bath data, as described in Section IV-C. We designated the time traces received by the 512 receivers located on the opposite side of the emitter as the reliable measurements for each data acquisition. The zeroth data acquisition of the combined data is displayed in Fig. 18(b).

E. Estimation of Initial Guess

The initial guess for the WISE method was obtained by use of the bent-ray reconstruction method described in Appendix C. We first filtered each time trace of the raw data by a band-pass Butterworth filter (0.5–2.5 MHz).
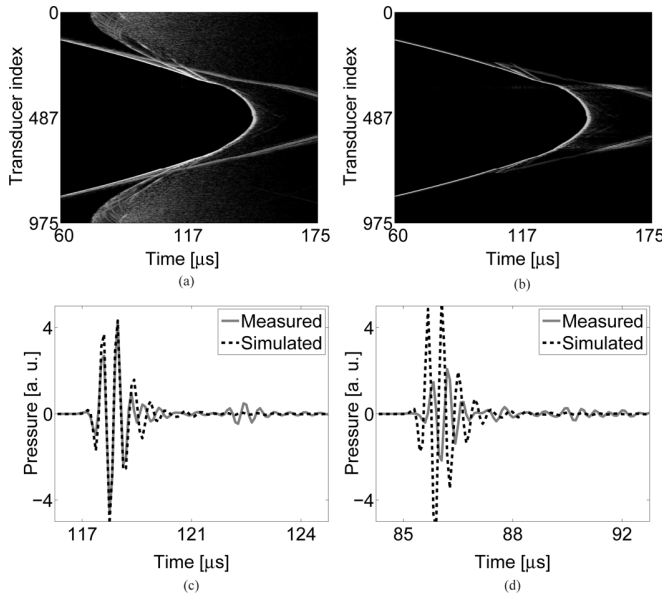

Fig. 18. Zeroth acquisition of (a) the experimentally measured raw data and (b) the combined data, and time traces at the zeroth acquisition received by (c) the 300th receiver, and (d) the 200th receiver. The grayscale window for (a) and (b) is [−45, 0] dB.
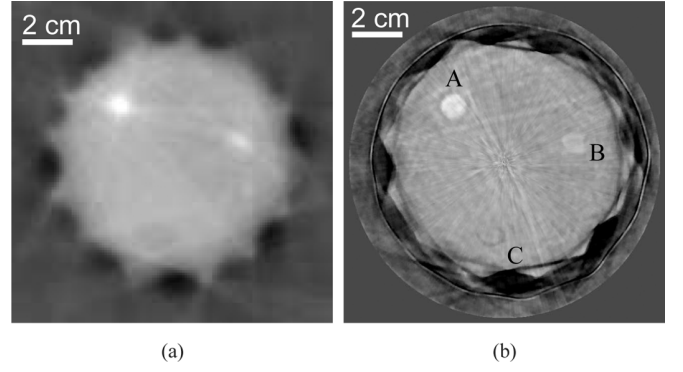

Fig. 19. Images reconstructed from the experimentally measured phantom data by use of (a) the bent-ray model-based sound speed reconstruction method and (b) the WISE method with a TV penalty (β^{TV} = 1.0×10^2) after the 200th iteration. The grayscale window is [1.49, 1.57] mm/μs.

Subsequently, we extracted the TOF by use of the thresholding method with a thresholding value of 20% of the peak value of each time trace. The bent-ray reconstruction algorithm was applied for image reconstruction with a measured background sound speed of 1.513 mm/μs. The resulting image is shown in Fig. 19(a) and has a pixel size of 1 mm. Finally, the image was smoothed by convolving it with a 2-D Gaussian kernel with a standard deviation of 2 mm.

F. Image Reconstruction

We applied the WISE method with a TV penalty to the combined data set. The second-order wave equation solver was employed with a calculation domain of dimensions 512.0×512.0 mm^2. The calculation domain was sampled on a 2560×2560 Cartesian grid with a grid spacing of 0.2 mm. On a platform consisting of dual quad-core CPUs with a 3.30 GHz clock speed, 64 GB RAM, and a single NVIDIA Tesla K20 GPU, each numerical solver run took 40 s to calculate the pressure data for 2112 time samples. Knowing the size of the phantom, we set the reconstruction region to be within a circle of diameter 128 mm (i.e., only the sound speed values of pixels within the circle were updated during the iterative image reconstruction). We swept the value of β^{TV} over a wide range to investigate its impact on the reconstructed images.

G. Images Reconstructed From Experimental Data

As shown in Fig. 19, the spatial resolution of the image reconstructed by use of the WISE method with a TV penalty is significantly higher than that reconstructed by use of the bent-ray model-based method. In particular, the structures labeled A and B possess clearly defined boundaries. This observation is further confirmed by the profiles of the two images shown in Fig. 20. In addition, the structure labeled C in Fig. 19(b) is almost indistinguishable in the image reconstructed by use of the bent-ray model-based method [Fig. 19(a)]. The improved spatial resolu-

tion is expected because the WISE method takes into account high-order acoustic diffraction, which is ignored by the bent-ray method [23]. Though not shown here, for the bent-ray method, we investigated multiple TOF pickers [25] and systematically tuned the regularization parameter. As such, it is likely that Fig. 19(a) represents a nearly optimal bent-ray image in terms of the resolution. This resolution also appears to be similar to previous experimental results reported in the literature [26].

The convergence properties of the WISE method with a TV penalty with experimental data were consistent with those observed in the computer simulation studies. Images reconstructed by use of 10, 50, and 300 algorithm iterations are displayed in Fig. 21. The image reconstructed by use of 10 iterations contains radial streak artifacts that are similar in nature to those observed in the computer simulation studies. These artifacts were mitigated after more iterations. The image reconstructed after 300 iterations [Fig. 21(d)] appears to be similar to that after 200 iterations [Fig. 19(b)], suggesting that the WISE method with a TV penalty is close to convergence after about 200 iterations. The time required to complete 200 iterations was approximately 14 hours. The estimated time it would take for the sequential waveform inversion method to produce a comparable image is approximately 1 month, assuming the same number of iterations is required as in the computer simulation studies (i.e., 40).

Despite the nonlinearity of the WISE method, the impact of the TV penalty appears to be similar to that observed in other imaging applications [54], [58] (Fig. 22). Though not shown here, the impact of the quadratic penalty is also similar. As expected, a larger value of β reduced the noise level at the expense of spatial image resolution. These results suggest a predictable impact of the penalties on the images reconstructed by use of the WISE method.
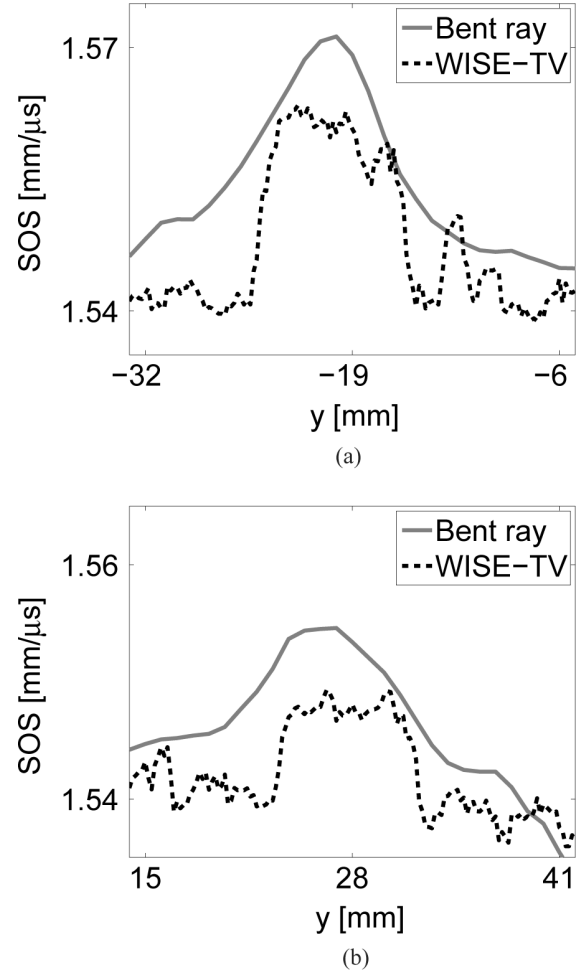

(a)

(b)

Fig. 20. Profiles at (a) $x = -24.0$ mm and (b) $x = 10.0$ mm of the reconstructed images by use of the bent-ray model-based sound speed reconstruction method (light solid) and the WISE method with a TV penalty with $\beta^{\mathrm{TV}} = 1.0 \times 10^2$ (dark dashed) from experimentally measured data.

VII. SUMMARY

It is known that waveform inversion-based reconstruction methods can produce sound speed images that possess improved spatial resolution properties over those produced by ray-based methods. However, waveform inversion methods are computationally demanding and have not been applied widely in USCT breast imaging. In this work, based on the time-domain wave equation and motivated by recent mathematical results in the geophysics literature, the WISE method was developed that circumvents the large computational burden of conventional waveform inversion methods. This method encodes the measurement data using a random encoding vector and determines an estimate of the sound speed distribution by solving a stochastic optimization problem by use of a stochastic gradient descent algorithm. With our current GPU-based implementation, the computation time was reduced from weeks to hours. The WISE method was systematically investigated in computer simulation and experimental studies involving a breast phantom. The results suggest that the method holds value for USCT breast imaging applications in a practical setting.

Many opportunities remain to further improve the performance of the WISE method. As shown in Fig. 19, images reconstructed by use of the WISE method can contain certain artifacts that are not present in the image reconstructed by use of the bent-ray method. An example of such an artifact is the dark horizontal streak below the structure C. Because of the nonlinearity of the image reconstruction problem, it is challenging to determine whether these artifacts are caused by imaging model errors or by the optimization algorithm, which might have arrived at a local minimum of the cost function. A more accurate imaging model can be developed to account for out-of-plane scattering, the transducer finite aperture size effect, acoustic absorption, as well as other physical factors. Also, the stochastic gradient descent algorithm is one of the most basic stochastic optimization algorithms. Numerous emerging optimization algorithms can be employed [33], [42] to improve the convergence rate. In ad-
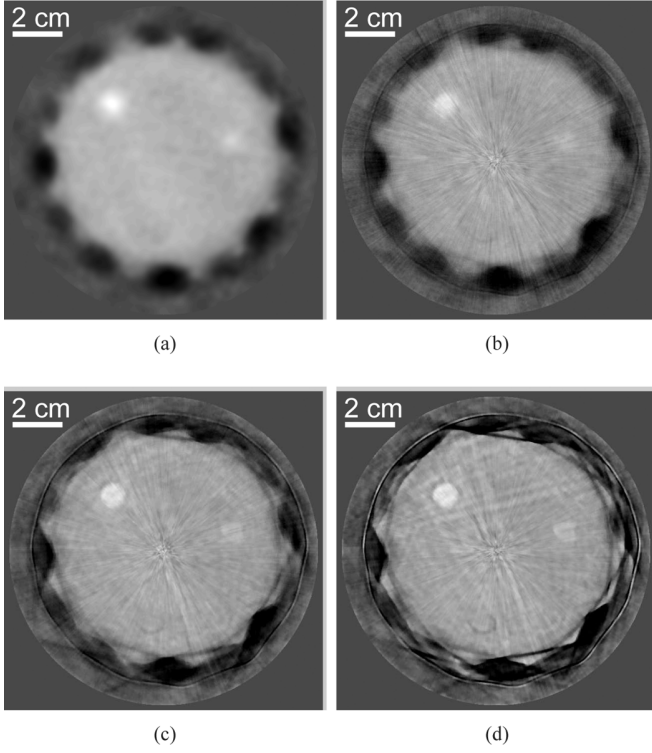
(a)   (b)

(c)   (d)

Fig. 21. (a) The initial guess of the sound speed map and the images reconstructed by use of the WISE method with a TV penalty with (β^{TV} = 1.0×10^2) after (b) the 10th, (b) the 50th, and (d) the 300th iteration, from the experimentally measured phantom data. The grayscale window is [1.49, 1.57] mm/μs.

dition, there remains a great need to compare the WISE method with other existing sound speed reconstruction algorithms [19], [40].

There remains a need to conduct additional investigations of the numerical properties of the WISE method. Currently, a systematic comparison of the statistical properties of the WISE and the sequential waveform inversion method is prohibited by the excessively long computation times required by the latter method. This comparison
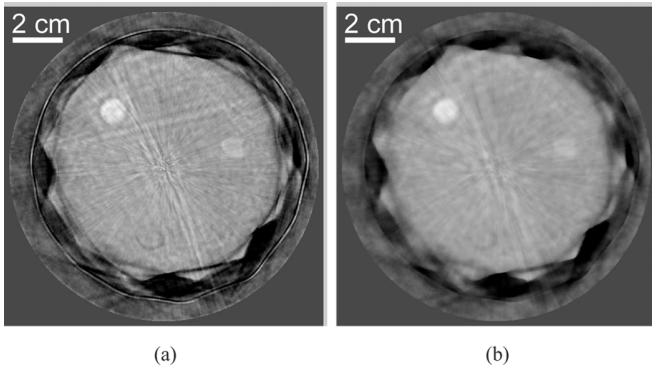

(a)   (b)

Fig. 22. Images reconstructed by use of the WISE method with a TV penalty with (a) β^{TV} = 5.0×10^1, and (b) β^{TV} = 5.0×10^2, from the experimentally measured phantom data. The grayscale window is [1.49, 1.57] mm/μs.

will be interesting when a more efficient wave equation solver is available. Given the fact that waveform inversion is nonlinear and sensitive to the initial guess, it becomes important to investigate how to obtain an accurate initial guess. We also observed that the performance of the WISE method is sensitive to how strong the medium heterogeneities are and the profile of the excitation pulse. An investigation of the impact of the excitation pulse the numerical properties of the image reconstruction may help optimize hardware design. In addition, quantifying the statistics of the reconstructed images will allow application of task-based measures of image quality to be applied to guide system optimization studies.

APPENDIX A
CONTINUOUS-TO-DISCRETE USCT IMAGING MODEL

In practice, each data function $g_m(\mathbf{r},t)$ is spatially and temporally sampled to form a data vector $\mathbf{g}_m \in \mathbb{R}^{N^{\mathrm{rec}}L}$, where N^{rec} and L denote the number of receivers and the number of time samples, respectively. We will assume that N^{rec} and L do not vary with excitation pulse. Let $[\mathbf{g}_m]_{n^{\mathrm{rec}}L+l}$ denotes the $(n^{\mathrm{rec}}L + 1)$th element of $\mathbf{g}_m$. When the receivers are point-like, $\mathbf{g}_m$ is defined as

$$[\mathbf{g}_m]_{n^{\mathrm{rec}}L+l} = g_m(\mathbf{r}(m, n^{\mathrm{rec}}), l\Delta^{\mathrm{t}}), \qquad (30)$$

where the indices n^{rec} and l specify the receiver location and temporal sample, respectively, and Δ^{t} is the temporal sampling interval. The vector $\mathbf{r}(m, n^{\mathrm{rec}}) \in \Omega_m$ denotes the location of the n^{rec}th receiver at the mth data acquisition.

A C-D imaging model for USCT describes the mapping of $c(\mathbf{r})$ to the data vector $\mathbf{g}_m$ and can be expressed as

$$[\mathbf{g}_m]_{n^{\mathrm{rec}}L+l} = \mathcal{M}_m \mathcal{H}^c s_m(\mathbf{r}, t)\mid_{\mathbf{r}=\mathbf{r}(m,n^{\mathrm{rec}}), t=l\Delta^{\mathrm{t}}}$$
$$\text{for} \quad \begin{matrix} n^{\mathrm{rec}} = 0,1,\cdots,N^{\mathrm{rec}}-1 \\ l = 0,1,\cdots,L-1. \end{matrix} \qquad (31)$$

Note that the acousto-electrical impulse response [59] of the receivers can be incorporated into the C-D imaging model by temporally convolving $s_m(\mathbf{r},t)$ in (1) with the receivers' acousto-electrical impulse response if we assume all receiving transducers share an identical acousto-electrical impulse response.

APPENDIX B
FRÉCHET DERIVATIVE OF DATA FIDELITY TERM

Consider the integrated squared-error data misfit function [22], [23],

$$\mathcal{F}^{\mathrm{CC}}(c) = \frac{1}{2}\sum_{m=0}^{M-1}\int_{\Omega_m} d\mathbf{r}\int_0^T dt[\underline{g_m}(\mathbf{r},t) - g_m(\mathbf{r},t)]^2, \qquad (32)$$

where $\underline{g_m}(\mathbf{r},t)$ and $g_m(\mathbf{r},t)$ denote the measured data function and the predicted data function computed by use of (3) with the current estimate of $c(\mathbf{r})$.

Both the sequential and WISE reconstruction method described in Section III require knowledge of the Fréchet derivatives of $\mathcal{F}^{\mathrm{CC}}(c)$ and $\mathcal{R}^{\mathrm{CC}}(c)$ with respect to c, denoted by $\nabla_c \mathcal{F}^{\mathrm{CC}}$ and $\nabla_c \mathcal{R}^{\mathrm{CC}}$, respectively. The calculation of $\nabla_c \mathcal{R}^{\mathrm{CC}}$ can be readily accomplished for quadratic smoothness penalties [54], [60]. For the integrated squared error data misfit function given in (32), $\nabla_c \mathcal{F}^{\mathrm{CC}}$ can be computed via an adjoint state method as [28], [61], [62]

$$\nabla_c \mathcal{F}^{\mathrm{CC}} = \frac{1}{c^3(\mathbf{r})} \sum_{m=0}^{M-1} \int_0^T dt\, q_m(\mathbf{r}, T-t) \frac{\partial^2}{\partial^2 t} p_m(\mathbf{r},t), \quad (33)$$

where $q_m(\mathbf{r},t) \in \mathbb{L}^2(\mathbb{R}^3 \times [0,\infty))$ is the solution to the adjoint wave equation. The adjoint wave equation is defined as

$$\nabla^2 q_m(\mathbf{r},t) - \frac{1}{c^2(\mathbf{r})} \frac{\partial^2}{\partial^2 t} q_m(\mathbf{r},t) = -\tau_m(\mathbf{r},t), \qquad (34)$$

where $\tau_m(\mathbf{r},t) = g_m(\mathbf{r}, T-t) - \underline{g_m}(\mathbf{r}, T-t)$. The adjoint wave equation is nearly identical in form to the wave equation in (1) except for the different source term on the right-hand side, suggesting the same numerical approach can be employed to solve both equations. Because one needs to solve (1) and (34) M times to calculate $\nabla_c \mathcal{F}^{\mathrm{CC}}$, it is generally true that the sequential waveform inversion is computationally demanding even for a 2-D geometry [63].

APPENDIX C
BENT-RAY MODEL-BASED SOUND SPEED RECONSTRUCTION

We developed an iterative image reconstruction algorithm based on a bent-ray imaging model. The bent-ray imaging model assumes that an acoustic pulse travels along a ray path that connects the emitter and the receiver and accounts for the refraction of rays, also known as ray-bending, through an acoustically inhomogeneous medium. For each pair of receiver and emitter, the travel time, as well as the ray path, is determined by the medium's sound speed distribution. Given the travel times for a collection of emitter and receiver pairs distributed around the object, the medium sound speed distribution can be iteratively reconstructed. This bent-ray model-based sound speed reconstruction (BRSR) method has been employed in the USCT literature [26], [64], [65].

To perform the BRSR, we extracted a TOF data vector from the measured pressure data. Denoting the TOF data vector by $\underline{\mathbf{T}} \in \mathbb{R}^{\mathrm{MN^{rec}}}$, each element of $\underline{\mathbf{T}}$ represented the TOF from each emitter and receiver pair. The extraction of the TOF was conducted in two steps. First, we estimated the difference between the TOF when the object

was present and the TOF when the object was absent by use of a thresholding method [25], [66]. In particular, 20% of the peak value of each time trace was employed as the thresholding value. Second, a TOF offset was added to the estimated difference TOF for each emitter and receiver pair to obtain the absolute TOF, where the TOF offset was calculated according to the scanning geometry and the known background SOS.

Having the TOF vector $\underline{\mathbf{T}}$, we reconstructed the sound speed by solving the following optimization problem:

$$\mathbf{s} = \arg\min_{\mathbf{s}} \left\| \underline{\mathbf{T}} - \mathbf{K}^{\mathrm{s}}\mathbf{s} \right\|^2 + \beta \mathcal{R}(\mathbf{s}), \qquad (35)$$

where $\mathbf{s}$ denotes the slowness (the reciprocal of the SOS) vector, and $\mathbf{K}^{\mathrm{s}}$ denotes the system matrix that maps the slowness distribution to the TOF data. The superscript s indicates the dependence of $\mathbf{K}^{\mathrm{s}}$ on the slowness map. At each iteration, using the current estimate of the SOS, a ray-tracing method [50] was employed to construct the system matrix $\mathbf{K}^{\mathrm{s}}$. Explicitly storing the system matrix in a sparse representation, we utilized the limited BFGS method [51] to solve the optimization problem given in (35). The estimated slowness was then converted to the sound speed by taking the reciprocal of the $\hat{\mathbf{s}}$ element. We refer the readers to [26], [64]–[67] for more details about the BRSR method.

REFERENCES

[1] G. Glover, "Characterization of in vivo breast tissue by ultrasonic time-of-flight computed tomography," in *National Bureau of Standards Int. Symp. Ultrasonic Tissue Characterization, National Science Foundation, Ultrasonic Tissue Characterization II*, 1979, pp. 221–225.

[2] P. Carson, C. Meyer, A. Scherzinger, and T. Oughton, "Breast imaging in coronal planes with simultaneous pulse echo and transmission ultrasound," *Science*, vol. 214, no. 4525, pp. 1141–1143, 1981.

[3] J. S. Schreiman, J. J. Gisvold, J. F. Greenleaf, and R. C. Bahn, "Ultrasound transmission computed tomography of the breast," *Radiology*, vol. 150, no. 2, pp. 523–530, 1984.

[4] M. P. André, H. S. Janée, P. J. Martin, G. P. Otto, B. A. Spivey, and D. A. Palmer, "High-speed data acquisition in a diffraction tomography system employing large-scale toroidal arrays," *Int. J. Imaging Syst. Technol.*, vol. 8, no. 1, pp. 137–147, 1997.

[5] D. T. Borup, S. A. Johnson, F. Natterer, S. C. Olsen, J. W. Wiskin, F. Wubeling, and Y. Zhang, "Apparatus and method for imaging with wavefields using inverse scattering techniques," Dec. 21, 1999, U.S. Patent 6 005 916.

[6] N. Duric, P. Littrup, L. Poulo, A. Babkin, R. Pevzner, E. Holsapple, O. Rama, and C. Glide, "Detection of breast cancer with ultrasound tomography: First results with the computed ultrasound risk evaluation (CURE) prototype," *Med. Phys.*, vol. 34, no. 2, pp. 773–785, 2007.

[7] N. V. Ruiter, G. Göbel, L. Berger, M. Zapf, and H. Gemmeke, "Realization of an optimized 3D USCT," in *Proc. SPIE Medical Imaging International Society for Optics and Photonics*, 2011, vol. 7968, art. no. 796805.

[8] N. Duric, O. Roy, C. Li, S. Schmidt, X. Cheng, J. Goll, D. Kunz, K. Bates, R. Janer, and P. Littrup, "Ultrasound tomography systems for medical imaging," in *Emerging Imaging Technologies in Medicine*. Boca Raton, FL, USA: CRC Press, 2012, pp. 167–182.

[9] N. V. Ruiter, M. Zapf, T. Hopp, R. Dapp, E. Kretzek, M. Birk, B. Kohout, and H. Gemmeke, "3D ultrasound computer tomography of the breast: A new era?" *Eur. J. Radiol.*, vol. 81, suppl. 1, pp. S133–S134, 2012.

[10] N. Duric, P. Littrup, O. Roy, S. Schmidt, C. Li, L. Bey-Knight, and X. Chen, "Breast imaging with ultrasound tomography: Initial results with SoftVue," in *IEEE Int. Ultrasonics Symp.*, Jul. 2013, pp. 382–385.

[11] C. Li, N. Duric, P. Littrup, and L. Huang, "In vivo breast sound-speed imaging with ultrasound tomography," *Ultrasound Med. Biol.*, vol. 35, no. 10, pp. 1615–1628, 2009.

[12] J. Wiskin, D. T. Borup, S. A. Johnson, and M. Berggren, "Non-linear inverse scattering: High resolution quantitative breast tissue tomography," *J. Acoust. Soc. Am.*, vol. 131, no. 5, pp. 3802–3813, 2012.

[13] S. Manohar, R. G. H. Willemink, F. van der Heijden, C. H. Slump, and T. G. van Leeuwen, "Concomitant speed-of-sound tomography in photoacoustic imaging," *Appl. Phys. Lett.*, vol. 91, no. 13, art. no. 131911, 2007.

[14] J. Zalev, D. Herzog, B. Clingman, T. Miller, K. Kist, N. C. Dornbluth, B. M. McCorvey, P. Otto, S. Ermilov, V. Nadvoretsky, A. Conjusteau, R. Su, D. Tsyboulski, and A. Oraevsky, "Clinical feasibility study of combined optoacoustic and ultrasonic imaging modality providing coregistered functional and anatomical maps of breast tumors," in *SPIE BiOS Int. Society for Optics and Photonics*, 2012, art no. 82 230A.

[15] J. Xia, C. Huang, K. Maslov, M. A. Anastasio, and L. V. Wang, "Enhancement of photoacoustic tomography by ultrasonic computed tomography based on optical excitation of elements of a full-ring transducer array," *Opt. Lett.*, vol. 38, no. 16, pp. 3140–3143, 2013.

[16] A. C. Kak and M. Slaney, *Principles of Computerized Tomographic Imaging*. Piscataway, NJ, USA: IEEE Press, 1988.

[17] R. J. Lavarello and M. L. Oelze, "Density imaging using inverse scattering," *J. Acoust. Soc. Am.*, vol. 125, no. 2, pp. 793–802, 2009.

[18] R. J. Lavarello and M. L. Oelze, "Density imaging using a multiple-frequency DBIM approach," *IEEE T. Ultrason. Ferr.*, vol. 57, no. 11, pp. 2471–2479, 2010.

[19] A. J. Hesford and W. C. Chew, "Fast inverse scattering solutions using the distorted born iterative method and the multilevel fast multipole algorithm," *J. Acoust. Soc. Am.*, vol. 128, no. 2, pp. 679–690. 2010.

[20] P. Huthwaite and F. Simonetti, "High-resolution imaging without iteration: A fast and robust method for breast ultrasound tomography," *J. Acoust. Soc. Am.*, vol. 130, no. 3, pp. 1721–1734, 2011.

[21] F. Simonetti, "Multiple scattering: The key to unravel the subwavelength world from the far-field pattern of a scattered wave," *Phys. Rev. E*, vol. 73, art. no. 036619, Mar. 2006.

[22] Z. Zhang, L. Huang, and Y. Lin, "Efficient implementation of ultrasound waveform tomography using source encoding," in *SPIE Medical Imaging. International Society for Optics and Photonics*, 2012, art. no. 832 003.

[23] R. G. Pratt, L. Huang, N. Duric, and P. Littrup, "Sound-speed and attenuation imaging of breast tissue using waveform tomography of transmission ultrasound data," in *Proc. SPIE*, vol. 6510, 2007. 10.1117/12.708789.

[24] P. Huthwaite, F. Simonetti, and N. Duric, "Combining time of flight and diffraction tomography for high resolution breast imaging: Initial in vivo results (L)," *J. Acoust. Soc. Am.*, vol. 132, no. 3, pp. 1249–1252, 2012.

[25] C. Li, L. Huang, N. Duric, H. Zhang, and C. Rowe, "An improved automatic time-of-flight picker for medical ultrasound tomography," *Ultrasonics*, vol. 49, no. 1, pp. 61–72, 2009.

[26] A. Hormati, I. Jovanović, O. Roy, and M. Vetterli, "Robust ultrasound travel-time tomography using the bent ray model," in *Proc. SPIE*, vol. 7629, 2010, art. no. 76290I.

[27] R. Bates, V. Smith, and R. Murch, "Manageable multidimensional inverse scattering theory," *Phys. Rep.*, vol. 201, no. 4, pp. 185–277, 1991.

[28] O. Roy, I. Jovanović, A. Hormati, R. Parhizkar, and M. Vetterli, "Sound speed estimation using wave-based ultrasound tomography: Theory and GPU implementation," in *SPIE Medical Imaging. Int. Society for Optics and Photonics*, 2010, art. no. 76 290J.

[29] J. R. Krebs, J. E. Anderson, D. Hinkley, R. Neelamani, S. Lee, A. Baumstein, and M.-D. Lacasse, "Fast full-wavefield seismic inversion using encoded sources," *Geophysics*, vol. 74, no. 6, pp. WCC177–WCC188, 2009.

[30] E. Haber, M. Chung, and F. Herrmann, "An effective method for parameter estimation with PDE constraints with multiple right-hand sides," *SIAM J. Optimiz.*, vol. 22, no. 3, pp. 739–757, 2012.

[31] P. P. Moghaddam, H. Keers, F. J. Herrmann, and W. A. Mulder, "A new optimization approach for source-encoding full-waveform inversion," *Geophysics*, vol. 78, no. 3, pp. R125–R132, 2013.

[32] J. Wiskin, D. Borup, S. Johnson, M. Andre, J. Greenleaf, Y. Parisky, and J. Klock, "Three-dimensional nonlinear inverse scattering: Quantitative transmission algorithms, refraction corrected reflection, scanner design and clinical results," in *Proc. Meetings on Acoustics*, vol. 19, no. 1, art. no. 075001, 2013.

[33] E. Haber and M. Chung, "Simultaneous source for non-uniform data variance and missing data," [Online]. Available: http://arxiv.org/abs/1404.5254, 2014.

[34] K. W. Morton and D. F. Mayers, *Numerical Solution of Partial Differential Equations: An Introduction*. New York, NY, USA: Cambridge University Press, 2005.

[35] T. D. Mast, L. Souriau, D.-L. Liu, M. Tabei, A. Nachman, and R. Waag, "A k-space method for large-scale models of wave propagation in tissue," *IEEE Trans. Ultrason. Ferroelectr. Freq. Control*, vol. 48, no. 2, pp. 341–354, Mar. 2001.

[36] M. Tabei, T. D. Mast, and R. C. Waag, "A k-space method for coupled first-order acoustic propagation equations," *J. Acoust. Soc. Am.*, vol. 111, no. 1, pp. 53–63, 2002.

[37] H. Barrett and K. Myers, *Foundations of Image Science* (*Series in Pure and Applied Optics*). Hoboken, NJ, USA: Wiley, 2004.

[38] L. E. Kinsler, A. R. Frey, A. B. Coppens, and J. V. Sanders, *Fundamentals of Acoustics*, 4th ed. Hoboken, NJ, USA: Wiley, Dec. 2000.

[39] S. Nash and A. Sofer, *Linear and Nonlinear Programming*. New York, NY, USA: McGraw-Hill, 1996.

[40] M. C. Hesse, L. Salehi, and G. Schmitz, "Nonlinear simultaneous reconstruction of inhomogeneous compressibility and mass density distributions in unidirectional pulse-echo ultrasound imaging," *Phys. Med. Biol.*, vol. 58, no. 17, art. no. 6163, 2013.

[41] L. A. Romero, D. C. Ghiglia, C. C. Ober, and S. A. Morton, "Phase encoding of shot records in prestack migration," *Geophysics*, vol. 65, no. 2, pp. 426–436, 2000.

[42] F. Roosta-Khorasani, K. van den Doel, and U. M. Ascher, "Data completion and stochastic algorithms for PDE inversion problems with many measurements," [Online]. Available: http:arxiv.org/abs/1312.0707, 2013.

[43] N. Duric, P. Littrup, S. Schmidt, C. Li, O. Roy, L. Bey-Knight, R. Janer, D. Kunz, X. Chen, J. Goll, A. Wallen, F. Zafar, V. Allada, E. West, I. Jovanovic, K. Li, and W. Greenway, "Breast imaging with the SoftVue imaging system: First results," in *Proc. SPIE*, vol. 8675, 2013.

[44] T. L. Szabo, *Diagnostic Ultrasound Imaging: Inside Out*. Waltham, MA, USA: Academic Press, 2004.

[45] C. Glide, N. Duric, and P. Littrup, "Novel approach to evaluating breast density utilizing ultrasound tomography," *Medical Physics*, vol. 34, no. 2, pp. 744–753, 2007.

[46] C. Li, N. Duric, and L. Huang, "Clinical breast imaging using sound-speed reconstructions of ultrasound tomography data," in *Proc. SPIE*, vol. 6920, 2008, art. no. 692009.

[47] B. E. Treeby, E. Z. Zhang, and B. T. Cox, "Photoacoustic tomography in absorbing acoustic media using time reversal," *Inverse Problems*, vol. 26, no. 11, art. no. 115003, 2010.

[48] D. Colton and R. Kress, *Inverse Acoustic and Electromagnetic Scattering Theory*, vol. 93. New York, NY, USA: Springer, 2012.

[49] S. A. Ermilov, R. Su, A. Conjusteau, V. Ivanov, V. Nadvoretskiy, T. Oruganti, P. Talole, F. Anis, M. A. Anastasio, and A. A. Oraevsky, "3D laser optoacoustic ultrasonic imaging system for research in mice (LOUIS-3DM)," in *Proc. SPIE*, vol. 8943, 2014, 10.1117/12.2044817.

[50] J. A Sethian, "A fast marching level set method for monotonically advancing fronts," *Proc. Natl. Acad. Sci.*, vol. 93, no. 4, pp. 1591–1595, 1996.

[51] R. H. Byrd, P. Lu, J. Nocedal, and C. Zhu, "A limited memory algorithm for bound constrained optimization," *SIAM J. Sci. Comput.*, vol. 16, no. 5, pp. 1190–1208, 1995.

[52] E. Y. Sidky and X. Pan, "Image reconstruction in circular cone-beam computed tomography by constrained, total-variation minimization," *Phys. Med. Biol.*, vol. 53, no. 17, art. no. 4777, 2008.

[53] K. Wang, E. Y. Sidky, M. A. Anastasio, A. A. Oraevsky, and X. Pan, "Limited data image reconstruction in optoacoustic tomography by constrained total variation minimization," A. A. Oraevsky and L. V. Wang, Eds., *SPIE*, vol. 7899, no. 1, 2011, art. no. 78993U.

[54] K. Wang, R. Su, A. A. Oraevsky, and M. A. Anastasio, "Investigation of iterative image reconstruction in three-dimensional op-

toacoustic tomography," *Phys. Med. Biol.*, vol. 57, no. 17, art. no. 5399, 2012.

[55] C. Huang, K. Wang, L. Nie, L. Wang, and M. Anastasio, "Full-wave iterative image reconstruction in photoacoustic tomography with acoustically inhomogeneous media," *IEEE Trans. Med. Imaging*, vol. 32, no. 6, pp. 1097–1110, June 2013.

[56] C. Li, G. S. Sandhu, O. Roy, N. Duric, V. Allada, and S. Schmidt, "Toward a practical ultrasound waveform tomography algorithm for improving breast imaging," in *Proc. SPIE*, vol. 9040, art. no. 90401P, 2014.

[57] N. Duric, P. Littrup, C. Li, O. Roy, S. Schmidt, X. Cheng, J. Seamans, A. Wallen, and L. Bey-Knight, "Breast imaging with SoftVue: Initial clinical evaluation," vol. 9040, art. no. 90 400V, 2014.

[58] K. Wang, R. Schoonover, R. Su, A. Oraevsky, and M. A. Anastasio, "Discrete imaging models for three-dimensional optoacoustic tomography using radially symmetric expansion functions," *IEEE Trans. Med. Imaging*, vol. 33, no. 5, pp. 1180–1193, May 2014.

[59] K. Wang, S. A. Ermilov, R. Su, H.-P. Brecht, A. A. Oraevsky, and M. A. Anastasio, "An imaging model incorporating ultrasonic transducer properties for three-dimensional optoacoustic tomography," *IEEE Trans. Med. Imaging*, vol. 30, no. 2, pp. 203–214, Feb. 2011.

[60] J. A. Fessler, "Penalized weighted least-squares reconstruction for positron emission tomography," *IEEE Trans. Med. Imaging*, vol. 13, no. 2, pp. 290–300, 1994.

[61] S. J. Norton, "Iterative inverse scattering algorithms: Methods of computing Fréchet derivatives," *J. Acoust. Soc. Am.*, vol. 106, no. 5, pp. 2653–2660, 1999.

[62] R.-E. Plessix, "A review of the adjoint-state method for computing the gradient of a functional with geophysical applications," *Geophys. J. Int.*, vol. 167, no. 2, pp. 495–503, 2006.

[63] J. Virieux and S. Operto, "An overview of full-waveform inversion in exploration geophysics," *Geophysics*, vol. 74, no. 6, pp. WCC1–WCC26, 2009.

[64] C. Li, N. Duric, and L. Huang, "Breast ultrasound tomography with total-variation regularization," in *Proc. SPIE*, vol. 7265, art. no. 726 506, 2009.

[65] J. Jose, R. G. H. Willemink, W. Steenbergen, C. H. Slump, T. G. van Leeuwen, and S. Manohar, "Speed-of-sound compensated photoacoustic tomography for accurate imaging," *Med. Phys.*, vol. 39, no. 12, pp. 7262–7271, 2012.

[66] F. Anis, Y. Lou, A. Conjusteau, R. Su, T. Oruganti, S. A. Ermilov, A. A. Oraevsky, and M. A. Anastasio, "Investigation of the adjoint-state method for ultrasound computed tomography: A numerical and experimental study," in *Proc. SPIE*, vol. 8943, art no. 894337, 2014.

[67] M. Born and E. Wolf, *Principles of Optics: Electromagnetic Theory of Propagation, Interference and Diffraction of Light*. New York, NY, USA: Cambridge University Press, 1999.

Authors' photographs and biographies were unavailable at time of publication.

Investigation of the adjoint-state method for ultrasound computed tomography: A numerical and experimental study

Fatima Anis[a], Yang Lou[a], André Conjusteau[b],Richard Su[b], Tanmayi Oruganti[b], Sergey A. Ermilov[b], Alexander A. Oraevsky[b] and Mark A. Anastasio[a]

[a] Department of Biomedical Engineering, Washington University in St. Louis, St. Louis, MO 63130 [b] TomoWave Laboratories, Inc., Houston TX

ABSTRACT

In this work, we investigate a novel reconstruction method for laser-induced ultrasound computed tomography (USCT) breast imaging that circumvents limitations of existing methods that rely on ray-tracing. There is currently great interest in developing hybrid imaging systems that combine optoacoustic tomography (OAT) and USCT. There are two primary motivations for this: (1) the speed-of-sound (SOS) distribution reconstructed by USCT can provide complementary diagnostic information; and (2) the reconstructed SOS distribution can be incorporated in the OAT reconstruction algorithm to improve OAT image quality. However, image reconstruction in USCT remains challenging. The majority of existing approaches for USCT breast imaging involve ray-tracing to establish the imaging operator. This process is cumbersome and can lead to inaccuracies in the reconstructed SOS images in the presence of multiple ray-paths and/or shadow zones. To circumvent these problems, we implemented a partial differential equation-based Eulerian approach to USCT that was proposed in the mathematics literature but never investigated for medical imaging applications. This method operates by directly inverting the Eikonal equation without ray-tracing. A numerical implementation of this method was developed and compared to existing reconstruction methods for USCT breast imaging. We demonstrated the ability of the new method to reconstruct SOS maps from TOF data obtained by a hybrid OAT/USCT imager built by our team.

Keywords: ultrasound tomography, optoacoustic tomography, photoacoustic tomography, breast cancer imaging

1. INTRODUCTION

Transmission ultrasound computed tomography (USCT) is an emerging imaging modality with many biomedical applications. USCT can be employed to retrieve anatomical information of tissues e. g. speed of sound, acoustical impedance and reflectivity. The effectiveness of USCT in tumor detection has been discussed in recent studies.[1–3] It is known that cancerous tissues have higher SOS values compared to the benign fatty masses and healthy breast tissues. A clinical ultrasound ring array scanner for breast cancer diagnosis (Computed Ultrasound Risk Evaluation (CURE)) has been proposed.[1,2] This system consists of 256 transducer elements distributed on a ring with a 20 cm diameter. Another prototype has also been developed by SoftVue and consists of 2048 transducers.[4] The system is capable of reconstructing a series of 2D slices of the SOS, acoustic attenuation, and reflectivity distributions. Techniscan (Salt Lake City UT) introduced a commercial USCT system that employs three transducer probes placed around the breast. The transducer system is mechanically rotated to reconstruct 2D slices and subsequently vertically scanned to capture multiple slices to obtain 3D images.[5] Finally, an ultrasound imaging module capable of generating three-dimensional SOS distributions has been investigated by researchers at the Karlsruhe Institute of Technology (KIT), Germany.[6]

Biomedical applications of USCT commonly employ geometrical acoustics models and require time-of-flight (TOF) measurements. TOF data that have been recorded for many source-receiver pairs can be employed for reconstruction of the SOS distribution. The reconstruction of the speed of sound distribution is conventionally performed by using ray-tracing (RT) methods.[1,2,7,8] To account for the curvature of the ray paths, the rays are

(Send correspondence to F. Anis)
Fatima Anis: E-mail: fatimaanis@seas.wustl.edu, Telephone: 1 314 935 9403

traced along the negative gradient of the TOF distribution.[8] Ray-tracing can become cumbersome, especially for three-dimensional USCT. Moreover, unlike X-ray computed tomography, the heterogeneous SOS distribution results in uneven ray-distributions, which makes the inverse problem ill-conditioned. In this work, we will investigate a different approach for SOS image reconstruction. This method, the adjoint state (AS) method, has previously been employed for seismic tomography.[9, 10] We are investigating the AS method for USCT for the first time for biomedical applications.

2. DESCRIPTION OF NUMERICAL STUDIES

To perform USCT using RT, we have employed the the geometrical ray theory for sound waves. This approximation results in a non-linear model, the eikonal equation, to relate the measured TOF values to the speed of sound distribution as

$$|\nabla T(\mathbf{r})| = \frac{1}{c(\mathbf{r})}. \tag{1}$$

In Eq. (1), ∇T is the gradient of the TOF, T, and c is the SOS distribution, both of which are a function of position as denoted by the position vector $\mathbf{r} \in \mathbb{R}^2$. Currently, the bent-ray reconstruction is a widely employed reconstruction technique for USCT because it incorporates refraction during sound wave propagation. The eikonal equation is solved numerically by finite difference methods[11] to obtain a TOF map for a given source corresponding to a certain speed of sound map $c(\mathbf{r})$.

2.1 Ray-tracing reconstruction method

In RT methods, the TOF is calculated as the line-integral over the slowness distribution over the ray-path connecting the source and the receiver location:

$$T(\mathbf{r}) = \int_{\Gamma(c)} \frac{1}{c(\mathbf{r})}. \tag{2}$$

The dependence of the ray-path, $\Gamma(c)$, on the SOS distribution makes it a non-linear problem. The discretized imaging model is given by

$$\mathbf{T} = \mathbf{H}(\mathbf{c})\frac{1}{\mathbf{c}}, \tag{3}$$

where $\mathbf{T}$ is a vector of TOF measurments, $\mathbf{c}$ is a finite-dimensional representation of the SOS, and $\mathbf{H}(\mathbf{c})$ is the system matrix. To formulate $\mathbf{H}(\mathbf{c})$, we implemented a RT method. Weights were assigned to pixels in the discrete SOS map based on the number of times each pixel was intersected by the rays. This weight matrix constitutes $\mathbf{H}(\mathbf{c})$.

To estimate the SOS distribution from the measured TOF data, we solved the following optimization problem:

$$\hat{\mathbf{c}} = \arg \min_{\mathbf{c}} \| \mathbf{T} - \mathbf{T}^* \|^2 + \nu g(\mathbf{c}), \tag{4}$$

where $\hat{\mathbf{c}}$ denotes the sought-after estimate of the the SOS distribution, $\mathbf{T}^*$ is the measured TOF data from all source-transducer pairs, $g(\mathbf{c})$ is a penalty function, ν is a regularization parameter, and $\mathbf{T}$ is the computed TOF found by solving (1). To minimize Eq. (4) we used the Limited BFGS method.[12] In solving the nonlinear optimization problem, we evaluated the gradient of Eq. (4) as

$$\nabla \mathbf{c} = 2\mathbf{H}(\mathbf{c})^T \left[\mathbf{H}(\mathbf{c})\mathbf{c} - \mathbf{T}^* \right] + \nu \nabla g(\mathbf{c}). \tag{5}$$

It should be noted from the above equation that the first term is a linear approximation of the true non-linear gradient of the objective function. The above linearized gradient is primarily used in USCT for biomedical applications.

2.2 Adjoint-state-based reconstruction method

We implemented a previously proposed algorithm for USCT reconstructed based on the adjoint-state method.[9] The mismatch energy functional between the measured and simulated data is defined as[9]

$$E[c(\mathbf{r})] = \frac{1}{2} \int_S |T(\mathbf{r}) - T^*(\mathbf{r})|^2 d\Omega, \tag{6}$$

where $T^*|_S$ is the measured TOF and $T|_S$ is computed by solving Eq. (1). The quantity in Eq. (6) — the energy functional — measures the L^2-difference between the the solution of the eikonal equation, T, and the experimental measurement, T^*, on the measurement surface S. Using the adjoint-state method for a small perturbation $\epsilon \tilde{c}$ to c, the gradient of the energy is defined:

$$\delta E = \epsilon \int_V \frac{\tilde{c}(\mathbf{r})\lambda(\mathbf{r})}{c^3(\mathbf{r})} d\Omega \tag{7}$$

Here, V is volume enclosed the measurement surface S and $\lambda(\mathbf{r})$ is the adjoint function to $T(\mathbf{r})$ that satisfies the following adjoint equation:

$$\nabla \cdot [\lambda(\mathbf{r})\nabla T(\mathbf{r})] = 0 \tag{8}$$

with the boundary condition,

$$[\mathbf{n} \cdot \nabla T(\mathbf{r})]\lambda(\mathbf{r})|_S = [T^*(\mathbf{r}) - T(\mathbf{r})]_S. \tag{9}$$

Here $\mathbf{n}$ is the unit outward normal of the surface S. To minimize the energy using the method of gradient descent, a perturbation $\tilde{c}(\mathbf{r}) = -\lambda(\mathbf{r})/c^3(\mathbf{r})$ is defined. This leads to

$$\delta E = -\epsilon \int_V \tilde{c}^2(\mathbf{r}) d\Omega \leq 0, \tag{10}$$

where V denotes the region interior to S. By solving Eqs. (8) and (9), the update, $\tilde{c}(\mathbf{r})$, to the SOS distribution can be computed. Specifically, the SOS distribution is updated at each step as:

$$c^{k+1} = c^k + \epsilon^k \tilde{c}^k \tag{11}$$

until a convergence criterion is reached. The following two conditions are required of the SOS distribution: (i) $\tilde{c}^k|_S = 0$ and (ii) c^{k+1} is smooth. To fulfill (ii), a regularization term similar to the one used in Eq. (4) was included. The filtering scheme defined in Lueng's work[9] was also implemeted. The step size, ϵ^k, can be determined by using the Armijo-Golstein rule or by simply setting $\epsilon^k = \epsilon$. The update scheme described in Eq. (11) takes a large number of iterations to converge. Therefore, we used the limited-memory Broydon-Fletcher Goldfarb-Shanno (L-BFGS) method to solve for this nonlinear optimization problem. We solved the adjoint-state equation (8) using the fast-sweeping method[9] with the boundary conditions defined in Eq. (9).

2.3 Experimental Setup

The experimental setup consists of a single laser ultrasound (LU) source and a 64 transducer elements arranged in an arc. The array aperture spans a 152 degree arc with a radius of 65 mm. The imaging module is mounted and centered on a rotational stage operated by a stepper motor, which is used to obtain TOF measurement for 150 views. The distance between the central element of the arc array and the LU source is 130 mm. Optoacoustic imaging was concurrently performed. More detail about the LU sources and the transducer array can be found elsewhere.[13, 14]
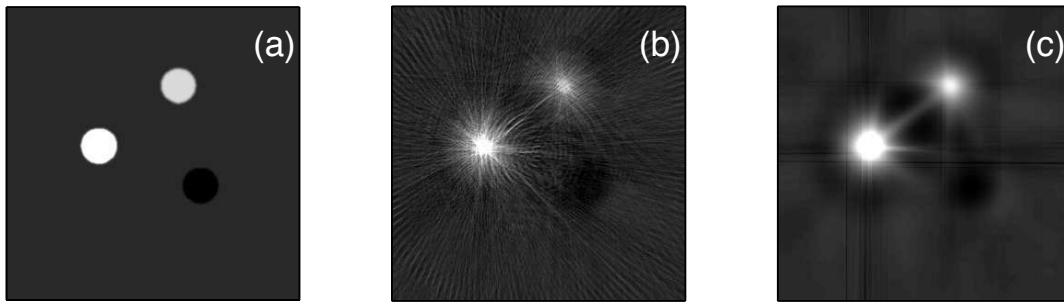
Figure 1. (a) Speed of sound distribution for the phantom; reconstructed SOS distribution for the RT method (b) and for the AS method (c).

3. RESULTS AND DISCUSSION

Computer-simulation studies were conducted to compare the RT method with the AS method. In this study, the objective function did not include a penalty and least squares estimates of the SOS distributions were computed. The two-dimensional phantom depicting the SOS distribution is shown in Figure 1(a). The phantom consists of three discs of 4.72 mm diameter with constant SOS of 1.48, 1.6 and 1.7 mm/μs, respectively. The pressure data were generated using the k-Wave software package[15] with a geometry and acoustic properties consistent with our experimental system design. Gaussian white noise was added to the calculated pressure signal to obtain experimentally-relevant SNRs. Figures 1(b) and 1(c) show the reconstructed SOS distribution for the RT method and the AS method, respectively. In the case of the RT method, streak artifacts are very visible as compared to the AS method. All three structures can be seen in the AS reconstruction of the SOS distribution. The results show that the AS method can be successfully used to perform USCT for biomedical applications.

To check the accuracy of the reconstructed SOS distribution, we selected 2 mm x 2mm regions at different locations and calculated the avaeraged SOS and standard deviation in those region. The location of the five regions is shown in Fig.2(a). The bar plot in Fig.2(b) shows the averaged SOS values for both the RT and AS method. It can be seen that AS gives accurate SOS values for the selected regions. The maximum standard deviation was 0.0226 mm/μs for region "A".

Finally, we studied the use of the AS method to perform SOS image reconstruction for the experimentally measured TOF from our LU system. The experimental phantom consists of three tubes each with a 4.72 mm internal diameter. Tubes were filled with water at different salt concentrations to induce different SOS values and $CuSO_4$ was added to provide optical contrast. For this case, concurrent optoacoustic (OA) and ultrasonic data acquisition was performed. The OA reconstruction of the phantom is shown in Fig. 3(a) and the SOS reconstruction is shown in Fig. 3(b). The SOS image was found via the AS reconstruction method. Once again, all three discs are visible in the reconstructed SOS distribution.
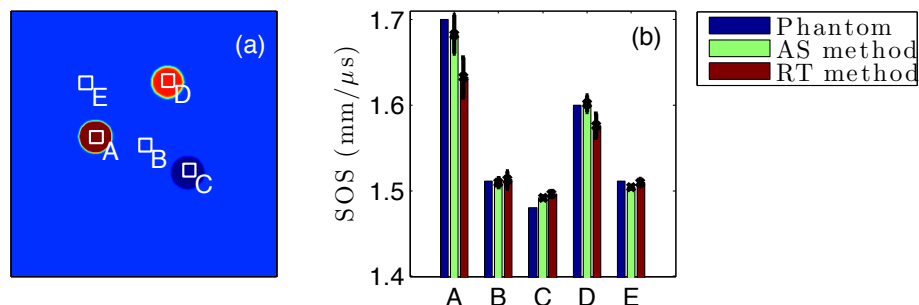

Figure 2. (a) Speed of sound distribution for the phantom with the marked location of five regions; (b) bar plot for the averaged SOS values in five regions for phantom, AS method, and RT method.
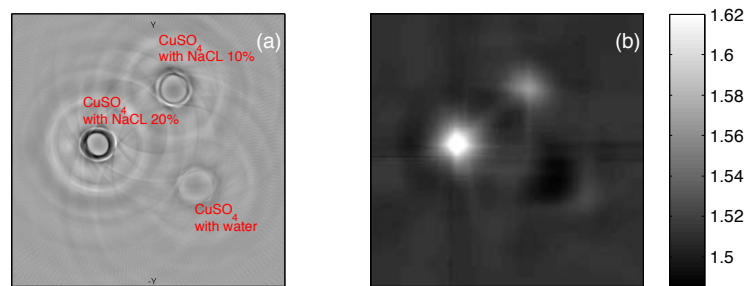
Figure 3. (a) Optoacoustic image of three tubes; (b) reconstructed SOS distribution using the AS method.

4. SUMMARY

The adjoint state method has been implemented for biomedical applications of USCT. Images reconstructed from both simulation studies and measured TOF data were presented. Ray tracing becomes much more cumbersome for three-dimensional USCT. Consequently, the adjoint state method holds great promise for that application. Further numerical studies will also be performed to quantify resolution and noise propagation in the adjoint state method.

ACKNOWLEDGMENTS

REFERENCES

1. N. Duric, P. Littrup, L. Poulo, A. Babkin, R. Pevzner, E. Holsapple, O. Rama, and C. Glide, "Detection of breast cancer with ultrasound tomography: First results with the computed ultrasound risk evaluation (cure) prototype," *Med. Phys.* **34**(2), pp. 773–785, 2007.

2. C. Li, N. Duric, P. Littrup, and L. Huang, "In vivo breast sound-speed imaging with ultrasound tomography," *Ultrasound Med. Biol.* **35**(10), pp. 1615 – 1628, 2009.

3. A. Leproux, M. van Beek, U. de Vries, M. Wasser, L. Bakker, O. Cuisenaire, M. van der Mark, and R. Entrekin, "Automated 3d whole-breast ultrasound imaging: results of a clinical pilot study," *Proc. SPIE* **7629**, pp. 762902–762902–10, 2010.

4. N. Duric, P. Littrup, S. Schmidt, C. Li, O. Roy, L. Bey-Knight, R. Janer, D. Kunz, X. Chen, J. Goll, A. Wallen, F. Zafar, V. Allada, E. West, I. Jovanovic, K. Li, and W. Greenway, "Breast imaging with the softvue imaging system: first results," *Proc. SPIE* **8675**, pp. 86750K–86750K–8, 2013.

5. J. Wiskin, D. Borup, S. Johnson, M. Berggren, D. Robinson, J. Smith, J. Chen, Y. Parisky, and J. Klock, "Inverse scattering and refraction corrected reflection for breast cancer imaging," **7629**, pp. 76290K–76290K–12, 2010.

6. R. Jiřík, I. Peterlik, N. Ruiter, J. Fousek, R. Dapp, M. Zapf, and J. Jan, "Sound-speed image reconstruction in sparse-aperture 3-d ultrasound transmission tomography," *Ultrasonics, Ferroelectrics and Frequency Control, IEEE Transactions on* **59**(2), pp. 254 –264, 2012.

7. J. Jose, R. G. H. Willemink, W. Steenbergen, C. H. Slump, T. G. van Leeuwen, and S. Manohar, "Speed-of-sound compensated photoacoustic tomography for accurate imaging," *Med. Phys.* **39**(12), pp. 7262–7271, 2012.

8. A. Hormati, I. Jovanović, O. Roy, and M. Vetterli, "Robust ultrasound travel-time tomography using the bent ray model," *Proc. SPIE* **7629**, pp. 76290I–76290I–12, 2010.

9. S. Leung and J. Qian, "An adjoint-state method for three-dimensional transmission traveltime tomography using rst arrivals," *Comm. in Math and Sci.* **4**(1), p. 2006, 249-266.

10. C. Taillandier, M. Noble, H. Chauris, and H. Calandra, "First-arrival traveltime tomography based on the adjoint-state method," *Geophysics* **74**(6), pp. WCB57–WCB66, 2009.

11. P. Podvin and I. Lecomote, "Finite difference computation of travel-times in very contrasted velocity model: A massively parallel approach and its associated tools," *Geophysical J. Int.* **105**, pp. 271–284, 1991.

12. R. H. Byrd, P. Lu, J. Nocedal, and C. Zhu, "A limited memory algorithm for bound constrained optimization," *SIAM J. Sci. Comput.* **36**, pp. 667–695, 199.

13. A. Conjusteau, V. V. Nadvoretskiy, S. A. Ermilov, and A. A. Oraevsky, "Generation of wide-directivity broadband ultrasound by short laser pulses," *Proc. SPIE* **8581**, pp. 85814U–85814U–8, 2013.

14. S. A. Ermilov, A. Conjusteau, T. Hernandez, R. Su, V. Nadvoretskiy, D. Tsyboulski, F. Anis, M. A. Anastasio, and A. A. Oraevsky, "3d laser optoacoustic ultrasonic imaging system for preclinical research," *Proc. SPIE* **8581**, pp. 85810N–85810N–5, 2013.

15. B. E. Treeby, J. Jaros, A. P. Rendell, and B. T. Cox, "Modeling nonlinear ultrasound propagation in heterogeneous media with power law absorption using a k-space pseudospectral method," *J. Acous. Soc. Am.* **131**(6), pp. 4324–4336, 2012.

Investigation of a method for laser-induced ultrasound tomography that eliminates the need for ray-tracing

Fatima Anis, Yang Lou, Andre Conjusteau, Sergey Ermilov,
Alexander Oraevsky and Mark A. Anastasio*
Dept. of Biomedical Engineering, Washington University in St. Louis, 1 Brookings Dr.,
St. Louis, MO, USA 63130

*Corresponding author. Email: anastasio@seas.wustl.edu

ABSTRACT

In this work, we investigate a novel reconstruction method for laser-induced ultrasound tomography (UST) breast imaging that circumvents limitations of existing methods that rely on ray-tracing. There is currently great interest in developing hybrid imaging systems that combine optoacoustic tomography (OAT) and UST. There are two primary motivations for this: (1) the speed-of-sound (SOS) distribution reconstructed by UST can provide complementary diagnostic information; and (2) the reconstructed SOS distribution can be incorporated in the OAT reconstruction algorithm to improve OAT image quality. However, image reconstruction in UST remains challenging. The majority of existing approaches for UST breast imaging involve ray-tracing to establish the imaging operator. This process is cumbersome and can lead to severe inaccuracies in the reconstructed SOS images in the presence of multiple ray-paths and/or shadow zones.

To circumvent these problems, we implemented a partial differential equation-based Eulerian approach to UST that was proposed in the mathematics literature but never investigated for medical imaging applications. This method operates by directly inverting the Eikonal equation without ray-tracing. A numerical implementation of this method was developed and systematically compared to existing reconstruction methods for UST breast imaging. We demonstrated the ability of the new method to reconstruct accurate SOS maps from TOF data obtained by a 3D hybrid OAT/UST imager built by our team.

Breast Ultrasound computed tomography using waveform inversion with source encoding

Kun Wang [a], Thomas Matthews [a], Fatima Anis, [a] Cuiping Li[b], Neb Duric[b,c], and Mark A. Anastasio[a]

[a] Department of Biomedical Engineering, Washington University in St. Louis, St. Louis, MO 63130
[b] Delphinus Medical Technologies, Plymouth MI 48170
[c] Karmanos Cancer Inistitute, Wayne State University, Detroit MI 48201

ABSTRACT

Ultrasound computed tomography (USCT) holds great promise for improving the detection and management of breast cancer. Because they are based on the acoustic wave equation, waveform inversion-based reconstruction methods can produce images that possess improved spatial resolution properties over those produced by ray-based methods. However, waveform inversion methods are computationally demanding and have not been applied widely in USCT breast imaging. A computationally efficient numerical wave equation solver has been reported based on a modified Fresnel propagation, which only applies to USCT systems with a planar incident wave. For breast imaging systems with a spherical incident wave, waveform inversion-based reconstruction methods remain computationally challenging.

In this work, source encoding concepts are employed to develop an accelerated USCT reconstruction method that circumvents the large computational burden of conventional waveform inversion methods. This method, referred to as the waveform inversion with source encoding (WISE) method, encodes the measurement data using a random encoding vector and determines an estimate of the speed-of-sound distribution by solving a stochastic optimization problem by use of a stochastic gradient descent algorithm. For practical applications, a data-filling strategy is proposed to mitigate source inferences to its neighbor receivers. Computer-simulation and experimental phantom studies are conducted to demonstrate the use of the WISE method. Using a single graphics processing unit card, each iteration can be completed within 25 seconds for a $128 \times 128 \, \text{mm}^2$ reconstruction region. The results suggest that the WISE method maintains the high spatial resolution of waveform inversion methods while significantly reducing the computational burden.

1. PURPOSE

This study is focused on the image reconstruction of breast speed-of-sound (SOS) distribution in USCT. The majority of USCT image reconstruction methods for breast imaging investigated to date have been based on approximations to the acoustic wave equation.[1,2] A relatively popular class of methods is based on geometrical acoustics. They are commonly referred to as 'ray-based' methods. Although ray-based methods can be computationally efficient, the spatial resoultion of the images they produce is limited due to the fact that diffraction effects are not modelled.[3,4] This is undesirable for breast imaging applications, in which the ability to resolve fine features, e.g., tumor spiculations, is important for distinguishing healthy from diseased tissues.

USCT reconstruction methods based on the acoustic wave equation, also known as full-wave inverse scattering or waveform inversion methods, have also been explored for a variety of applications including medical imaging.[4–7] Because they account for higher-order diffraction effects, waveform inversion methods can produce images that possess higher spatial resolution properties than those produced by ray-based methods.[4,5] However, conventional waveform inversion methods are iterative in nature and require the wave equation to be solved numerically a large number of times at each iteration. Consequently, such methods can be extremely computationally burdensome. For special geometries,[7] efficient numerical wave equation solvers have been reported. However, apart from

special cases, the large computational burden of waveform inversion methods has hindered their widespread application.

The purpose of this study is to develop an algorithmically accelerated waveform inversion method for breast SOS reconstruction. Aided by a graphics processing unit (GPU)-accelerated implementation, the developed method will maintain the high spatial resolution of standard waveform inversion methods with a signifcant reduction in computational time.

2. METHODS

A conventional waveform inversion method seeks the solution of

$$\hat{\mathbf{c}} = \arg\min_{\mathbf{c}} \frac{1}{2} \sum_{m=0}^{M-1} \|\underline{\mathbf{g}}_m - \mathbf{H}^{\mathrm{c}}\mathbf{s}_m\|^2 + \beta\mathcal{R}(\mathbf{c}), \tag{1}$$

where $\mathbf{c}$ is the sought-after object to be reconstructed, i.e, SOS distribution, $\underline{\mathbf{g}}_m$ denotes the measured data vector, $\mathbf{s}_m$ denotes the (known) source vector, $\mathbf{H}^{\mathrm{c}}$ denotes a numerical wave equation solver (NWES) that maps the known source vector to the measured data vector, and $\mathcal{R}(\mathbf{c})$ and β denote the penalty term and the regularization parameter respectively. The superscript in $\mathbf{H}^{\mathrm{c}}$ indicates the dependence of $\mathbf{H}^{\mathrm{c}}$ on $\mathbf{c}$. Note that one USCT measurement involves firing a sequence of acoustic pulses in turn and recording the data corresponding to every pulse. Each pulse-firing and data recording process will be indexed by m for $m = 0, 1, \cdots, M-1$. Solving Eqn. (1), in general, requires the calculation of $\frac{1}{2}\sum_{m=0}^{M-1}\nabla_{\mathrm{c}}\|\underline{\mathbf{g}}_m - \mathbf{H}^{\mathrm{c}}\mathbf{s}_m\|^2$, where ∇_{c} denotes the gradient operator with respect to $\mathbf{c}$. The gradient in each summand is commonly computed by use of an adjoint state method,[5] which requires two runs of the NWES. Repeating the gradient calculation for all sources results in $2M$ runs of the NWES at each iteration. This computational burden largely hinders the application of the conventional waveform inversion methods in practice.

In this study, a waveform inversion with source encoding (WISE) method was developed. The WISE method employs the objective function

$$\hat{\mathbf{c}} = \arg\min_{\mathbf{c}} \mathbf{E}_{\mathbf{w}}\left\{\frac{1}{2}\|\underline{\mathbf{g}}^{\mathrm{w}} - \mathbf{H}^{\mathrm{c}}\mathbf{s}^{\mathrm{w}}\|^2\right\} + \beta\mathcal{R}(\mathbf{c}), \tag{2}$$

where $\mathbf{E}_{\mathbf{w}}$ denotes the expectation operator with respect to the random source encoding vector $\mathbf{w} \in \mathbb{R}^M$, and $\underline{\mathbf{g}}^{\mathrm{w}}$ and $\mathbf{s}^{\mathrm{w}}$ denote the $\mathbf{w}$-encoded data and source vectors, defined as

$$\underline{\mathbf{g}}^{\mathrm{w}} = \sum_{m=0}^{M-1}[\mathbf{w}]_m\underline{\mathbf{g}}_m, \quad \text{and} \quad \mathbf{s}^{\mathrm{w}} = \sum_{\mathrm{m}=0}^{\mathrm{M}-1}[\mathbf{w}]_{\mathrm{m}}\mathbf{s}_{\mathrm{m}}, \tag{3}$$

respectively. Equation (2) was solved by use of a stochastic gradient descent algorithm.[8] Because the stochastic gradient descent algorithm calculated the gradient of only one realization of the random variable $\frac{1}{2}\|\underline{\mathbf{g}}^{\mathrm{w}} - \mathbf{MH}^{\mathrm{c}}\mathbf{s}^{\mathrm{w}}\|^2$ at each iteration, the required number of NWES runs per iteration was reduced from $2M$ to 2. Although it, in general, requires more algorithm iterations to average out the randomness in the realizations, the WISE method, as demonstrated later, can greatly reduce the overall number of NWES runs. Both computer-simulation and experimental phantom studies were conducted to demonstrate the use of the WISE method for breast SOS reconstruction.

3. RESULTS

The images reconstructed from the computer-simulated noise-free data by use of the WISE method after 199 iterations and sequential waveform inversion method after 43 iterations are shown in Fig. 1-(a) and (b). As expected,[4, 9] both images are more accurate and possess higher spatial resolution than the one reconstructed by use of the bent-ray reconstruction algorithm displayed in Fig. 1-(c). The images shown in Fig. 1-(a) and -(b) possess similar accuracies as measured by their Euclidean distances from the SOS phantom vector $\mathbf{c}$, namely 0.07% of $\|\mathbf{c}\|$ for the former and 0.08% of $\|\mathbf{c}\|$ for the latter. However, the reconstruction of Fig. 1-(a) required

only about 1.7% of the computational time required to reconstruct Fig. 1-(b), namely, 1.4 hours for the former and 81.4 hours for the latter respectively. This is because the WISE method required only 1018 NWES runs, which is signficantly less than the 58880 NWES runs required by the sequential waveform inversion method. With a similar number of NWES runs, (e.g., 1024), one can only complete a single algorithm iteration by use of the sequential waveform inversion method. The corresponding image, shown in Fig. 1-(d), lacks quantitative accuracy as well as qualitative value for identifying features. The results suggest that the WISE method maintains the advantages of the sequential waveform inversion method while significantly reducing the computational time.
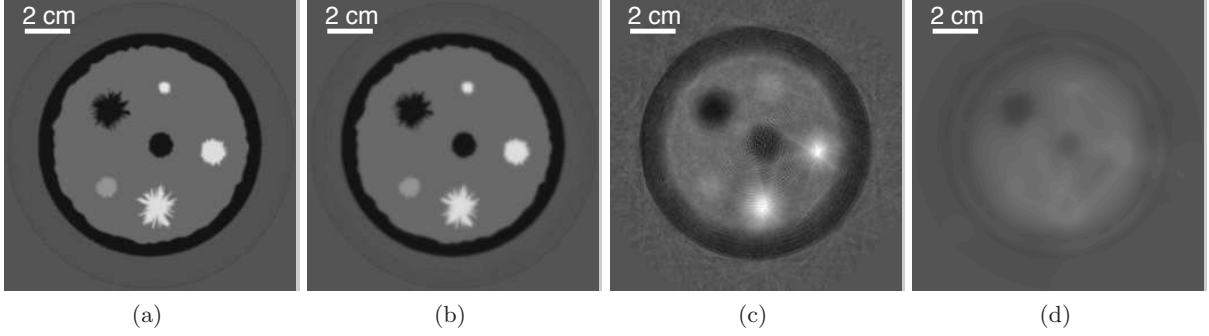

(a)   (b)   (c)   (d)

Figure 1. Images reconstructed by use of (a) the WISE method after the 199-th iteration ($1,018$ runs of NWES) (b) the sequential waveform inversion algorithm after the 43-rd iteration ($58,880$ runs of the NWES), (c) the bent-ray model-based SOS reconstruction method, and (d) the sequential waveform inversion algorithm after the 1-st iteration ($1,024$ runs of the NWES) from the noise-free non-attenuated data. The grayscale window is $[1.46, 1.58]$ mm/μs.

The images reconstructed from the experimentally-measured data are shown in Fig. 2. The spatial resolution of the image reconstructed by use of the WISE method is significantly higher than that reconstructed by use of the bent-ray model-based method. In particular, the structures labeled 'A' and 'B' possess clearly-defined boundaries. In addition, the structure labeled 'Cancer' in Fig. 2-(a) is almost indistinguishable in the image reconstructed by use of the bent-ray model-based method (see Fig. 2-(b)). The improved spatial resolution is expected because the WISE method takes into account the high-order diffraction effects, which are ignored by the bent-ray method.[4]

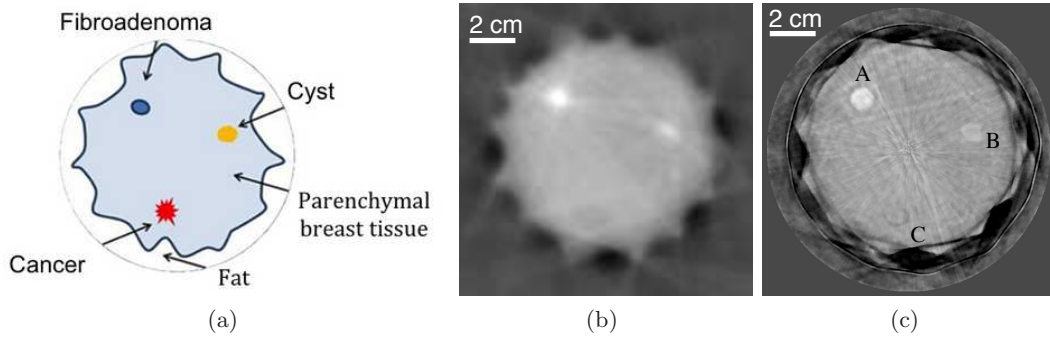(a)   (b)   (c)

Figure 2. (a) Schematic of the breast phantom employed in the experimental study. Images reconstructed from the experimentally measured phantom data by use of (a) the bent-ray model-based SOS reconstruction method and (b) the WISE method after the 200-th iteration. The grayscale window is $[1.49, 1.57]$ mm/μs.

4. NEW OR BREAKTHROUGH WORK TO BE PRESENTED

Source encoding concepts are demonstrated in breast USCT experimental studies for the first time. Unlike previously studied waveform inversion methods that were based on the Helmholtz equation, the WISE method

is formulated by use of the time-domain acoustic wave equation. A GPU-accelerated NWES is developed that can compute 1800 time samples, on a 1024×1024 spatial grid, in 5 seconds. In addition, a data-filling strategy is proposed to mitigate the inference of the source with its neighboring receivers for practical applications.

5. CONCLUSION

It is known that waveform inversion-based reconstruction methods can produce SOS images that possess improved spatial resolution properties over those produced by ray-based methods. However, waveform inversion methods are computationally demanding and have not been applied widely in USCT breast imaging. In this work, based on the time-domain wave equation and motivated by recent mathematical results in the geophysics literature, the WISE method was developed that circumvents the large computational burden of conventional waveform inversion methods. This method encodes the measurement data using a random encoding vector and determines an estimate of the speed-of-sound distribution by solving a stochastic optimization problem by use of a stochastic gradient descent algorithm. With our current GPU-based implementation, the computation time was reduced from weeks to hours. The WISE method was systematically investigated in computer-simulation and experimental studies involving a breast phantom. The results suggest that the method holds value for USCT breast imaging applications in a practical setting.

6. DISCLOSURE

This work is original. Parts of this work have been submitted to *IEEE Transactions on Ultrasounics, Ferroelectrics and Frequency Control* and are under review.

REFERENCES

1. Kak, A. C. and Slaney, M., [*Principles of Computerized Tomographic Imaging*], IEEE Press (1988).
2. Huthwaite, P., Simonetti, F., and Duric, N., "Combining time of flight and diffraction tomography for high resolution breast imaging: Initial invivo results (l)," *The Journal of the Acoustical Society of America* **132**(3), 1249–1252 (2012).
3. Bates, R., Smith, V., and Murch, R., "Manageable multidimensional inverse scattering theory," *Phys. Rep.* **201**(4), 185 – 277 (1991).
4. Pratt, R. G., Huang, L., Duric, N., and Littrup, P., "Sound-speed and attenuation imaging of breast tissue using waveform tomography of transmission ultrasound data," in [*Proc. SPIE*], **6510**, 65104S–65104S–12 (2007).
5. Roy, O., Jovanović, I., Hormati, A., Parhizkar, R., and Vetterli, M., "Sound speed estimation using wave-based ultrasound tomography: theory and GPU implementation," in [*SPIE Medical Imaging*], 76290J–76290J, International Society for Optics and Photonics (2010).
6. Zhang, Z., Huang, L., and Lin, Y., "Efficient implementation of ultrasound waveform tomography using source encoding," in [*SPIE Medical Imaging*], 832003–832003, International Society for Optics and Photonics (2012).
7. Wiskin, J., Borup, D. T., Johnson, S. A., and Berggren, M., "Non-linear inverse scattering: High resolution quantitative breast tissue tomography," *The Journal of the Acoustical Society of America* **131**(5), 3802–3813 (2012).
8. Bousquet, O. and Bottou, L., "The tradeoffs of large scale learning," in [*Advances in Neural Information Processing Systems 20*], Platt, J., Koller, D., Singer, Y., and Roweis, S., eds., 161–168, Curran Associates, Inc. (2008).
9. Li, C., Sandhu, G. S., Roy, O., Duric, N., Allada, V., and Schmidt, S., "Toward a practical ultrasound waveform tomography algorithm for improving breast imaging," in [*Proc. SPIE*], **9040**, 90401P–90401P–10 (2014).

Accelerated iterative image reconstruction in three-dimensional optoacoustic tomography

Fatima Anis[a], Kun Wang[a], Richard Su[b], Sergey A. Ermilov[b],
Alexander A. Oraevsky[b] and Mark A. Anastasio[a]

[a] Department of Biomedical Engineering, Washington University in St. Louis,
St. Louis, MO 63130 [b] TomoWave Laboratories, Inc., Houston TX

ABSTRACT

Iterative image reconstruction algorithms can model complicated imaging physics, compensate for imperfect data acquisition systems, and exploit prior information regarding the object. Hence, they produce higher quality images than do analytical image reconstruction algorithms. However, three-dimensional (3D) iterative image reconstruction is computationally burdensome, which greatly hinders its use with applications requiring a large field-of-view (FOV), such as breast imaging. In this study, an improved GPU-based implementation of a numerical imaging model and its adjoint have been developed for use with general gradient-based iterative image reconstruction algorithms. Both computer simulations and experimental studies are conducted to investigate the efficiency and accuracy of the proposed implementation for optoacoustic tomography (OAT). The results suggest that the proposed implementation is more than five times faster than the previous implementation.

Keywords: Optoacoustic tomography, iterative image reconstruction, GPU acceleration

1. INTRODUCTION

Optoacoustic tomography (OAT) is an emerging imaging modality with many biomedical applications.[1–3] The clinical applications of OAT, e.g., breast imaging, have been pursued by several research groups.[4–6] OAT imaging is performed by illuminating tissues with a laser pulse. The thermoacoustic effect then creates an acoustic pressure rise that can be measured by transducer elements placed around the object.[1,7] From these measured pressure data, we can reconstruct an estimate of the absorbed optical energy density of the object. Many analytical and iterative image reconstruction algorithms have been developed for this purpose.[8] Analytical methods, such as filtered backprojection (FBP),[8–10] have the advantages of being simplistic and computationally efficient; however, due to model errors, measurement noise, data inconsistencies, and limited data,[11] these methods often produce lower quality images than those obtained by iterative methods. Iterative algorithms have also been used to incorporate a more accurate imaging physics as well as the spatial and acousto-electric impulse responses of ultrasonic transducers.[11–13]

Despite the many advantages of iterative methods, few studies have been reported involving 3D iterative image reconstruction algorithms,[12,14,15] primarily because of their computational complexity. Progress has been made in this regard by the use of graphic processing unit (GPU) accelerated algorithms; however, even in this case, it takes tens of minutes to perform a single iteration and several hours to obtain an image, making iterative algorithms less attractive for practical applications.[15] In this study, we present an accelerated interpolation-based imaging algorithm that combines four strategies: (i) the use of a new imaging model that eliminates one operator, (ii) the use of a voxel-driven adjoint imaging operator, (iii) the acceleration of convolution calculations by CUDA's parallelized fast-Fourier transform library, and (iv) a multi-GPU implementation. Image reconstruction was performed by solving a panelized least squares optimization problem using a linear conjugate gradient algorithm.[12,16]

(Send correspondence to F. Anis)
Fatima Anis: E-mail: fatimaanis@seas.wustl.edu, Telephone: 1 314 935 9403

2. DESCRIPTION OF THE IMAGING MODEL

2.1 Continuous-to-Discrete (C-D) Imaging Model

When sampling effects are considered, an OAT system for a point-like transducer is properly described by a continuous-to-discrete (C-D) imaging model:

$$\left[\mathbf{u}\right]_{qK+k} = d^e(t)*_t \,\bar{g}(\mathbf{r}^s,t)\Big|_{t=k\Delta_t}, \qquad \begin{matrix} q=0,1,\cdots,Q-1, \\ k=0,1,\cdots,K-1, \end{matrix} \tag{1}$$

where K represents the total number of temporal samples, Q is the number of transducer elements, and $[\mathbf{u}]_{qK+k}$ is the measured pressure at time t corresponding to the kth temporal sample recorded by the qth transducer element. In Eqn. (1), $d^e(t)$ is the time derivative of the acoustic-electric response (EIR) of the transducer, and it is assumed to be identical for all transducer elements. Also, $\bar{g}(\mathbf{r}^s,t)$ is related to the spherical Radon transform (SRT) by the following expression:

$$\bar{g}(\mathbf{r}^s,t) \quad = \quad \frac{\beta}{4\pi C_p}\frac{g(\mathbf{r}^s,t)}{t}, \tag{2}$$

$$= \quad \frac{\beta}{4\pi C_p}\frac{1}{t}\int_V dr A(\mathbf{r})\delta(c_0 t - |\mathbf{r}^s - \mathbf{r}|), \tag{3}$$

where $g(\mathbf{r}^s,t)$ is the SRT calculated at time t for the transducer element located at position $\mathbf{r}^s$, $A(\mathbf{r})$ is the absorbed optical energy density, and β, c_0, and C_p are the coefficient of volume expansion, the speed of sound in the medium, and the specific heat capacity of the medium at constant pressure, respectively.

2.2 Interpolation-based Discrete-to-Discrete (D-D) Imaging Model

To perform iterative image reconstruction, we discretized the object $A(\mathbf{r})$ in Eqn.(3). In this work, we have focused on the interpolation-based imaging model for discretization.[15] We have included a brief description of the imaging model for completeness (Ref. [15] provides a more detailed description). To apply iterative image reconstruction algorithms, we employed the following N-dimensional representation of the object function

$$A(\mathbf{r}) \approx \sum_{n=0}^{N-1}[\boldsymbol{\alpha}]_n\phi_n(\mathbf{r}), \tag{4}$$

where $\boldsymbol{\alpha}$ is a coefficient vector whose n-th element is denoted by $[\boldsymbol{\alpha}]_n$, and $\phi_n(\mathbf{r})$ is an expansion function. The coefficient vector elements are defined as samples of the object function on the nodes of a uniform Cartesian grid:

$$\left[\boldsymbol{\alpha}\right]_n = \int_V d\mathbf{r}\,\delta(\mathbf{r}-\mathbf{r}_n)A(\mathbf{r}), \quad n=0,1,\cdots,N-1, \tag{5}$$

where, $\mathbf{r}_n = (x_n,y_n,z_n)^T$ specifies the location of the n-th node of the uniform Cartesian grid. The definition of the expansion function depends on the choice of interpolation method.[17] For a trilinear interpolation method, the expansion function can be expressed as[18]

$$\phi_n^{\text{int}}(\mathbf{r}) = \begin{cases} (1-\frac{|x-x_n|}{\Delta_s})(1-\frac{|y-y_n|}{\Delta_s})(1-\frac{|z-z_n|}{\Delta_s}), & \text{if } |x-x_n|,|y-y_n|,|z-z_n| \leq \Delta_s \\ 0, & \text{otherwise} \end{cases}, \tag{6}$$

where Δ_s is the voxel size. On substitution from Eqn. (4) into Eqn. (1), a D-D mapping from $\boldsymbol{\alpha}$ to $\mathbf{u}$ can be expressed as

$$\mathbf{u} \approx \mathbf{H}\boldsymbol{\alpha}. \tag{7}$$

$\mathbf{H}$ can be decomposed in two steps:

$$\mathbf{u} = \mathbf{H}\boldsymbol{\alpha} \equiv \mathbf{D}^e\bar{\mathbf{G}}\boldsymbol{\alpha}, \tag{8}$$

where $\bar{\mathbf{G}}$ and $\mathbf{D}^e$ are discrete approximations of Eqn. (3) and the operator that implements a temporal convolution with the derivative of the EIR, respectively. We implemented $\bar{\mathbf{G}}$ using a 'ray-driven' implementation[19–21] of the

SRT. In this case, for each data sample, the surface integral is evaluated as the sum of the contributions from the voxels that reside on the spherical shell surface specified by the data sample. By use of Eqns. (3), (4), (5), and (6), we obtain

$$
\left[\mathbf{G}\boldsymbol{\alpha}\right]_{qK+k} = \frac{\Delta_s^2}{k\Delta_t} \sum_{n=0}^{N-1} \left[\boldsymbol{\alpha}\right]_n \sum_{i=0}^{N_i-1} \sum_{j=0}^{N_j-1} \phi_n(\mathbf{r}_{k,i,j}) \equiv \left[\bar{\mathbf{g}}\right]_{qK+k}, \tag{9}
$$

where $[\bar{\mathbf{g}}]_{qK+k} \approx \bar{g}(\mathbf{r}_q^s,t)|_{t=k\Delta_t}$ with $\mathbf{r}_q^s$ specifying the location of the q-th point-like transducer, and N_i and N_j denote the numbers of divisions over the two angular coordinates of the local spherical coordinate system with respect to the position of the transducer element (see Wang's paper[15] for more detail). The convolution operator in Eqn. (1) is calculated as

$$
\left[\mathbf{D}^e \bar{\mathbf{g}}\right]_{qK+k} = \frac{\beta}{4\pi C_p} \left[\mathcal{F}^{-1}\left\{\mathcal{F}(\mathbf{d}^e)\mathcal{F}(\bar{\mathbf{g}})\right\}\right]_{qK+k} \equiv \left[\mathbf{u}\right]_{qK+k}, \tag{10}
$$

where $\mathbf{d}^e \epsilon \mathbb{R}^k$ contains the temporal samples of the derivative of the EIR, and $\mathcal{F}(\cdot)$ and $\mathcal{F}^{-1}(\cdot)$ denote the discrete Fourier and inverse Fourier transforms, respectively.

2.3 The Voxel-Driven Adjoint Operator in the Interpolation-based Imaging Model

The adjoint operator of $\mathbf{H}$ is defined as $\mathbf{H}^\dagger = \bar{\mathbf{G}}^\dagger \mathbf{D}^{e\dagger}$, where

$$
\left[\mathbf{D}^{e\dagger} \mathbf{u}\right]_{qK+k} = \frac{\beta}{4\pi C_p} \left[\mathcal{F}^{-1}\left\{\mathcal{F}(\mathbf{d}^e)^* \mathcal{F}(\mathbf{u})\right\}\right]_{qK+k} \equiv \bar{\mathbf{g}}'_{qK+k}. \tag{11}
$$

In case of the ray-driven adjoint operator $\bar{\mathbf{G}}^\dagger$,

$$
\left[\mathbf{G}^\dagger \mathbf{g}'\right]_n = \Delta_s^2 \sum_{q=0}^{Q-1} \sum_{k=0}^{K-1} \left[\bar{\mathbf{g}}'\right]_{qK+k} \sum_{i=0}^{N_i-1} \sum_{j=0}^{N_j-1} \phi_n(\mathbf{r}_{k,i,j}) \equiv \left[\boldsymbol{\alpha}'\right]_n. \tag{12}
$$

Here, with respect to the projection operator, we introduce an unmatched adjoint operator that accumulates the contribution from all the transducers to a given voxel. This scheme is referred to as the voxel-driven adjoint operator. For the voxel-driven adjoint operator,

$$
\left[\mathbf{G}_{\text{vox}}^\dagger \mathbf{g}'\right]_n = \Delta_s^2 \sum_{q=0}^{Q-1} \left[\bar{\mathbf{g}}'\right]_{\tilde{k}} \equiv \left[\boldsymbol{\alpha}'_{\text{vox}}\right]_n. \tag{13}
$$

Here $\tilde{k} = (|\mathbf{r}_q^s - \mathbf{r}_n|/c_0)/\Delta_t$, and the value of $\left[\bar{\mathbf{g}}'\right]_{\tilde{k}}$ was approximated by linear interpolation from its two neighboring samples as

$$
\left[\bar{\mathbf{g}}'\right]_{\tilde{k}} = \frac{1}{t_{\tilde{k}}} \left[\left(k+1-\tilde{k}\right)\left[\mathbf{g}'\right]_{qK+k} + \left(\tilde{k}-k\right)\left[\mathbf{g}'\right]_{qK+k+1}\right], \tag{14}
$$

where $t_{\tilde{k}} = |\mathbf{r}_q^s - \mathbf{r}_n|/c_0$, and k is the integer part of $\tilde{k}$. Comparing Eqn. (12) with Eqn. (13), we find that $[\alpha'_{\text{vox}}]_n \approx [\alpha']_n$. Moreover, Eqn. (13) can also be derived from Eqn. (12). In this study, the accelerated interpolation-based imaging model refers to the D-D imaging model with forward operators in Eqn. (9) and (10) and the adjoint operators described in Eqn. (11) and (13).

All operators were implemented using the CUDA framework to take advantage of GPU parallelization. The calculations were performed primarily on NVIDIA K40 GPUs.

3. COMPUTER SIMULATIONS AND EXPERIMENTAL STUDIES

Computer simulation studies were performed on a 3D phantom containing nine spheres of different diameters and absorbed energy densities. A 2D slice of the phantom is shown in Fig. 1(a). The pressure data were generated for 90 tomographic views distributed uniformly between 0 and 2π for a transducer array consisting of 64 transducer elements. The elements were equiangularly distributed between 0 and π. The phantom had an overall size of $29.4 \times 29.4 \times 61.4$ mm^3, and we used a voxel size of 0.14 mm in each dimension.

Experimental studies were conducted on pre-existing mouse data from 180 tomographic views and 63 transducer elements. The transducer elements were distributed uniformly between 14° and 84°. The measured data consisted of 1536 temporal samples recorded at a 20 MHz sampling rate. In this study, we set c_0 to be 1.54 mm/μs and the Grüneisen coefficient ($\beta c_0^2/C_p$) to be 2.3716.

3.1 Image Reconstruction Algorithm

3.1.1 Penalized Least-Squares with Quadratic Penalty (PLS-Q)

The absorbed optical enery density was estimated by minimizing the penalized least-squares objective function using a linear conjugate gradient method:

$$\hat{\boldsymbol{\alpha}} = \arg\min_{\boldsymbol{\alpha}} \|\mathbf{u} - \mathbf{H}\boldsymbol{\alpha}\|^2 + \beta \mathrm{R}(\boldsymbol{\alpha}), \tag{15}$$

where β is the regularization parameter and $\mathrm{R}(\boldsymbol{\alpha})$ is defined as

$$\mathrm{R}(\boldsymbol{\alpha}) = \sum_{n=0}^{N-2} \left[(\alpha_n - \alpha_{nx})^2 + (\alpha_n - \alpha_{ny})^2 + (\alpha_n - \alpha_{nz})^2 \right]. \tag{16}$$

In the above equation, nx, ny, and nz are the neighboring grid points to the nth node along each direction.

4. RESULTS AND DISCUSSION

The images reconstructed from the numerical phantom data are shown in Fig. 1. It can be seen that the image from the new interpolation-based algorithm (c) agrees very well with that reconstructed using the original algorithm[15] (b), as well as with the phantom (a). In this study, a penalty was not employed, i.e. $\beta = 0$. The images were obtained after the 34th iteration. Using the original interpolation-based algorithm, it took 918 minutes (using one GPU) to obtain an image, while the acceleratd algorithm provided an image in 41 minutes (using four GPUs). The results suggest that the new accelerated algorithm is **20 times** more efficient than the
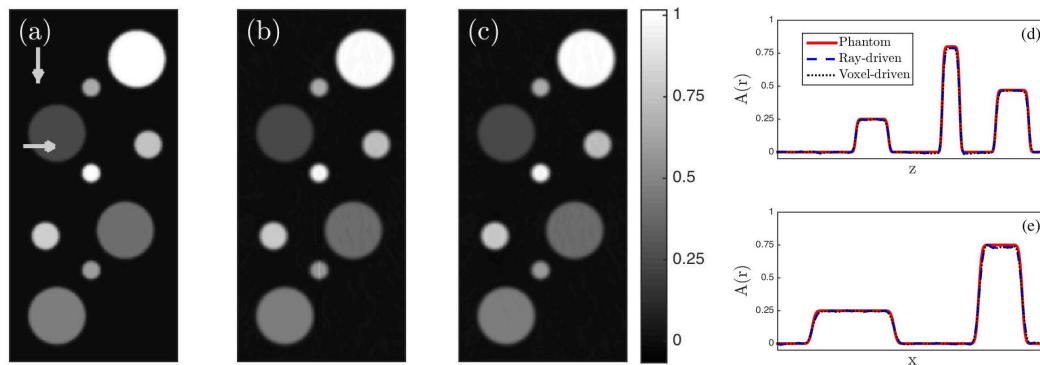

Figure 1. Slices of (a) the numerical phantom and the images reconstructed using (b) the interpolation-based algorithm with the ray-driven adjoint operator and (c) the interpolation-based algorithm with the voxel-driven adjoint operator; (d) profiles corresponding to the vertical arrow in (a) for all three images; (e) profiles corresponding to the horizontal arrow in (a) for all three images.
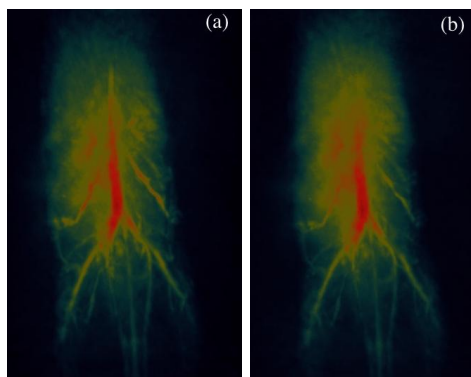
Figure 2. Maximum intensity projection renderings of 3D images of a mouse body using (a) the original interpolation-based algorithm, and (b) the accelerated interpolation-based algorithm.

original implementation when we take advantage of multiple GPUs, and more than **five times** more efficient when using a single GPU implementation.

Images reconstructed for mouse data are shown in Fig. 2. The regularization parameter was 0.1 and the images were obtained after 30 iterations. By comparing the images, we see that the accelerated algorithm retains the fine vasculature structures of the image reconstruced using matched ray-driven backprojection algorithm. It took 26 hours and 30 minutes for the image reconstruction using the original algorithm, but the image was reconstructed in just one hour and 21 minutes using the accelerated algorithm.

5. SUMMARY

In this study, we have demonstrated the use of an unmatched adjoint operator (with respect to the projection operator) for both a numerical phantom and experimental studies. The unmatched adjoint operator is five times more computationally efficient than the matched adjoint operator. Moreover, the unmatched operator can also be more conveniently parallelized in multi-GPU implementations. The study beneficially extends 3D iterative image reconstruction algorithms to applications with a large FOV, such as breast imaging.

ACKNOWLEDGMENTS

REFERENCES

1. A. A. Oraevsky and A. A. Karabutov, "Optoacoustic tomography," in *Biomedical Photonics Handbook*, T. Vo-Dinh, ed., CRC Press LLC, 2003.
2. L. V. Wang, "Tutorial on photoacoustic microscopy and computed tomography," *IEEE Journal of Selected Topics in Quantum Electronics* **14**, pp. 171–179, 2008.
3. Z. Xu, C. Li, and L. V. Wang, "Photoacoustic tomography of water in phantoms and tissue," *Journal of Biomedical Optics* **15**(3), p. 036019, 2010.
4. S. A. Ermilov, M. P. Fronheiser, H.-P. Brecht, R. Su, A. Conjusteau, K. Mehta, P. Otto, and A. A. Oraevsky, "Development of laser optoacoustic and ultrasonic imaging system for breast cancer utilizing handheld array probes," *Photons Plus Ultrasound: Imaging and Sensing 2009* **7177**(1), p. 717703, SPIE, 2009.
5. R. A. Kruger, R. B. Lam, D. R. Reinecke, S. P. D. Rio, and R. P. Doyle, "Photoacoustic angiography of the breast," *Med. Phys.* **37**(11), pp. 6096–6100, 2010.
6. G. Ku, B. D. Fornage, X. Jin, M. Xu, K. K. Hunt, and L. V. Wang, "Thermoacoustic and photoacoustic tomography of thick biological tissues toward breast imaging," *Technology in Cancer Research and Treatment* **4**, pp. 559–566, 2005.

7. L. V. Wang and H.-I. Wu, *Biomedical Optics, Principles and Imaging*, Wiley, Hoboken, N.J., 2007.

8. L. A. Kunyansky, "Explicit inversion formulae for the spherical mean Radon transform," *Inverse Problems* **23**, pp. 373–383, 2007.

9. Y. Xu and L. V. Wang, "Universal back-projection algorithm for photoacoustic computed tomography," *Physical Review E* **71**(016706), 2005.

10. Y. Xu, D. Feng, and L. V. Wang, "Exact frequency-domain reconstruction for thermoacoustic tomography: I. Planar geometry," *IEEE Transactions on Medical Imaging* **21**, pp. 823–828, 2002.

11. K. Wang, S. A. Ermilov, R. Su, H.-P. Brecht, A. A. Oraevsky, and M. A. Anastasio, "An imaging model incorporating ultrasonic transducer properties for three-dimensional optoacoustic tomography," *Medical Imaging, IEEE Transactions on* **30**, pp. 203 –214, feb. 2011.

12. K. Wang, R. Su, A. A. Oraevsky, and M. A. Anastasio, "Investigation of iterative image reconstruction in three-dimensional optoacoustic tomography," *Physics in Medicine and Biology* **57**(17), p. 5399, 2012.

13. B. T. Cox, S. R. Arridge, K. P. Köstli, and P. C. Beard, "Two-dimensional quantitative photoacoustic image reconstruction of absorption distributions in scattering media by use of a simple iterative method," *Appl. Opt.* **45**, pp. 1866–1875, Mar 2006. http://ao.osa.org/abstract.cfm?URI=ao-45-8-1866.

14. P. Ephrat, L. Keenliside, A. Seabrook, F. S. Prato, and J. J. L. Carson, "Three-dimensional photoacoustic imaging by sparse-array detection and iterative image reconstruction," *Journal of Biomedical Optics* **13**(5), p. 054052, 2008.

15. K. Wang, C. Huang, Y.-J. Kao, C.-Y. Chou, A. A. Oraevsky, and M. A. Anastasio, "Accelerating image reconstruction in three-dimensional optoacoustic tomography on graphics processing units," *Medical Physics* **40**(2), pp. –, 2013.

16. C. Huang, K. Wang, L. Nie, L. Wang, and M. Anastasio, "Full-wave iterative image reconstruction in photoacoustic tomography with acoustically inhomogeneous media," *Medical Imaging, IEEE Transactions on* **32**, pp. 1097–1110, June 2013.

17. A. Buehler, A. Rosenthal, T. Jetzfellner, A. Dima, D. Razansky, and V. Ntziachristos, "Model-based optoacoustic inversions with incomplete projection data," *Med. Phys.* **38**(3), pp. 1694–1704, 2011.

18. A. C. Kak and M. Slaney, *Principles of Computerized Tomographic Imaging*, IEEE Press, 1988.

19. M.A. Anastasio, J. Zhang, X. Pan, Y. Zou, G. Keng, and L.V. Wang, "Half-time image reconstruction in thermoacoustic tomography," *IEEE Transactions on Medical Imaging* **24**, pp. 199–210, 2005.

20. M. Anastasio, J. Zhang, E. Sidky, Y. Zou, D. Xia, and X. Pan, "Feasibility of half-data image reconstruction in 3-D reflectivity tomography with a spherical aperture," *Medical Imaging, IEEE Transactions on* **24**, pp. 1100 –1112, sept. 2005.

21. J. Zhang, M. Anastasio, P. La Riviere, and L. Wang, "Effects of different imaging models on least-squares image reconstruction accuracy in photoacoustic tomography," *Medical Imaging, IEEE Transactions on* **28**, pp. 1781 –1790, nov. 2009.

Three-Dimensional Optoacoustic and Laser-Induced Ultrasound Tomography System for Preclinical Research in Mice: Design and Phantom Validation

S. A. Ermilov[1], R. Su[1,2], A. Conjusteau[1], F. Anis[3], V. Nadvoretskiy[1], M. A. Anastasio[3], and A. A. Oraevsky[1,2]

Abstract

In this work, we introduce a novel three-dimensional imaging system for in vivo high-resolution anatomical and functional whole-body visualization of small animal models developed for preclinical and other type of biomedical research. The system (LOUIS-3DM) combines a multiwavelength optoacoustic tomography (OAT) and laser-induced ultrasound tomography (LUT) to obtain coregistered maps of tissue optical absorption and speed of sound, displayed within the skin outline of the studied animal. The most promising applications of the LOUIS-3DM include 3D angiography, cancer research, and longitudinal studies of biological distributions of optoacoustic contrast agents.

Keywords

photoacoustic tomography, speed of sound tomography, mouse imaging

Introduction

Three-dimensional full-aperture optoacoustic, also known as photoacoustic, tomography (3D-OAT) was previously shown to efficiently visualize central and peripheral vasculature and blood-rich organs of a mouse.[1-3] Reconstructed 3D-OAT images could provide information valuable for preclinical studies of pathologies that affect local blood content, such as cancer, trauma, ischemia, stroke, and so on.[4,5] For example, in cancer research development of angiogenesis, a complex microvascular network feeding a growing tumor can be assessed with 3D-OAT.[4] Other

[1]TomoWave Laboratories, Houston, TX, USA
[2]Department of Biomedical Engineering, University of Houston, Houston, TX, USA
[3]Department of Biomedical Engineering, Washington University in St. Louis, St. Louis, MO, USA

Corresponding Author:

S. A. Ermilov, TomoWave Laboratories, 6550 Mapleridge St., Suite 124, Houston, TX 77081-4629, USA.
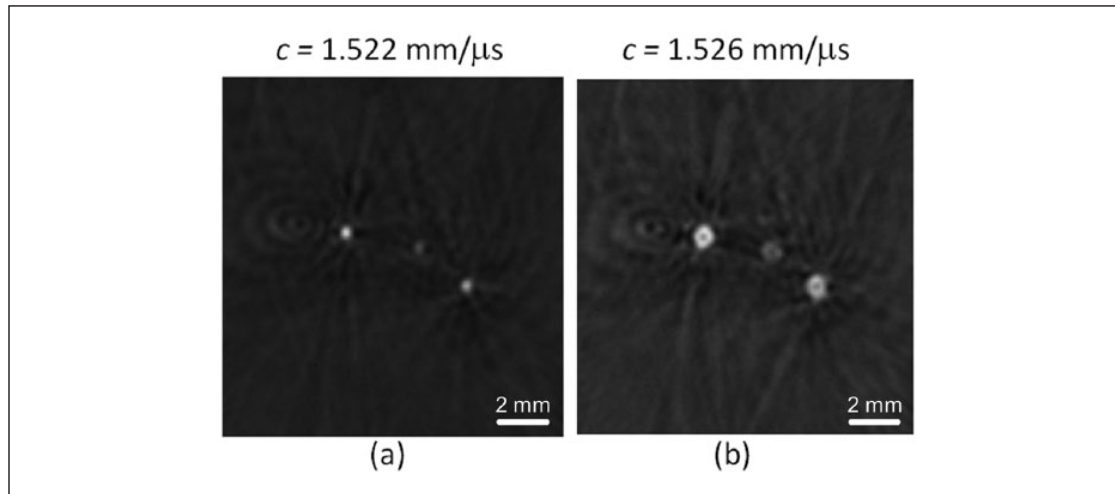Email: sae@tomowave.com

Figure 1. Section of a 3D optoacoustic image of two hairs. Data were acquired by using a 64-channel arc-probe, 25MHz sampling rate, and 150 angular acquisitions. Hairs were aligned in a cross-pattern stretched along the axis of rotation. (a) Image reconstructed with correct speed of sound of 1.522 mm/µs, corresponding to the speed of sound in the ambient distilled water at 36°C. Image shows sharp cross-sections of both hairs with diameters of 260 µm. (b) Image reconstructed from the same data with speed of sound increased by 0.3% to 1.526 mm/µs. Blurring of the hairs is noticeable, and the measured FWHM diameter of both hairs is increased by 140% to 630 µm.

preclinical applications of full-aperture optoacoustic systems include the monitoring of high-frequency ultrasound (Hi-Fu) treatment, longitudinal studies of postmortem changes, and measurements of biodistributions of optoacoustic contrast agents such as carbon nanotubes, metal plasmonic nanoparticles, and fluorescent proteins.[6-13] Clinical applications of 3D-OAT are also being investigated and may require high-quality visualization of peripheral vasculature down to the microcirculation level. One such example is the monitoring of an individual's peripheral blood flow during a physiological stress test aimed to study local vasomotor response during induced short-term hypothermia.[14] The feasibility of using 3D optoacoustic tomography (OAT) for breast angiography was also reported.[15]

Biological objects visualized with OAT typically consist of blood vessels, muscles, connective tissue, bones, air, and liquid filled spaces. Such mechanically heterogeneous composition complicates optoacoustic imaging by creating artifacts due to mismatch in acoustic impedances.[16] It also decreases image quality through blurring introduced by assumption of homogeneous speed of sound (SOS) during tomographic reconstruction.[16,17] Mitigation of OAT image artifacts due to unmodeled SOS variations is particularly important in the case of 3D-OAT. In such cases, the reconstructed objects can be located several centimeters from the acoustic transducers, and variations in the SOS introduce noticeable blurring on the reconstructed image. Figure 1 shows an example of a section across 3D image of two hairs reconstructed with two SOSs different by just 0.3%. In this situation, small blood vessels can be visually blurred and their diameters increased by 140% to 630 µm from the original 260 µm.

Ultrasound computed tomography (UCT) seeks to reconstruct distributions that describe acoustic properties of an object.[18,19] In biomedical applications, UCT has been employed to estimate the SOS and acoustic attenuation (AA) distributions, which can characterize soft tissues. Most previous investigations of UCT have utilized electrically generated ultrasound.[20-22] UCT continues to mature and is currently being evaluated for breast cancer imaging. For example, Li et al. (2009) used the CURE system with 256 ultrasound transducers evenly distributed over a 20
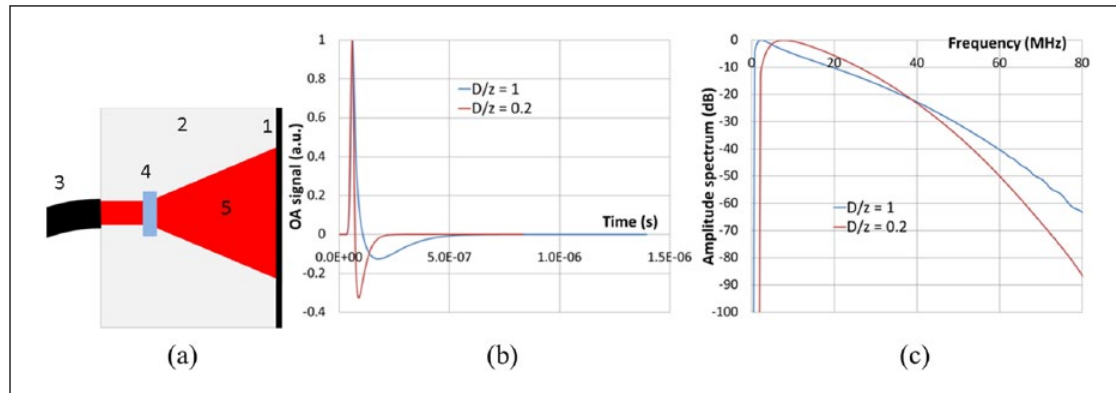
Figure 2. (a) A schematic showing a device for generation of planar monopolar laser ultrasound waves (side view). (1) optically absorbing layer (black paint), (2) acoustically matching backing, (3) optical fiber bundle, (4) lens, (5) expanding laser beam. Computer simulation of ultrawide band laser ultrasound planar waveforms generated by a 16 ns laser pulse incident upon a highly absorbing flat substrate with acoustically matching conditions: (b) temporal profiles and (c) amplitude spectra of laser-induced ultrasound signals (OA signal) measured at two different distances (z) from the laser ultrasound emitter. D is a diameter of the Gaussian laser beam at the surface of the emitter.

cm diameter ring array to reconstruct parallel coronal SOS slices in 61 breast cancer patients.[23] Their advanced tomography algorithm based on the iterative bent-ray model regularized with total-variation (TV) allowed imaging and quantification of SOS in malignant lesions (1548 ± 17 m/s), as well as differentiation between fatty tissue (1422 ± 9 m/s) and breast parenchyma (1487 ± 21 m/s). They also demonstrated that SOS images fused with back-scattered ultrasound could be used for monitoring clinical response of breast cancer to neo-adjuvant chemotherapy. Nebeker and Nelson (2012) proposed another technological approach to coronal breast UCT by positioning a breast between a regular convex ultrasound transducer and a concave ultrasound reflector, and engaging a rotational mechanism to acquire the required set of views.[24]

Laser ultrasound (LU) pulses are generated via the same optoacoustic effect that allows opto-acoustic imaging.[4,25] The main difference is that, in case of laser-induced ultrasound, absorption of optical energy occurs in an artificial emitter element, which is located outside of the interrogated tissue or object and has extremely high absorption coefficient (10^3 cm^{-1} and more) and increased efficiency of thermoacoustic conversion (Gruneisen parameter). One of the easiest ways to create an efficient laser ultrasound source is to use a Q-switched laser (same laser could be used in opto-acoustic imaging) illuminating black-colored or painted polymers, such as polyethylene, acrylic, or Teflon, which have Gruneisen parameter two to four times that of water. High-quality ultrawide band nonreverberating acoustic pulses are achieved by acoustic matching and/or removal of the emitter's interfaces.[26-28] Figure 2 shows results of a computer simulation for ultrawide band laser ultrasound waveforms generated by a 16 ns laser pulse incident upon a highly absorbing flat substrate with acoustically matching conditions. As it is seen in Figure 2(b) and (c), when properly designed, laser ultrasound sources can generate acoustic pulses, which are by far superior to those of traditional electrically generated ultrasound in terms of lack of reverberations and spectral bandwidth providing the best source for SOS and spectral AA tomographies.[27,29] In addition, using laser-induced ultrasound is the most efficient and inexpensive way to combine UCT and OAT, as both technologies employ the same optimized lasers, transducers, and electronics.

Two-dimensional laser ultrasound tomography (LUT) was originally proposed by Manohar et al. (2007).[30] By introducing a graphite rod into the optical beam of their transmission-mode 2D

photoacoustic tomography system (between the 1064 nm laser illuminator and the interrogated object), the authors were able to separate in time photoacoustic transients and laser ultrasound pulses generated by the illuminated carbon fiber. SOS images of an agar/oil phantom were reconstructed using straight-ray fan-beam CT and showed good quality of two 8 mm and 5 mm square inclusions. Subsequent publications from the same research group further advanced the technique by, first, implementing the concomitant photoacoustic tomography and LUT for both SOS and AA,[31] and, then, by significantly accelerating data acquisition via multiple (nine) simultaneously emitting LU elements.[32] The latter case, however, resulted in image degradation as compared with a unit armed with just a single LU emitter. The most recent work in the field of 2D-LUT demonstrated coregistered photoacoustic and SOS maps from the excised kidney of a mouse embedded in an agar matrix.[17] Although, high fidelity photoacoustic images showed internal structure of the kidney, SOS map was only able to segment the entire organ from the background.

In case when LUT is coregistered with optoacoustic data, the spatial distribution of acoustic properties can be employed in iterative reconstruction algorithms to improve the fidelity of optoacoustic images.[33-35] Recently, Xia et al. (2013) used experimental data obtained from a mouse kidney phantom and from a leaf phantom to compare photoacoustic reconstructions done with a single SOS value optimized for the entire interrogated volume with those utilizing the estimated map of SOS distribution.[17] The authors concluded that the former, simplified approach resulted in images of reasonable quality, providing spatial SOS variations were not too large (as in the mouse kidney phantom). When spatial SOS variations were significant (leaf phantom), photoacoustic images reconstructed with optimized single SOS demonstrated inferior quality, mostly at the periphery of the rotational reconstruction geometry.

In this work, we present novel instrumentation and a tomographic framework for performing 3D-OAT with coregistered 3D laser-induced ultrasound tomography (3D-LUT). The ultimate goal of this study is to develop a 3D laser OAT-UCT imaging system for preclinical research (LOUIS-3DM). We report the first fully 3D laser UCT unit and demonstrate the performance of the system prototype through multiwavelength optoacoustic imaging coregistered with SOS imaging of a phantom.

Materials and Method

Optoacoustic Imaging Unit

The optoacoustic imaging component of the system was based on a design proven to produce excellent volumetric images of mice in vivo.[1,8] Figure 3a depicts the imaging module that contains a metal housing (1), array of ultrasonic transducers (2), alignment unit (3), optical fiber bundles for optoacoustic imaging of the skin (4), optical fiber bundles for optoacoustic imaging of deep tissue (5), array of laser ultrasound emitters (6), and computer controlled rotational stage (7). In these studies, we used a water-tank-based prototype of LOUIS-3DM (Figure 3b). Using a rectangular water tank allowed us to optimize parts and units during development process without expensive remanufacturing of the imaging module. The prototype contained an arc-shaped array (2) (Imasonic SAS, Voray sur l'Ognon, France) of 64 (2 mm × 2 mm) piezo-composite ultrasonic transducers (1.5-4.5 MHz bandwidth at −6dB), which was used in both optoacoustic and ultrasound tomography modes. The aperture of the array was spanning a 150° arc with a radius of 65 mm, oriented vertically inside the tank. During the OAT scanning, a mouse or a phantom was rotated about the axis passing through the center of the array parallel to the plane of the arc. Since all the transducers in such a scanning geometry look straight into the center of the reconstructed volume, the negative contribution of the transducer's directivity into the quality of reconstructed images is reduced. Alignment of the axis of rotation was performed as needed
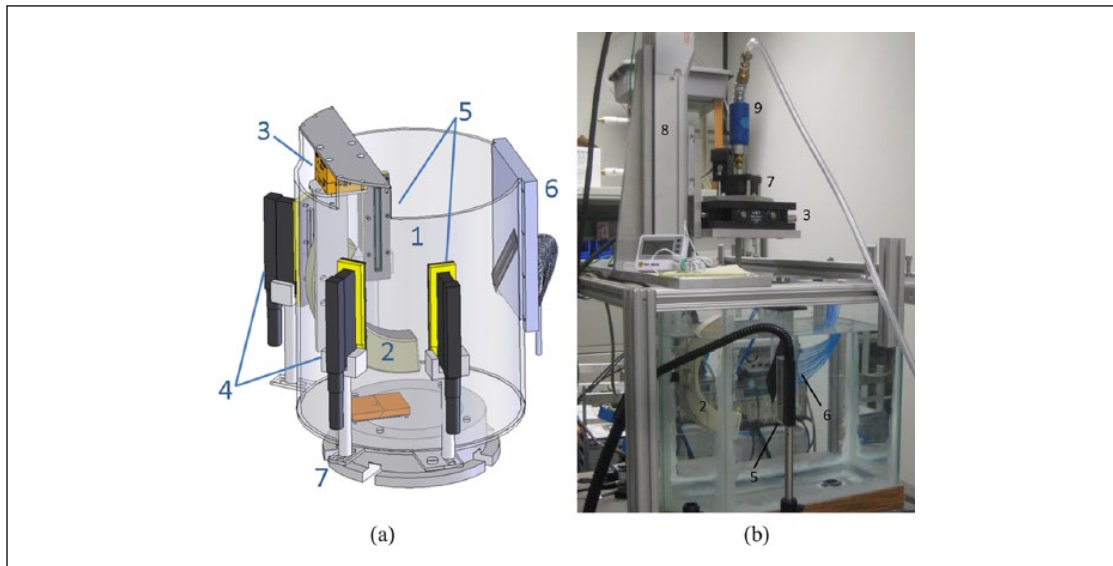
Figure 3. (a) Designer's vision of the 3D-OAT/LUT imaging module. (b) Water-tank-based prototype of the LOUIS-3DM. Metal housing (1), array of ultrasonic transducers (receivers) (2), manual alignment unit (3), optical fiber bundles for optoacoustic imaging of the skin (4), optical fiber bundles for optoacoustic deep tissue imaging (5), array of laser ultrasound emitters (6), computer controlled rotational stage (7), motorized linear stage (8), gas anesthesia delivery module (9). OAT = optoacoustic tomography; LUT = laser-induced ultrasound tomography.

using a manual 2D translation stage (3) (Thor Labs, Newton, New Jersey, USA) oriented perpendicularly to the arc of the array. The alignment was confirmed using optoacoustic imaging of a horse hair.

The OAT scan was performed by a DC motor with an optical encoder (7) (Faulhaber Gmbh, Schoenaich, Germany) for 10 full 360° rotations or cycles with 2.4° steps and 150 views per cycle. The rotational step size was set to match the angular pitch between the elements of the arc array. A motorized linear stage (8) provided up to 150 mm movement along the axis of rotation and served simply to position the interrogated sample at an appropriate depth inside the tank. The mouse/phantom holder with the gas anesthesia delivery module (9) (Summit Anesthesia Solutions, Bend, Oregon) was described in detail in our previous work.[1] Optoacoustic illumination was provided by two bifurcated, randomized fiber bundles with four rectangular output profiles of 1 mm × 80 mm each. A Q-switched laser system (SpectraWave, Tomowave Laboratories, Houston, Texas, USA) was used to establish appropriate optoacoustic illumination pattern selected from two fixed (532 nm and 1064 nm, 9 ns pulses, up to 160 mJ/pulse) and a tunable (750-830 nm, 12 ns pulses, up to 80 mJ/pulse) output wavelength, and operated at 10 Hz pulse repetition frequency. A 532 nm wavelength, being absorbed primarily within a narrow superficial layer of skin, was used in a backward optoacoustic mode (4) to outline the visualized biological object and to identify two separate acoustic domains (inside and outside of the biological object) for future improved implementation of OAT/LUT.[16,17] The wavelengths of 760 nm, 800 nm, and 1064 nm are typically used in orthogonal optoacoustic mode (5), as they are necessary for reconstruction of functional volumetric maps related to distribution of total hemoglobin, water, and local levels of blood oxygenation.[36,37] Electronic system components like 40 to 90 dB broadband analog amplifier with adjustable gain control and the digital acquisition (DAQ) hardware operated at 64 parallel channels, 25 MHz, and 1536 samples per channel were previously reported for 3D-OAT mouse imaging system.[1,8]

Signal conditioning for deep tissue imaging included (a) synchronization with the moment of laser emission using laser pulse signals recorded by a photodiode, (b) averaging data acquired at identical rotational positions during the scan, (c) Wiener deconvolution of the system's acousto-electric impulse response, and (d) bandpass filtering with 0.25 to 5 MHz bandwidth. Data collected after each complete deep tissue OAT scan were used in near full-aperture 3D filtered back-projection[38] for reconstruction of rectangular volume with 0.1 mm³ voxels and dimensions up to 30 mm × 30 mm × 50 mm centered at the focus of the probe. It was developed to run on graphics processing units (GPUs) which support compute unified device architecture (CUDA), resulting in fast reconstruction of 3D-OAT images (about 1.5 min for 50 million voxels).[39] Visualization was performed using VolView 2.0 (Kitware, Clifton Park, New York, USA) and included (a) median filtering with a 3 × 3 × 3 voxel kernel, and (b) two linear ramps for the Scalar Opacity Mapping starting near the mode of the histogram. Gradient-based opacity was manipulated manually to clean out fuzziness/noise and emphasize large intensity changes (boundaries).

Signal conditioning for skin imaging included (a) enveloping, (b) low-pass filtering, and (c) limiting data to the first and last sample of the mouse (skin) signal using noise-based thresholding. The OAT was then performed in the same manner as in the case of deep tissue imaging. Visualization of the skin also was a double ramp process. Skin volume was presented in gray palette, with a dark gray scale of 0.3 starting near the mode of the histogram. Gradient opacity was manually set in attempt to enhance the skin layer.

For combined representation of the skin over internal structures of a mouse, the volumes of skin (532 nm) and blood vessels (1064 nm) were merged together in Volview. They were visually processed in the same manner as they were individually with the only exception that the 532 nm volume was made 70% more transparent to see the 1064 nm volume within. The skin was represented in gray scale palette and essentially enveloped the 1064 nm yellow/red image providing natural anatomical fiducials for vascular network, kidneys, and spleen.

Laser-Induced Ultrasound Imaging Unit

Several designs of the array of laser ultrasound emitters were considered, and parameters were optimized through both computer simulations and prototyping, while the design of the arc array of acoustic receivers (the same that is used in the optoacoustic mode) was fixed. The reconstructed volume was constrained to be equal to 30 mm × 30 mm × 50 mm as in typical whole-body 3D-OAT of a mouse.

As our computer simulations suggested that SOS images were comparable for the spiral, oblique circular, and linear diagonal arrangements of LU emitters,[40] we decided to further pursue linear geometry that could be accurately reproduced and aligned. Section S1 in the Supplementary Materials contains details of the design and evaluation of another promising prototype based on the spiral arrangement of the LU emitters. We fabricated a rectangular acrylic support of optical fibers with fiber slots arranged in a planar diagonal pattern facing the array of receivers (Figure 4a). The output termini of thirty-three 600 μm multimode step-index fibers were permanently glued to the acrylic support. The inputs of the fibers were arranged in a linear pattern and fixed within the aluminum plate (Figure 4b). Both ends of the fiber were polished to 0.3 micron with lapping film. During LUT scans, fiber-optic inputs of the emitters were coupled to the fiber-optic output of the laser using a ball-lens projection system (Figure 4c). A cheap and disposable laser printer transparency film (thickness about 125 μm) painted with black plastic-specific spray acrylic was used to produce laser ultrasound pulses. The film was positioned 53 mm from the axis of rotation with painted side facing the array of receivers. To minimize acoustic reflections generated on a glass interface, the painted film was offset by 8 mm with respect to the fiber-optic illuminators using two rectangular acrylic spacers. Due to the short offset distance and small difference between
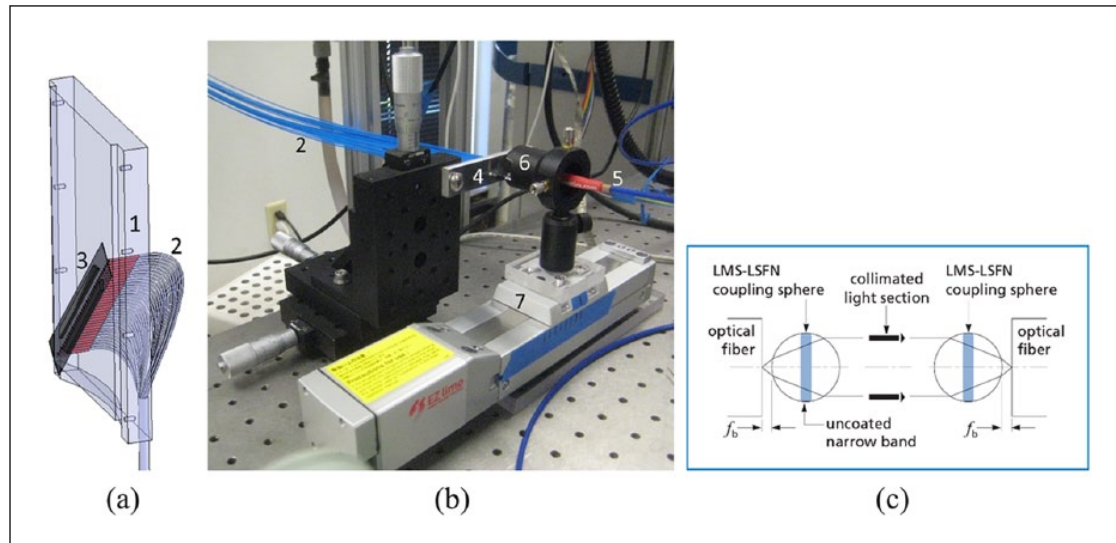
Figure 4. Laser-induced ultrasound unit. (a) Array of LU emitters. (b) Fiber-to-fiber optic coupling and scanning. (c) Ball-lens (LMS-LSFN) fiber-optic coupler. (1) Acrylic support of optical fibers, (2) thirty-three 600 μm optical fibers, (3) transparency film painted with black acrylic (LU source), (4) aluminum support of fiber-optic inputs of the emitters, (5) fiber-optic output of the laser, (6) ball-lens projection system, (7) linear motorized stage.

refractive indices of the fiber's core and water, light beam expansion was negligible. Each individual LU emitter mimicked a point source by exploiting the expansion of a very small diameter (600 μm) flat wave. We used fundamental Nd:YAG wavelength of the SpectraWave laser system attenuated to energies about 100 μJ per pulse. Laser ultrasound was generated by conversion of 9 ns laser pulses into clean nonreverberating ultrawide band acoustic pulses.

The temperature of water in the tank (background) was maintained by heating elements placed at the bottom of the tank and controlled by the proportional-integral-derivative controller (PID Temperature Controller, Watlow Inc., Columbia, Missouri, USA). The precision of ±0.1°C was achieved during both calibration and experiment facilitating accurate estimates of the SOS for the background (Figure 5). Spatial gradients of the water temperature and water contamination were minimized by a custom-made water circulation and filtration system based on FilStar XP1 (Rena, Chalfont, Pennsylvania, USA).

At every rotational position, optical fiber inputs of laser ultrasound emitters were sequentially scanned with a fiber-optic output of the laser mounted on a linear motorized stage (Figure 4b). LUT scan was performed immediately prior to the optoacoustic scans using deionized water maintained at the desired constant temperature as a coupling background acoustic medium with known speed of sound. During each LU emission, all 64 receivers acquired 1536 samples in parallel at 40 MHz sampling rate. It took approximately 1.5 hr to complete a scan using 33 emitters, 72 rotational views, and 64 averaged acquisitions/(emitter × view).

Characterization of LU Emitters

A single element prototype of the LU source was designed and assembled. To evaluate the amplitude, spectral, and directivity characteristics of laser ultrasound pulses, the source was held at the bottom of our custom-built protractor[27] such that the emitting surface was located exactly at the axis of rotation (Figure 6a). The protractor (Figure 6b) allowed accurate and reproducible rotation of the emitter with respect to the axis of detection of the calibrated hydrophone (Onda
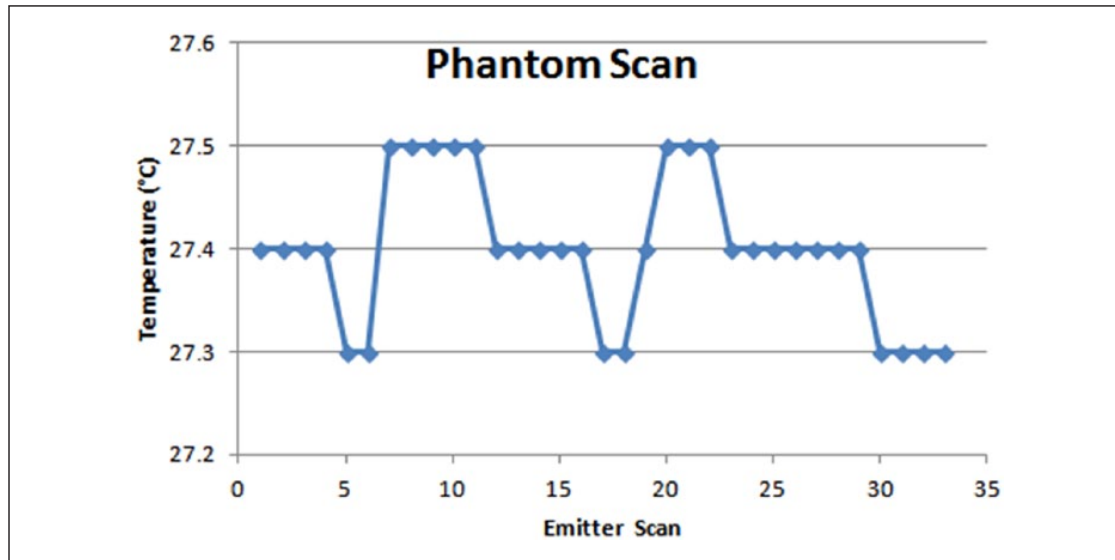
Figure 5. Temperature readings inside the water tank during LUT of the phantom. LUT = laser-induced ultrasound tomography.

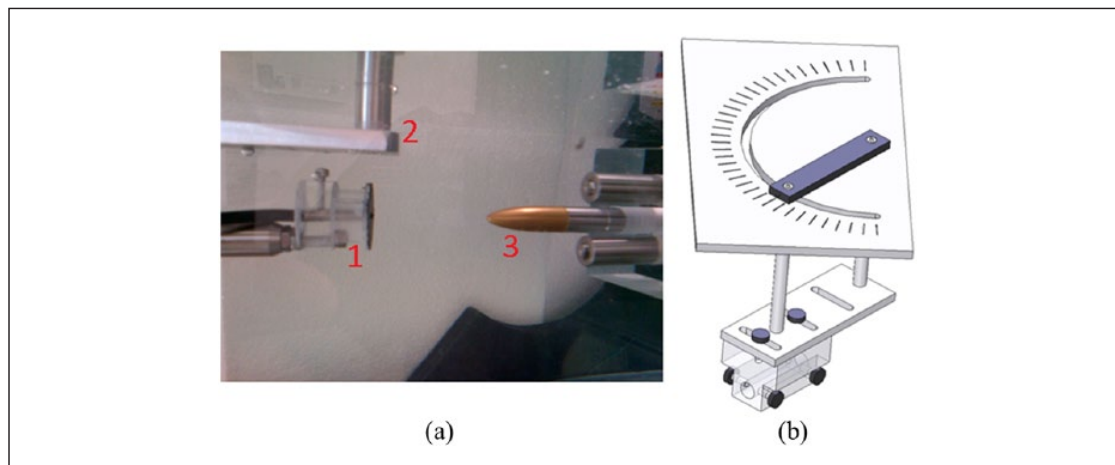(a)   (b)

Figure 6. Setup for characterization of LU emitter. (a) A prototype of a single emitter (1) is mounted on the protractor (2). The surface of the emitter is located exactly on the axis of rotation. The calibrated hydrophone (3) is used to measure a generated acoustic waveform. (b) The protractor assembly. See text for further details, as well as Ref. 27.

HGL-1000). The hydrophone had a broadband (0-30 MHz) sensitivity of 510 nV/Pa. The output of the hydrophone was fed to the oscilloscope (Tektronix TDS-3014) through the AH-2010 broadband amplifier with a gain A = 10. The impulses were acquired with gigahertz sampling rate (10,000 points per trace, thus 10 μs were acquired) and saved to a computer with LabView through GPIB interface. During acquisition, the emitter and the hydrophone were separated by about 50 mm to measure acoustic wavefront in the far field. The angle of detection varied from 90° (normal to the surface of the source) to 40°. To quantify the efficiency of the LU source, a single point measurement was also performed at the surface of the emitter.

3D Speed of Sound Tomography

The goal of SOS tomography is to reconstruct relative slowness of the object with respect to the homogeneous medium using the measured relative time of flight (TOF) for all source–receiver pairs.

Time of flight (TOF) estimation. The TOF was measured using a steep onset of a transmitted laser ultrasound pulse detected within a time window defined by the known emitter–receiver distance and valid SOS range (1.45-1.55 mm/µs, considering that in our geometry each LU ray traversed mostly through ambient water). LU signals processed with a bandpass 1 to 5 MHz second order Butterworth filter were subject to thresholding based on the estimated root mean square (RMS) noise (σ).Matlab *filter* function with a phase recovery was used to preserve the steep onset of LU signal. The first sample within the time window, which exceeded the empirically selected threshold $Th = 10\sigma$ was selected as the onset of the transmitted LU pulse. If no sample was found above the threshold, the error was recorded for that particular view and receiver–emitter pair, and it was not used in the subsequent reconstruction.

Following mechanical alignment of the LUT unit, the relative coordinates of emitters and receivers were calibrated by model-fitting the TOF values measured for background acoustic medium with well-known speed of sound. Using preliminary calibration of TOF for thermally stable background medium was supposed to make reconstruction less sensitive to system alignment and knowledge of absolute coordinates for emitters and receivers.

3D speed of sound image reconstruction. We performed image reconstruction based on the geometrical ray theory for sound waves to establish a nonlinear model that relates the measured TOF values to 3D SOS distribution. This results in the Eikonal equation:

$$\left| \nabla T^o \left(\vec{r} \right) \right| = s^o \left(\vec{r} \right). \tag{1}$$

In Equation (1), $T^o(\vec{r})$ is the TOF at position $\vec{r}$ with respect to the emitter location, and $s^o(\vec{r})$ is the slowness distribution and is the inverse of the SOS distribution. Our reconstruction model assumes straight acoustic rays propagating in 3D space.[35] Based on the straight-ray model, for a given emitter–transducer pair (q), the TOF, T_q^o, is calculated as an integral over the slowness distribution along a straight line:

$$\left[T^o \right]_q = \int s^o \left(\vec{r} \right) d\vec{r}. \tag{2}$$

For a discretized slowness object model of dimension, N, the mapping equation from object space to the data space is expressed as

$$\left[T^o \right]_q = \sum_{n=0}^{N-1} \left[s^o \right]_n l_{nq}, \tag{3}$$

where l_{nq} is the length segment of the linear ray for the qth emitter–transducer pair in the nth voxel. The relative TOF was calculated as the difference between the TOF for a homogeneous medium of slowness s^h and for the given slowness distribution. Mathematically,

$$\Delta T = T^h - T^o = L \left(s^h - s^o \right) = L \Delta s, \tag{4}$$

where T^h is the TOF vector for the homogeneous medium, and L is the system matrix with elements l_{nq}. An estimate of the relative slowness $(\Delta s \overset{def}{=} s^h - s^o)$ was reconstructed by solving the optimization problem,

Table 1. Optical and Acoustic Properties of the Optoacoustic/Ultrasonic Mouse Phantom.

Object	μ_a(760 nm) [cm^{-1}]	μ_a(1064 nm) [cm^{-1}]	c [mm/μs]
Target 1	2	1	1.42
Target 2	2	0	1.42
Phantom background	0	0	1.57
Acoustic coupling medium	0	0	1.50

$$\Delta\hat{s} = \min_{\Delta s \epsilon C} \left\| Ls - \Delta T \right\|^2 + 2\lambda TV(\Delta s), \tag{5}$$

where λ is the regularization parameter. Slowness was constrained to have values in a range defined based on the a priori knowledge of the object. We included the total variation (TV) regularization to accommodate severe incompleteness of the measured data and minimized our objective function using the monotone form of fast iterative shrinkage/threshold algorithm (FISTA). We followed the implementation of FISTA as described by Beck and Teboulle.[41]

Mouse

To demonstrate in vivo multiwavelength 3D-OAT, we imaged an Athymic Nude-Foxn1[nu] mouse (Harlan, Indianapolis, Indiana) that was 8 weeks old and weighed approximately 30 g. Animal handling, isoflurane anesthesia, and euthanasia were described in detail in our previous publications.[1,8] All the mouse-related procedures were in compliance with our Institutional Animal Care and Use Committee (IACUC) protocol. The mouse was sequentially scanned using 760 nm for imaging deoxygenated blood, 1064 nm for imaging oxygenated blood, and, finally, 532 nm for skin outline imaging. During the entire scanning procedure, the mouse remained in the same position inside the holder bracket. The laser fluence measured at the animal's skin was 0.4 mJ/(pulse·cm^2) for 760 nm, 0.8 mJ/(pulse·cm^2) for 1064 nm, and 0.5 mJ/(pulse·cm^2) for 532 nm.

Phantom

We prepared a dual-modality cylindrical gelatin phantom with dimensions similar to those of a mouse (∅25 mm) containing two 7 mm spherical polyvinyl chloride plastisol (PVCP) targets. Table 1 shows measured optical and acoustic properties of the phantom and the aqueous background. 3D-LUT scan of the phantom was followed by two optoacoustic scans at 760 nm and 1064 nm laser wavelengths using orthogonal (deep tissue) illumination mode.

Results

Performance of the LUT Unit

The primary novelty of our system is a 3D-LUT unit, which was designed for reconstruction of volumetric maps of SOS and spectral AA providing a new level of diagnostic information coregistered with optoacoustic data. In addition, the information contained in ultrasonic images can be employed in iterative algorithms of OAT to improve image fidelity. Laser ultrasound is generated through conversion of low-energy (about 100 μJ) 9 ns laser pulses into clean wideband acoustic pulses (Figure 7). The materials currently used in LOUIS-3DM for generation of laser ultrasound provide about 5 kPa of acoustic pressure per 1 mJ/cm^2 of incident 1064 nm laser radiation, as
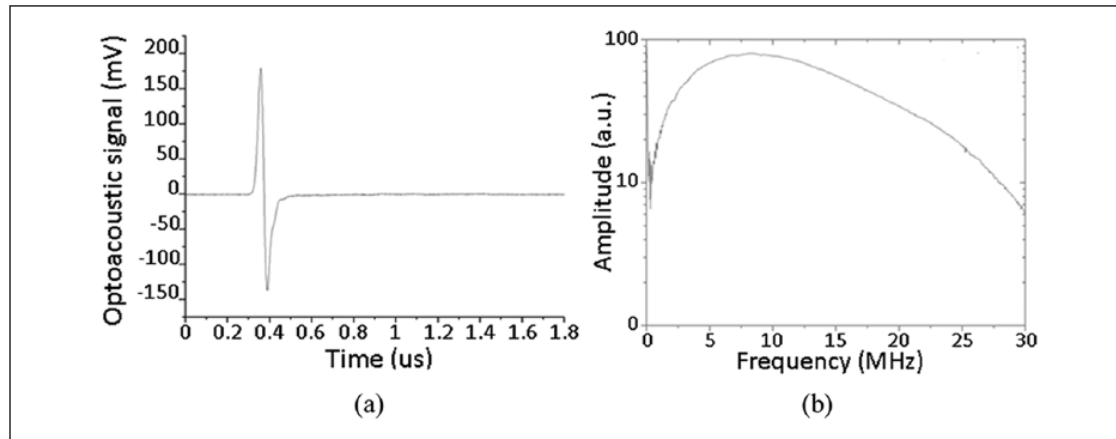
Figure 7. A pulse of laser ultrasound generated by the LUT prototype emitter (a) and its spectrum (b) showing central frequency at 8.5 MHz and 150% bandwidth. LUT = laser-induced ultrasound tomography.
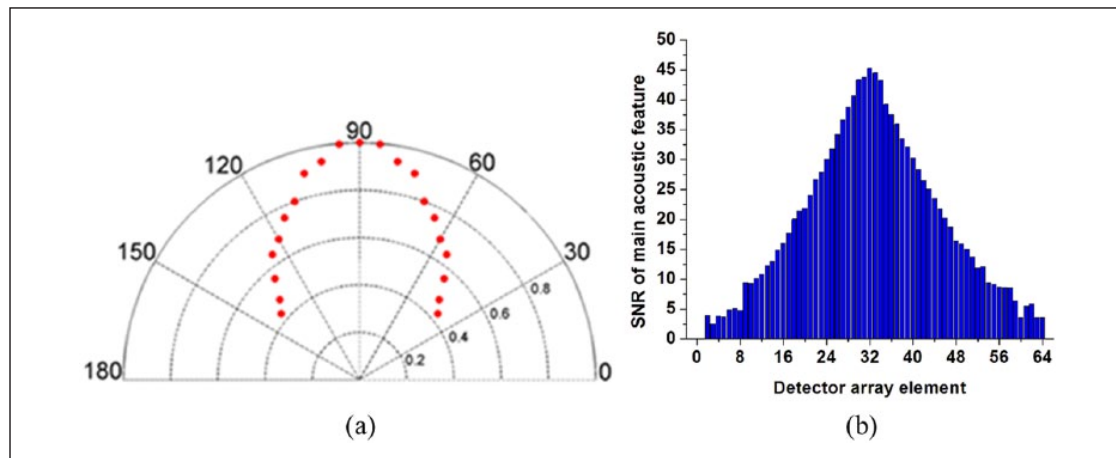

Figure 8. (a) Emission directivity of a single LU prototype. Graph made in the polar coordinate system shows the amplitude of the measured LU signal as a function of emission angle (deg). The data are normalized to the amplitude of the LU signal measured for normally emitted LU wave. (b) Variation of detected LU signal across the detector array. LUT unit provides a wavefront SNR of 5 or greater across the entire array. SNR = signal-to-noise ratios; LUT = laser-induced ultrasound tomography.

measured with our calibrated hydrophone. Pressure pulses have central frequency of 8.5 MHz and 150% bandwidth (Figure 7b).

We also characterized the directivity of the expanding acoustic waves generated by our LU sources. A true spherical wave would provide the best acoustic stimulus for our LUT system, as it would be detected uniformly along the entire array of receivers. Figure 8a shows directivity measured in the far field of the LU emitter, confirming that unattenuated laser ultrasound pulses (based on −6 dB level) are generated within the emission cone of 90°. To complete the analysis, emitter performance was evaluated within normal operating conditions of the LUT system. Signals were acquired for all detectors with the central emitter of the LU array being illuminated as a means of measuring the azimuthal spread of the acoustic field. The impulses were analyzed, and the signal-to-noise ratios (SNR) were tabulated for all channels. The data are plotted as the

bar graph shown in Figure 8b. These data show the LU emitter excites the detector array with acoustic signals that have SNR between 5 and 45, which is sufficient for reliable measurements of TOF.

We performed a numerical simulation of our experimental LUT setup and scanning procedure using a digital phantom with 3D SOS distribution replicating that of the phantom (see the section "Phantom"). Figure 9 shows the results of the simulation for the noiseless TOF data—left panel— and with additional Gaussian noise (Full width at half maximum, FWHM = 100 ns)—right panel. The images of the reconstructed meridional slice through the phantom (bottom panels in Figure 9) show that our LUT system should be able to provide high contrast accurate SOS images even under experimentally relevant noise levels. The reconstructed values of SOS were 1.430 ± 0.016 mm/μs (Average ± *SD*) and 1.519 ± 0.009 mm/μs for the spherical inclusions and the phantom matrix, respectively. The numbers were in close agreement with the original values of 1.42 and 1.52 mm/μs used in the simulations.

Multiwavelength 3D Optoacoustic Imaging

An example of in vivo multiwavelength 3D-OAT of a nude mouse (dorsal view) is shown in the Figure 10. The skin and superficial blood vessels were visualized using backward mode illumination with a 532 nm laser (Figure 10a). Deep tissue imaging using orthogonal illumination with an 800 nm wavelength, which is close to the isosbestic point of hemoglobin,[42] shows details of internal vascular network and blood-rich organs, like kidneys, spleen, and intestines (Figure 10b). Using 1064 nm laser with orthogonal illumination shifts the contrast of the visualized structures toward arterial circulation and tissues with high water content (Figure 10c). Using our combined imaging protocol (see the section "Optoacoustic Imaging Unit"), we created a volume showing the internal organs and circulatory system anatomically associated with the skin of the animal (Figure 10d). A video showing the rotating 3D-OAT image of the mouse could be found at https://youtu.be/BzonKQqOi14.

Coregistered 3D Optoacoustic and 3D Speed of Sound Imaging

We performed coregistered multiwavelength 3D-OAT and 3D-LUT imaging on a specially designed tissue mimicking phantom (see the section "Phantom"). Figure 11 shows a photograph of the cylindric gelatin phantom inside the mold during fabrication process (panel a) and opto- acoustic volumetric maps depicting spherical inclusions according to their optical absorption coefficients (panels b and c). The reconstructed laser-induced ultrasound image is depicted in Figure 11d, where the phantom outline and two inclusions are clearly delineated based on their SOS contrast. The reconstructed values of SOS were 1.538 ± 0.002 mm/μs (sphere 1), 1.546 ± 0.007 mm/μs (sphere 2), and 1.558 ± 0.018 mm/μs (phantom matrix). A video showing the rotat- ing 3D SOS image of the phantom could be found at https://youtu.be/_PtNTN6N_VY.

Discussion and Summary

In this work, we described the development of a 3D laser optoacoustic ultrasonic imaging system for preclinical research (LOUIS-3DM). A tank-based prototype of the system was tested in phan- tom studies to assess the quality of coregistered multiwavelength optoacoustic and SOS images. The obtained OAT and SOS images are fundamentally different from those previously demon- strated using different variants of a 2D-LUT slicer.[17,31,32] Jose et al. (2011) and Resink et al. (2011) were able to visualize 2.6 mm objects inside their agar phantoms, while Xia et al. (2013) were able to get outlines of an excised kidney of a mouse (~5 × 12 mm). However, despite reasonable in-slice
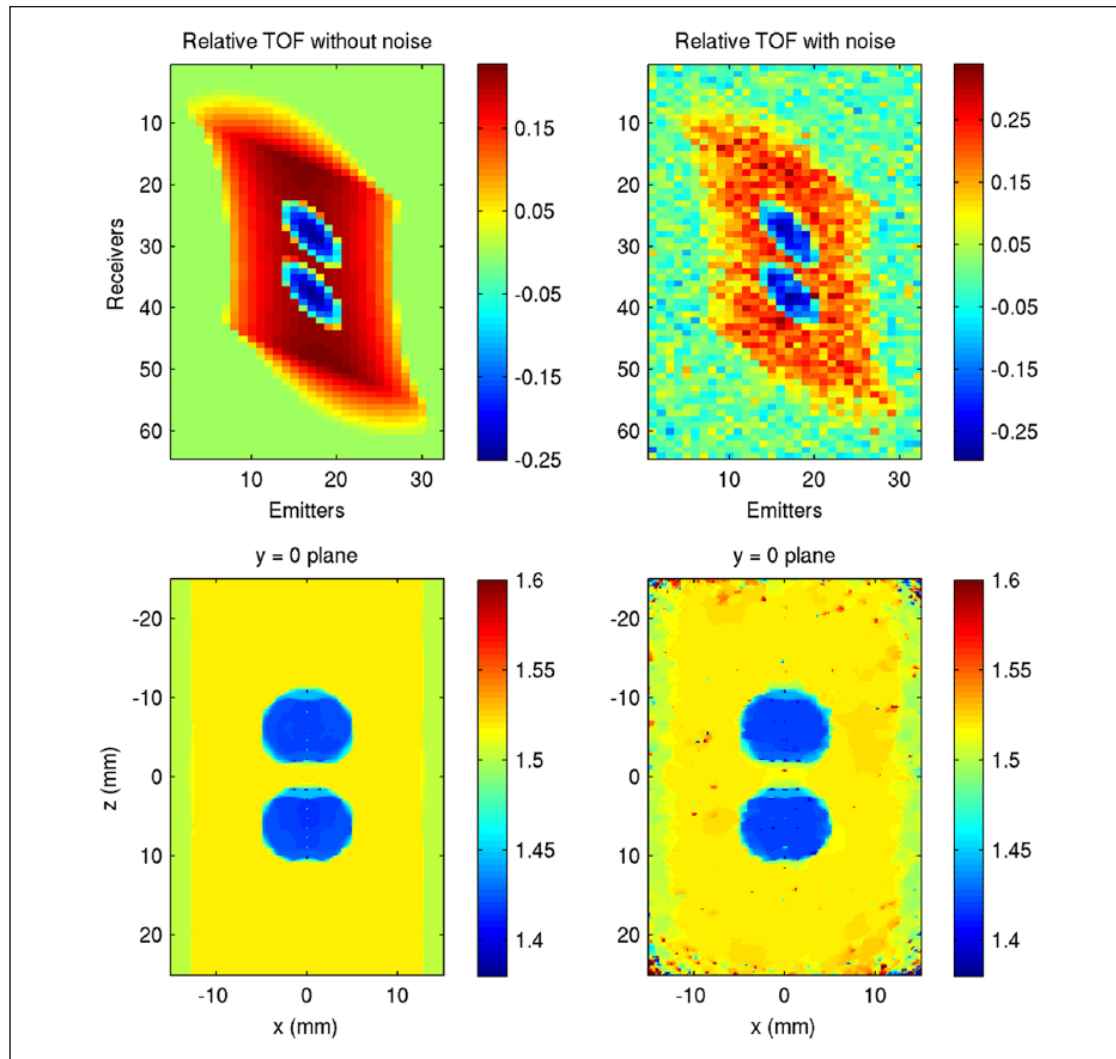
Figure 9. SOS reconstruction of a digital phantom that consists of a cylindric 24 mm in diameter body (SOS$_{body}$ = 1.52 mm/μs) with two spherical inclusions, 10 mm in diameter each (SOS$_{incl}$ = 1.42 mm/μs). Acoustically coupling medium has SOS$_{couple}$ = 1.50 mm/μs. Top panels show mapping of TOF measured at a particular rotational view for all emitter–receiver pairs. Due to the rotational symmetry of the phantom, the maps look identical for all the views. Colorbars, displayed on the right of each map indicate TOF deviation (μs) from the calibrated values (those measured for the same emitter–receiver pairs while LU propagated through background only). Bottom panels show the meridional slice through the phantom reconstructed via our tomographic algorithm (see the section "3D Speed of Sound Tomography"). The inclusions are clearly visible with high contrast on both the noiseless image (left panel) and on the image reconstructed from the data with additive 100 ns FWHM Gaussian noise (right panel). A total of 72 views were simulated. Colorbars, displayed on the right of each reconstructed image indicate SOS (mm/μs). SOS = speed of sound; TOF = time of flight.

resolution of the SOS images, all the implementations did not claim any practical capability in stacking parallel slices of SOS and AA into a continuous volume, suffering from difficulties of in-slice focusing and interslice registration. Therefore, in these studies, we proceeded with the fully 3D-LUT approach, which finally provided high-quality reconstruction of continuous 3D volumes of SOS fully coregistered with the already established 3D-OAT imager, as it could be seen in Figure S2 (Supplementary Materials) and Figure 11.
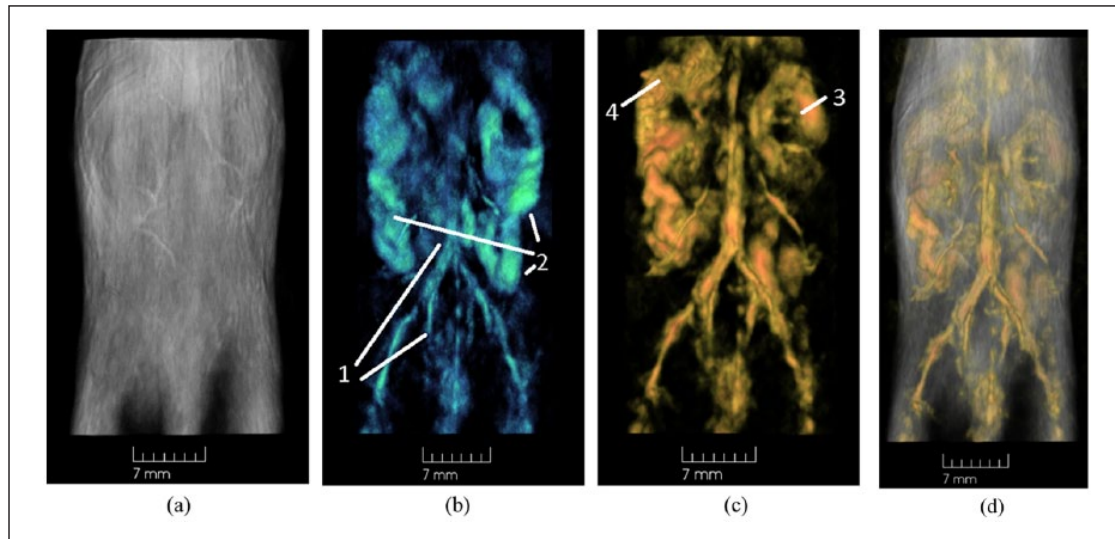
Figure 10. In vivo 3D optoacoustic image of a nude mouse (dorsal view). (a) Image acquired in the backward mode with 532 nm laser illumination showing skin and superficial blood vessels. (b) and (c) Deep tissue images acquired in the orthogonal illumination mode with an 800 and 1064 nm wavelengths. Deep tissue OAT images uncover fine spatial details of central and peripheral circulatory system (1), intestine (2), right kidney (3), and spleen (4). (d) A composite OAT image showing spatial details of the internal organs and circulatory system referenced to the skin of the animal. OAT = optoacoustic tomography.
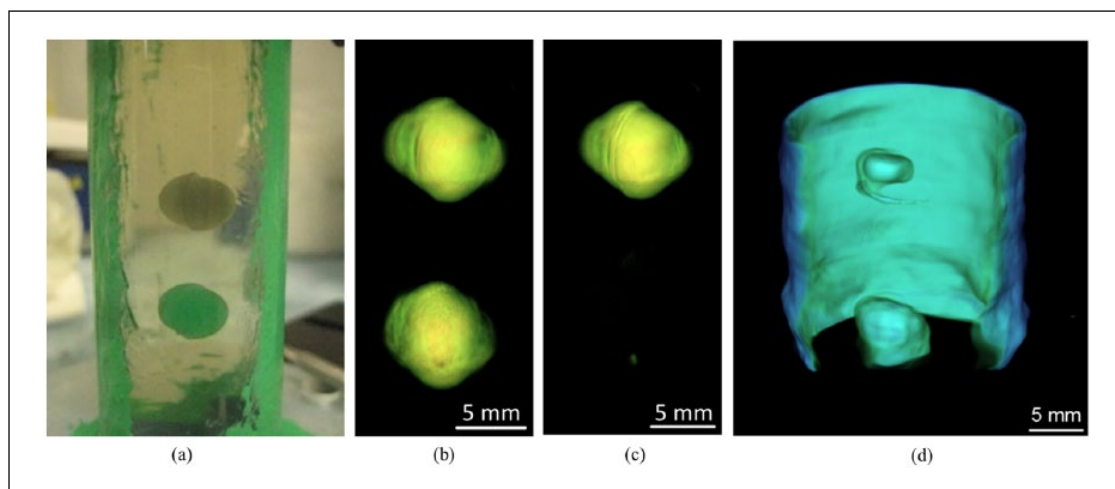

Figure 11. (a) Mouse phantom in the mold with Target 1 at the top and Target 2 below. (b) Optoacoustic image acquired at 760 nm showing both targets. (c) Optoacoustic image acquired at 1064 nm showing only the top target (Target 1). (d) Reconstructed speed of sound volume showing the phantom's exterior boundary and both targets.

One obvious disadvantage of our 3D-LUT technique as compared to the published 2D implementations is the speed of data acquisition. Jose et al. (2011) employed a single passive LU element, 45 views per scan, and 100 averages per view, which totaled to about 8 min.[31] LU scans by Resink et al. (2011) were done using multielement implementation of LU emitters (9 emitters)

with otherwise identical setup, which allowed them to reduce time of the scans from 13.3 min (80 views) down to 1.5 min (9 views), although with some degradation of the image quality.[32] Our LUT scans took 1.5 hr (72 views, 33 emitters, 64 averages) followed by about 15 min per each additional OAT scan (1500 views, no averages). One obvious way to accelerate our LUT scans is to reduce number of averaging required for an acceptable SNR. To do this, a larger laser energy could be delivered through the fiber-optics. Currently, to prevent crosstalk between adjacent LU emitters, we coupled well the output of the laser fiber into an input of the LU emitter fiber using a ball-lens system (Figure 4b and 4c). However, the input of the 600 μm laser fiber is passively inserted into a 6 mm output laser beam, which results in a significant loss of the coupled laser energy (at least 100 times) producing an output spot of just 100 μJ. Therefore, increasing the energy of individual LU sources by at least 10 times is not a significant problem and would require an additional beam coupling optical system at the input of the laser fiber. Stronger emission of LU sources will also relax the requirements of the amplification, therefore reducing the random noise.

Two-dimensional LUT prototypes were also designed to simultaneously acquire LUT and OAT data by temporally separating OA signals generated inside the interrogated object from the artificial LU signals, which arrive later.[30-32] In these studies, we did not implement OAT and LUT scans to be run simultaneously. The reason was to first demonstrate in a clear experiment (sequential LUT and OAT scans) capabilities and advantages of the fully 3D-LUT. In a 3D-OAT geometry, useful signals come from the interrogated object during the time interval, which may significantly exceed the time interval for useful OAT signals in 2D slicer. Therefore, the LU emitters must be separated from the array of receivers by a longer distance to not interfere with the OA signals. Longer separation between the array of emitters and receivers increases the requirements for the laser pulse energy to maintain the same SNR. It also reduces the size of interrogated volume unless the array of emitters is proportionally extended. We still believe that possibility of simultaneous OAT and LUT scanning, originally proposed by Manohar et al. (2007) for 2D geometry,[30] is a useful approach to accelerate and simplify data acquisition, and we will investigate its applicability to a fully 3D-LUT in our future studies.

Resolution of the reconstructed LUT images increases with higher density of the laser ultrasound emitters/receivers.[30,31,43] In 2D geometries, LUT prototypes benefit from the established industrial standards for high-quality ultrasound arrays (receivers) with a small inter element pitch. In case of 3D-LUT, both emitters and receivers must be tightly arranged. In these studies, our array of emitters had 33 LU sources separated by 3.4 mm from each other. The emitter-forming optical fibers were individually embedded into acrylic matrix. To increase emitters' density in the future prototypes, individual fiber slots could be abandoned and instead all the fibers densely packed within a single diagonal groove. Minimum LU emitter pitch for the same type of fibers arranged in a linear pattern could be in this case reduced to 1.1 mm, allowing three times the number of emitters over the same aperture of the array. Alternatively, more complex 2D patterns of the LU emitters may be considered.

Poor directivity of emitter–receiver pairs reduces SNR and widens the measured LU pulse.[27] It eventually leads to the loss of fidelity in evaluated TOF. The directivity of our LUT unit (Figure 8) was sufficient to provide 90° −6dB emission cone and SNR of 5-45 for the central emitter and the entire array of receivers. For the best directivity performance, each emitter should be aimed toward the bisector with respect to the outermost receivers. However, such an implementation is technologically challenging and was not attempted during our prototyping. Improved directivity performance could be also achieved by increasing LU source power toward the outside of the emitters' array by using, for example, thinner optical fibers (200 μm) in the middle and thicker (600 μm) at the ends of the array. Even wider directivity of individual emitters could be provided by spherical LU sources. Conjusteau et al. (2013) used spherical LU emitters made out of ball

lenses and demonstrated significantly wider emission directivity than that of the 600 μm planar source.[44] However, spherical emitters have large cross-section and, therefore, impose additional limitations on the emitter pitch.

In this work, we used 3D-LUT to visualize phantom inclusions with SOS 10% smaller than in the phantom matrix. Our simulations (Figure 9) showed that experimentally relevant 100 ns random TOF noise does not present a problem for the quality of reconstruction. In this case, both forward model of ultrasound wave propagation and the inverse model utilized in the reconstruction algorithm assumed straight acoustic rays. The estimates of SOS (for targets and phantom matrix) agreed well with the set values with only a slightly higher number (by 0.7%) obtained for the SOS of the targets. However, when the experimental data were analyzed, the reconstructed values for the SOS in spherical targets exceeded the measured SOS values by more than 8%, while the SOS estimates remained quite accurate for the phantom's matrix (lower by just 0.8%). Both targets were still reconstructed in a correct negative SOS contrast with respect to the phantom's matrix and allowed clear delineation along their boundaries (see Figure 11). The discrepancy in the reconstructed SOS could originate from the following two sources. First, the utilized straight-ray model is a rough approximation, which works well only in situations where SOS deviations are very small. When this assumption is violated, the acoustic rays are getting refracted on heterogeneous interfaces and produce systematic error in estimated SOS. From this point of view, the SOS of targets (1.42 mm/μs) likely differed enough from the SOS of phantom's matrix (1.57 mm/μs) to violate this approximation. Second, the size of targets was quite small, and our setup could only provide very sparse sampling of the TOF measurements through the spherical targets with few receiver–source pairs providing TOF from the rays passing through the targets. In this scenario, the system matrix becomes underdetermined, which we tried to partially compensate by including a TV regularization. The penalty term can also contribute to the observed deviations of SOS from the expected values.

The fundamental limitations of TOF sensitivity are defined by the sampling rate of the DAQ system. We used the 40 MHz sampling rate as Xia et al. (2013),[17] which is translated into a maximum TOF resolution of 25 ns, while Jose et al. (2011)[31] sampled the signals twice faster. In reality, these numbers are generally superseded by the accuracy of the method used for TOF detection (see Section S2 in the Supplementary Materials for more details on accuracy and sensitivity of the TOF measurements). In these studies, we used a simple method based on the detection of the pulse's onset as soon as it exceeds the threshold, which was established from the channel's RMS noise. Xia et al. (2013) used cross-correlation technique[17] and Jose et al. (2011) had it refined with maximum likelihood (ML) estimator.[31] However, both techniques are still not ideal in case of dispersive behavior of the acoustic waves. Other, more complex, TOF pickers were also developed.[45] The next step to improve accuracy of the reconstructed 3D SOS images would be to apply more sophisticated reconstruction algorithms. For example, a bent-ray model approach was implemented in 2D SOS tomography[23] and could be potentially adapted for 3D problems.

Currently, only 3D SOS tomography was developed in details and successfully tested in phantoms. Improved quality of generated LU pulses should allow us in the future to make a next step toward reconstruction of spectral ultrasound attenuation maps. The ultimate goal would be in vivo coregistered multiwavelength optoacoustic and laser-induced ultrasound imaging in a mouse and modification of the system for clinical 3D-OAT and UCT applications, like diagnostics of breast cancer.

Declaration of Conflicting Interests

Funding

Supplementary Material

Supplementary materials are available on the Ultrasonic Imaging website at http://uix.sagepub.com/supplemental.

References

1. Brecht HP, Su R, Fronheiser M, Ermilov SA, Conjusteau A, Oraevsky AA. Whole-body three-dimensional optoacoustic tomography system for small animals. J Biomed Opt. 2009;14(6):064007.
2. Xia J, Chen W, Maslov K, Anastasio MA, Wang LV. Retrospective respiration-gated whole-body photoacoustic computed tomography of mice. J Biomed Opt. 2014;19(1):16003.
3. Gateau J, Caballero MA, Dima A, Ntziachristos V. Three-dimensional optoacoustic tomography using a conventional ultrasound linear detector array: whole-body tomographic system for small animals. Med Phys. 2013;40(1):013302.
4. Oraevsky AA. Optoacoustic tomography: from fundamentals to diagnostic imaging of breast cancer. In: Vo-Dinh T, ed. Biomedical Photonics Handbook. 2nd ed. Boca Raton, FL: CRC Press; 2014. pp. 715-57.
5. Wang LV, Hu S. Photoacoustic tomography: in vivo imaging from organelles to organs. Science. 2012;335(6075):1458-62.
6. Chitnis PV, Brecht HP, Su R, Oraevsky AA. Feasibility of optoacoustic visualization of high-intensity focused ultrasound-induced thermal lesions in live tissue. J Biomed Opt. 2010;15(2):021313.
7. Su R, Ermilov S, Liopo A, Oraevsky AA. Optoacoustic 3D visualization of changes in physiological properties of mouse tissues from live to postmortem. Proc SPIE. 2012;8223:82230K.
8. Su R, Ermilov SA, Liopo AV, Oraevsky AA. Three-dimensional optoacoustic imaging as a new noninvasive technique to study long-term biodistribution of optical contrast agents in small animal models. J Biomed Opt. 2012;17(10):101506.
9. Tsyboulski DA, Liopo AV, Su R, Ermilov SA, Bachilo SM, Weisman RB, et al. Enabling in vivo measurements of nanoparticle concentrations with three-dimensional optoacoustic tomography. J Biophotonics. 2014;7(8):581-8.
10. Stiel AC, Dean-Ben XL, Jiang Y, Ntziachristos V, Razansky D, Westmeyer GG. High-contrast imaging of reversibly switchable fluorescent proteins via temporally unmixed multispectral optoacoustic tomography. Opt Lett. 2015;40(3):367-70.
11. Beziere N, Lozano N, Nunes A, Salichs J, Queiros D, Kostarelos K, et al. Dynamic imaging of PEGylated indocyanine green (ICG) liposomes within the tumor microenvironment using multi-spectral optoacoustic tomography (MSOT). Biomaterials. 2015;37:415-24.
12. Bao C, Beziere N, del Pino P, Pelaz B, Estrada G, Tian F, et al. Gold nanoprisms as optoacoustic signal nanoamplifiers for in vivo bioimaging of gastrointestinal cancers. Small (Weinheim an der Bergstrasse, Germany). 2013;9(1):68-74.
13. Krumholz A, Shcherbakova DM, Xia J, Wang LV, Verkhusha VV. Multicontrast photoacoustic in vivo imaging using near-infrared fluorescent proteins. Sci Rep. 2014;4:3939.
14. Ermilov S, Su R, Liopo A, Oraevsky AA. Optoacoustic angiography of peripheral vasculature. Proc SPIE. 2012;8223:82230D.
15. Kruger RA, Kuzmiak CM, Lam RB, Reinecke DR, Del Rio SP, Steed D. Dedicated 3D photoacoustic breast imaging. Med Phys. 2013;40(11):113301.

16. Dean-Ben XL, Ntziachristos V, Razansky D. Effects of small variations of speed of sound in opto-acoustic tomographic imaging. Med Phys. 2014;41(7):073301.

17. Xia J, Huang C, Maslov K, Anastasio MA, Wang LV. Enhancement of photoacoustic tomography by ultrasonic computed tomography based on optical excitation of elements of a full-ring transducer array. Opt Lett. 2013;38(16):3140-3.

18. Carson PL, Meyer CR, Scherzinger AL, Oughton TV. Breast imaging in coronal planes with simultaneous pulse echo and transmission ultrasound. Science. 1981;214(4525):1141-3.

19. Schreiman JS, Gisvold JJ, Greenleaf JF, Bahn RC. Ultrasound transmission computed tomography of the breast. Radiology. 1984;150(2):523-30.

20. Greenleaf JF, Bahn RC. Clinical imaging with transmissive ultrasonic computerized tomography. IEEE Trans Biomed Eng. 1981;28(2):177-85.

21. Duric N, Littrup P, Babkin A, Chambers D, Azevedo S, Pevzner R, et al. Development of ultrasound tomography for breast imaging: technical assessment. Med Phys. 2005;32(5):1375-86.

22. Chang CH, Huang SW, Yang HC, Chou YH, Li PC. Reconstruction of ultrasonic sound velocity and attenuation coefficient using linear arrays: clinical assessment. Ultrasound Med Biol. 2007;33(11):1681-7.

23. Li C, Duric N, Littrup P, Huang L. In vivo breast sound-speed imaging with ultrasound tomography. Ultrasound Med Biol. 2009;35(10):1615-28.

24. Nebeker J, Nelson TR. Imaging of sound speed using reflection ultrasound tomography. J Ultrasound Med. 2012;31(9):1389-404.

25. Diebold GJ, Sun T, Khan MI. Photoacoustic monopole radiation in one, two, and three dimensions. Phys Rev Lett. 1991;67(24):3384-7.

26. Yang H, Kim JS, Ashkenazi S, O'Donnell M, Guo LJ. Optical generation of high frequency ultrasound using two-dimensional gold nanostructure. Appl Phys Lett. 2006;89(9):093901.

27. Conjusteau A, Ermilov SA, Su R, Brecht HP, Fronheiser MP, Oraevsky AA. Measurement of the spectral directivity of optoacoustic and ultrasonic transducers with a laser ultrasonic source. Rev Sci Instrum. 2009;80(9):093708.

28. Maslov K, Zhang HF, Wang LV. Photoacoustic generation of focused quasi-unipolar pressure pulses. J Innov Opt Health Sci. 2010;3(4):247-53.

29. Hou Y, Ashkenazi S, Huang SW, O'Donnell M. Improvements in optical generation of high-frequency ultrasound. IEEE Trans Ultrason Ferroelectr Freq Control. 2007;54(3):682-6.

30. Manohar S, Willemink RG, van der Heijden F, Slump CH, van Leeuwen TG. Concomitant speed-of-sound tomography in photoacoustic imaging. Appl Phys Lett. 2007;91:131911.

31. Jose J, Willemink RG, Resink S, Piras D, van Hespen JC, Slump CH, et al. Passive element enriched photoacoustic computed tomography (PER PACT) for simultaneous imaging of acoustic propagation properties and light absorption. Opt Express. 2011;19(3):2093-104.

32. Resink S, Jose J, Willemink RG, Slump CH, Steenbergen W, van Leeuwen TG, et al. Multiple passive element enriched photoacoustic computed tomography. Opt Lett. 2011;36(15):2809-11.

33. Roitner H, Bauer-Marschallinger J, Berer T, Burgholzer P. Experimental evaluation of time domain models for ultrasound attenuation losses in photoacoustic imaging. J Acoust Soc Am. 2012;131(5):3763-74.

34. Huang C, Nie L, Schoonover RW, Wang LV, Anastasio MA. Photoacoustic computed tomography correcting for heterogeneity and attenuation. J Biomed Opt. 2012;17(6):061211.

35. Jose J, Willemink RG, Steenbergen W, Slump CH, van Leeuwen TG, Manohar S. Speed-of-sound compensated photoacoustic tomography for accurate imaging. Med Phys. 2012;39(12):7262-71.

36. Luke GP, Emelianov SY. Optimization of in vivo spectroscopic photoacoustic imaging by smart optical wavelength selection. Opt Lett. 2014;39(7):2214-7.

37. Cox B, Laufer JG, Arridge SR, Beard PC. Quantitative spectroscopic photoacoustic imaging: a review. J Biomed Opt. 2012;17(6):061202.

38. Kruger RA, Liu P, Fang YR, Appledorn CR. Photoacoustic ultrasound (PAUS)—reconstruction tomography. Med Phys. 1995;22(10):1605-9.

39. Wang K, Huang C, Kao YJ, Chou CY, Oraevsky AA, Anastasio MA. Accelerating image reconstruction in three-dimensional optoacoustic tomography on graphics processing units. Med Phys. 2013;40(2):023301.

40. Anis F, Su R, Nadvoretsky VV, Conjusteau A, Ermilov SA, Oraevsky AA, et al. Image reconstruction and system optimization for three-dimensional speed of sound tomography using laser-induced ultrasound. Proc SPIE. 2013;8581:85814T.

41. Beck A, Teboulle M. A fast iterative shrinkage-thresholding algorithm for linear inverse problems. SIAM J Img Sci. 2009;2:183-202.

42. Roggan A, Friebel M, Doerschel K, Hahn A, Mueller G. Optical properties of circulating human blood in the wavelength range 400-2500. J Biomed Opt. 1999;4(1):36-46.

43. Suetens P. Fundamentals of Medical Imaging. 2nd ed. Cambridge: Cambridge University Press; 2009.

44. Conjusteau A, Nadvoretskiy VV, Ermilov SA, Oraevsky AA. Generation of wide-directivity broadband ultrasound by short laser pulses. Proc SPIE. 2013;8581:85814U.

45. Li C, Huang L, Duric N, Zhang H, Rowe C. An improved automatic time-of-flight picker for medical ultrasound tomography. Ultrasonics. 2009;49(1):61-72.